Dissertation

submitted to the

Combined Faculty of Natural Sciences and Mathematics

of the Ruperto Carola University Heidelberg, Germany

for the degree of

Doctor of Natural Sciences

Presented by

Kulikov Ivan

born in: Maloyaroslavets, Russia

Oral examination: 05-07-2021

Study of the A=100 deformation region through high precision mass measurements of the neutron rich krypton isotopes

Referees: Dr. Apl. Prof. Yuri Litvinov

Dr. Priv.-Doz. Wolfgang Quint

Abstract

Nuclear structure effects such as shape-transition are observed as sudden changes in the mean-square charge radii, low-lying excitation energies and the binding energies evolution. The latter is executable by the direct mass measurements. The deformation in the krypton isotopic chain has been an open question for decades and this work presents the direct mass measurement of $^{96-98}$Kr isotopes. The isotopes of interest have been produced at the ISOLDE facility at CERN. The mass measurements were performed by use of the versatile ISOLTRAP mass spectrometer. The multi-reflection time of flight and the time of flight ion cyclotron resonance techniques were applied for the mass determination. The mass of ^{98}Kr isotope was determined for the first time. Results from the state of the art mean-field and beyond mean-field approaches are compared to the experimental binding energy trends.

Kernstruktureffekte wie der Formübergang können anhand von plötzlichen Änderungen des mittleren quadratischen Ladungsradius, von niedrig liegenden Anregungsenergien und von der Entwicklung der Bindungsenergien veranschaulicht werden. Mit Hilfe von hoch-präzisen Massenmessungen kann man Letzere messen. Kernstrukturelle Verformungen in der Isotopenkette von Krypton sind seit Jahrzehnten eine offen Frage, welche mit der in dieser Arbeit präsentierten Präzisionsmassenmessung der Krypotonisotope $^{96-98}$Kr ausführlich behandelt wird. Genannte Isotope wurden an ISOLDE/CERN produziert und mit Hilfe des Massenspektrometers ISOLTRAP gemessen, wobei die Mass von ^{98}Kr zum ersten Mal direkt bestimmt werden konnte. Für die Massenbestimmung wurden die Multi-reflection Time of Flight und die Time of Flight Ion Cyclotron Resonance techniken angewendet. Die Ergebnisse der Messungen werden mit modernen Methoden der Molekularfeldtheorie verglichen.

Contents

List of Figures

List of Tables

Acknowledgements

I want to thank my primary supervisor Dr. Apl. Prof. Yuri Litvinov for all the help and support he provided me during these four years. His knowledge about the physics of trapped and stored ions and the positive attitude helped me evaluate the work. Yuri Litvinov was always available for any help from physics until general management/administrative advising. He gave me the best condition to study I have ever had in my life in terms of physics discussions and funding. I could always rely on him. During the project, I knew if I make some mistakes Yuri will watch my back. So it was all safe to do the research. I could always come to Yuri, dream about the future and often unrealistic future :) and he would just smile or makes sarcastic jokes which seems only Russians can understand. So thank you very much Yuri, it was joyful to work with you during these years.

Second, I would like to thank my second supervisor Prof. Dr. Klaus Blaum. The person who knows everything about traps and associated physics. His advices were always clear. During the discussions, Klaus starts with simple ideas which are very easy to understand and follow. He is always available for help, always smiling and at the same time serious researcher with very deep knowledge in physics. He also provided me with the best conditions to work and flourish. His funding sources seem to be infinite and I could always rely on it if I needed to buy some materials for the lab. Thank you very much Klaus.

Third, I would like to thank my local teammates. With these guys, we went together through all the stages, through thick and thin of the negotiations. I would like to thank Dr. Maxime Mougeot for his advising as a local supervisor. Also, I would like to thank Lukas Nies, our newest PhD student. I believe he will do a great job at ISOLTRAP. He already does. Last but not least, I would like to thank Dr. Jonas Karthein. The person who was acting as a buddy from the beginning of my project. It was very nice and easy to communicate with him and it was always joyful to work together in the lab.

Fours, I would like to thank ex-ISOLTRAPers. I would like to thank Dr. Frank Wienholtz for his advicing on the equipment and how to choose a proper tool. I personally can build a setup from wood and dirt; therefore, his help was essential for me. I would like to thank Dr. Vladimir Manea. Although he has been far away, I could always send him a mail and receive a manual/instruction answering all my questions and even more. A special thank goes

to Dr. Dinko Atanasov. This person was helping me at all stages of my project, especially with socialization and understanding all the other colleagues. If I write about socialization, I also must mention Dr. Dave Lunney. He was always making fun of all these ”Sheldons” around and also surprisingly knows a lot about PhD culture. Thanks, thanks, thanks.

And fifth, I would like to thank all members of my big family. Brothers and sisters, mother and father, grands, aunts and uncles. All your letters and postcards I reread in the darkest times of my life. Nothing makes me warmer than this. Although there is a very big distance between us, I feel your love and I will make it through my entire life. My wife Masha, these years have been a real test for us. And I am very happy to see that together we did a really great job. Keep it up.

I

Chapter 1

Introduction

1.1 Why do we measure the mass of the nucleus?

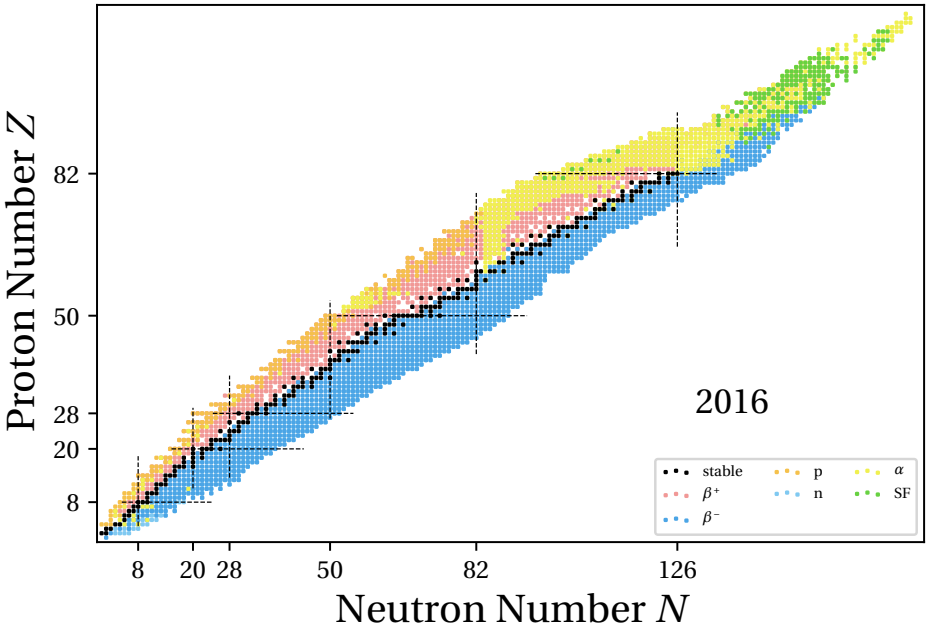

Figure 1.1. The nuclear chart presenting all experimentally known isotopes. Each square represents a nuclide and the colors represents main decay modes.

One of the fundamental properties of a nucleus is its mass, which reflects nuclear structure through the binding energy [G+13a], answering questions about the element's origin [Gor01] and even testing the standard model [H+09]. There is an enormous amount of data collected over more than a hundred years of experimental investigations, which can be summarized in figure 1.1. This figure is the visual representation, details of the nuclear masses measured by different methods have been collected in the Atomic Mass Evaluation [M+21]. The analysis of the available data supports the modern understanding of the evolution of the mass surface by ap-

plying various mass filters along isotopic, isotonic or isobaric chains. Nuclear-structure effects such as shell closures [W$^+$13a] or onsets of deformation [M$^+$13a] are revealed as irregularities on the smooth mass surface. Therefore, new precision mass measurements are indispensable for investigations of such effects. Furthermore, the mass values are an essential input for modeling the astrophysical processes [M$^+$06]. For instance, explosive nucleosynthesis processes involve exotic nuclides with presently unknown masses [Gor01]. The description thus relies upon predictions by nuclear-mass models [C$^+$21], which in turn have to be constrained through accurately measured masses [A$^+$15]. Even in the investigations of the weak interaction, the mass measurements may play a significant role. The Q-value of the neutrinoless double-beta decay can answer the questions about fundamental properties of the neutrino particle [F$^+$12]. Moreover, mass spectrometry contributes to tests of the unitary of the Cabibbo-Kobayashi-Maskawa quark-mixing matrix through constraining the $|V_{ud}|$ element [H$^+$15].

Such diverse research directions require unique tools. J.J. Thomson and his student F.W. Aston were the first to build mass spectrometers at the beginning of the last century [M$^+$10]. Since then technologies related to mass spectrometry are under constant upgrade in terms of the precision, focusing and effective manipulations of the ion motions using the electromagnetic fields. For example, the first device had 10^{-3} level of relative precision and nowadays the relative precision of mass spectrometers can reach 10^{-12}. Such remarkable improvement in the field of mass spectrometry was achieved by introducing the Radio Frequency Quadrupole(RFQ) spectrometers [PS53], Time of Flight systems [WP90], Penning traps [GK78] and Storage rings [L$^+$20b]. Moreover, not only the systems but the different mass measurement techniques are under constant upgrade to reach a better resolving power and precision. A recent and one of the most promising techniques is the phase-imaging ion cyclotron resonance technique [E$^+$14] applied in Penning traps. The central device of this work is the ISOLTRAP mass spectrometer. It combines different devices and techniques the details of which are discussed in Section 2.2-2.5.

In the early years of mass spectrometry field researchers were studying stable species available in nature. The discovery of radioactivity led to the development of the field such that today 3437 masses of different nuclides are known [M$^+$21]. The progress on the production and separation methods of radioactive nuclei made it possible. Among the laboratories in the world, the first five places in the number of discovered isotopes are occupied by the Lawrence Berkeley National Laboratory (638) [S$^+$09c], GSI Helmholtz Centre for Heavy Ion Research (438) [H$^+$12], the Joint Institute for Nuclear Research (221) [Oga10], the Cavendish Laboratory (218) [Lon16] and CERN (115) [BB18]. These laboratories differ by the production and separation methods of radioactive isotopes. The ISOLTRAP mass spectrometer was installed at ISOLDE/CERN facility in yearly 1980s to measure masses of radioactive isotopes and since then addressed more than 600 short-lived nuclides [Kow10]. The production and separation

methods of the ISOLDE facility are discussed in Section 2.1.

1.1.1 The motivation for astrophysics

The cosmos is the unique and free laboratory existing in nature. All objects in the universe such as galaxies, stars, interstellar environment, planets, meteorites have been sources of information about the world we live in [WLM05]. Today researchers are particularly interested in how and where the elements are produced [Z$^+$16].

At first, the production of elements was carefully studied in the Sun. Through the ppI thermonuclear cycle [SC05], four protons create a He nucleus with the release of a tremendous amount of energy, electron neutrinos, photons, and positrons. The ppII and ppIII cycles are responsible for producing the elements until boron, which can be achieved in Sun-like stars. However, there are other stars of mass much more than the Sun, and through the CNO cycle [S$^+$09b], triple α-process [Sal52] and nuclear fusion reactions elements can be created until the iron nucleus.

The significant invention was the proposed slow and rapid neutron capture processes [B$^+$57, A$^+$07]. The slow neutron capture is the process that starts from stable iron and continues until lead/bismuth. It creates mostly stable elements of the nuclear chart followed by a β^- decay transforming the neutron into a proton. The most likely place to observe such a process is the Asymptotic Giant Branch (AGB) stars [Sie06]. The rapid neutron capture is the process when the elements heavier than iron are produced through consequent (n, γ) reactions. The neutron-rich elements of the nuclear chart are produced through this process. The most probable place where such extreme conditions can be achieved is the core-collapsing supernovae or neutron-star mergers environments [L$^+$98]. ISOLTRAP mass spectrometer put many efforts to study r-process by performing precision mass measurements, as an example $^{129-131}$Cd isotopes [A$^+$15]. For the rapid neutron capture process the equilibrium between (n, γ) and (γ, n) reactions has to be reached. The general and first approximation for the statistical balance can be expressed as:

$$log(\frac{n(N+1,Z)}{n(N,Z)}) = log(n_n) - 34.07 - \frac{3}{2}log(T_9) + \frac{5.04}{T_9}S_n \tag{1.1}$$

$n(N,Z)$: the number density of a nucleus with N,Z number of neutrons and protons
n_n : the number density of free neutrons
T_9 : the temperature T/$10^9 K$
S_n : one neutron separation energy

By precisely measuring the mass of the nucleus researcher can obtain the one neutron separation energy (see the nuclear binding energy subsection 1.2) which is the contribution of the

mass measurements in the nucleosynthesis calculations. The mass of $^{129-131}$Cd isotopes were used for the simulation of ν-driven wind model of the core-collapse supernovae [W$^+$11a] and the decompression of the neutron star merger model [G$^+$13b]. For the detailed description of the reaction network calculations reader is refereed to [Lan99].

The rapid proton capture process also exists in nature [A$^+$03], but protons have to overcome the Coulomb barrier. In the rp-process, protons are captured via a sequence of (p, γ) reactions and β^+ decays [G$^+$19]. The process runs on the neutron-deficient part of the nuclear chart. A new element will be produced if the capture reaction is faster than the decay of the parent nucleus or until the proton drip line has been reached. According to the current computer simulations, this process can not produce all neutron-deficient nuclei. Therefore, scientists are looking for other processes to explain the abundances, for example, νp process [S$^+$09a]. The ISOLTRAP mass spectrometer contributes and regularly proposes to measure masses of nuclei for these processes, as an example [H$^+$11]. These nuclei are of the high demand for the theoretical models of type I x-ray burst and collapse scenario of supernova where these processes most probably take place [P$^+$13, SR06].

This is just a tiny overview aiming to show that mass measurements play a crucial role in understanding how the elements are produced. Most of the isotopes are created in very extreme environments, and a limited number of them can be reached at nuclear facilities because of their short half-lives and production yields. Therefore, the theoretical models try to describe the production mechanisms, and precise mass measurements [N$^+$20, A$^+$16] are needed to constrain the theoretical calculations.

1.1.2 The motivation for fundamental interactions physics

The electron is the first elementary particle, which was discovered in 1892 [Tho97]. In 1964 Murray Gell-Mann and George Zweig assumed the composite nature of the proton and the neutron [GM64]. Now it is a scientific fact that they consist of u and d quarks. Attempts to describe the observed phenomena led to the development of the standard model [Hig64]. The standard model describes three of four fundamental interactions: weak, strong and electromagnetic.

One of the interactions which can be studied through precision mass measurements is weak interaction. The interaction is accessible through β-decays of nuclei. This decay is nothing else but the flavor change of quarks. The flavor change of quarks is taken into account in the Cabibbo–Kobayashi–Maskawa(CKM) matrix [Cab63]. The mass spectrometrists contribute to testing the unitary of this matrix through calculations of $|V_{ud}|$ element. Equation 1.2 links the mass measurement contribution in the calculation of the Ft value of a β-transition:

$$Ft = ft(1 + \delta_R^{'})(1 + \delta_{NS} - \delta_C) = \frac{K}{2G_V^2(1 + \Delta_R^V)} \tag{1.2}$$

ft : the strength of the transition
δ_C : the isospin symmetry-breaking correction
$\delta_R^{'}, \delta_{NS}$: transition-dependent part of the radiative correction
K : constant
G_V : the vector-coupling constant
Δ_R^V : transition-independent part of the radiative correction

To obtain the G_v constant, superallowed Fermi decays are typically considered. The experimental ft value is related to the vector-coupling constant G_V [H$^+$15]. After obtaining the vector-coupling constant G_V one can calculate $|V_{ud}| = \frac{G_V}{G_F}$, where G_F is a weak-interaction constant. Until now, only fourteenth such decays participate in the world-average corrected Ft value. The strength of the transition ft is the product of the phase-space factor f, and the partial half-life of the transition t. The experimental half-life and branching ratio are included in the partial half-life t determination, while phase-space factor f depends on the electron capture energy Q_{EC}. The Q_{EC} energy has been in the close research circle of the ISOLTRAP mass spectrometer [K$^+$19]. From the past attempts to measure ^{70}Br isotope [A$^+$17] until a recent proposal to measure the ^{98}In isotope [N$^+$20]. The latter is the heaviest nucleus which has not been included in the worldwide average because of the lack of experimental information. The radiative and nuclear-structure-dependent corrections, such as $\delta_C, \delta_R^{'}, \delta_{NS}, \Delta_R^V$, are also indispensable inputs and have to be provided by theory.

The other topic where the mass measurements play a significant role is the neutrino mass determination [And18]. This has been a hot topic since the discovery of this particle. The lower limits on the neutrino mass can be set through a kinematic approach of the β-decay transitions. When the decay occurs, the nucleus emits the positron/electron and the electron neutrino/anti-neutrino. The smaller the transition energy the more precise the measurement can be. And again, this topic has been included in the scientific program of ISOLTRAP mass spectrometer [E$^+$08, B$^+$10].

To sum up, mass measurements play a significant role even in weak interaction studies.

1.1.3 The motivation for nuclear physics

At the beginning of the 20th century, scientists knew only the proton, the electron, and the photon [Rut20]. It took an enormous effort to develop an atomic model from a naive raisin pie model [Tho04] to the model we know now as the planetary model [Rut11]. Furthermore, it passed twenty years to discover neutron [Cha32] and start building the model to describe the modern understanding of the nucleus. It began from a naive liquid drop model [Wei35] until the discovery of magic numbers and shell-model outbreak [May48].

It is well known that the nucleus consists of protons and neutrons, and the simple sum of them should give the total mass of a nucleus. However, the actual nuclear mass is written as:

$$m_{nuc}(Z,N) = Z \times m_p + N \times m_n + \frac{B_{nuc}}{c^2} \tag{1.3}$$

m_{nuc} : the mass of a nucleus which has Z number of protons and N number of neutrons
m_p : the mass of a single proton
m_n : the mass of a single neutron
$\frac{B_{nuc}}{c^2}$: the binding energy of the nucleus

The last term in equation 1.3 is the nuclear binding energy, reflecting interactions inside the nucleus. Since the mass of the proton and the mass of the neutron are well known, mass spectrometrists obtain the binding energy and study the systematics of the deviations of the nuclear binding energies. These studies can tell us about the inner kitchen of the nucleus and how it is organized.

It has been observed that at some exceptional Z number of protons or N number of neutrons or both of them simultaneously, the nucleus reaches an extra gain in its binding energy. Those are the magic numbers, and they appear when protons or neutrons fill a shell [R$^+$18]. The latest example from ISOLTRAP is a recently measured ^{100}In isotope. With the Q-value of ^{100}Sn decay, the doubly magic origin of the tin isotope can be tested. However, this gain in the binding energy also appears on the sub-shell level [X$^+$19], as an example sub-shell closure in calcium isotopic chain measured at ISOLTRAP [W$^+$13a]. These shells and sub-shells are strongly affected by the interactions between nucleons. That leads to a nuclear structure effect, namely breaking of the shell order [M$^+$18]. There are five regions on the nuclear chart where modifications of the shell structure have been experimentally observed. They lie close to the neutron drip line at N= 8, 14, 20, 28, 40. This phenomenon has been in the focus of the ISOLTRAP research program [A$^+$19]. There is a further interesting effect that the mass measurements can study. There are particular regions on the nuclear chart where extreme deviations can be observed. For example, in light isotopes where the N/Z ratio is large, the neutrons can form a halo around the nucleus [O$^+$92, S$^+$08]. The same effect has been observed with protons forming the proton halo [K$^+$88, KE$^+$95]. An interesting effect has been seen when neutrons form a ”skin” on the nucleus surface [HKE98]. Driven by nucleon-nucleon interaction, the nuclei can form extraordinary shapes, such as pear-shaped nucleus [B$^+$20]. In this thesis’s frame, the ISOLTRAP mass spectrometer’s particular interest is the A=100 region known as the ”region of deformation” [M$^+$13a, DR$^+$17] and discussed in Section 3.1.

1.2 The nuclear binding energy

The nuclear binding energy can be generally expressed as a sum of different contributions:

$$\frac{B_{nuc}}{c^2} = B_0(Z,N) + B_1(Z,N) + \frac{-1^{Z+1}+1}{2}\delta_p(Z,N) + \frac{-1^{N+1}+1}{2}\delta_n(Z,N) \tag{1.4}$$

B_0, B_1 : the terms which link different theories
δ_p, δ_n : the terms which are responsible for odd-even staggering effect

For example, in the finite-range droplet model (FRDM), two terms B_0, B_1 can represent different contributions to the total binding energy. Such terms as the volume term, the surface term and other terms (the details are provided in Chapter 3) can be included as B_0 correction and B_1 will stay for deformed droplet shape. In the shell model, shell-corrections can also be included in B_0, B_1 terms. For example, B_0 can be considered as the result of independent particles orbiting in a spherical potential and B_1 represents the rest interactions. The δ_p, δ_n parts describe the odd-even staggering effect of protons and neutrons, respectively. This effect can be seen in figure1.2-(a) where at every even neutron number of calcium isotope there is a gain in the binding energy. This gain is due to two neutrons forming a pair. However, nuclear binding energy is a large quantity to study the underlying nuclear structure phenomena. As an example, the 20, 28 sell closures and 32 sub-shell closure are highlighted by vertical dash-lines in figure1.2-(a)) and they are not visible on the general trend of the nuclear binding energy. To access other nuclear structure effects mass spectrometriests use so-called mass filters.

One such filter is one proton/neutron separation energy:

$$\begin{aligned} S_p(Z,N) &= B_{nuc}(Z-1,N) - B_{nuc}(Z,N) \\ S_n(Z,N) &= B_{nuc}(Z,N-1) - B_{nuc}(Z,N) \\ \delta_{1n}(Z,N) &= S_n(Z,N) - S_n(Z,N+1) \end{aligned} \tag{1.5}$$

S_p, S_n : one proton and one neutron separation energy correspondingly
δ_{1n} : the one neutron shell gap

This filter is equal to the energy being required to remove one proton/neutron from the nucleus. Figure1.2-(b) shows the S_n energies for calcium isotopic chain. First, one can observe a more pronounced odd-even staggering effect of neutrons. Second, it shows significant drops in the trend of the one neutron separation energy at 20, 28 and 32 neutron numbers compared to other neutron numbers. In this case these drops reflect the shell and sub-sell closures. The amplitude of this drop can be described by the so-called one neutron shell gap in equation

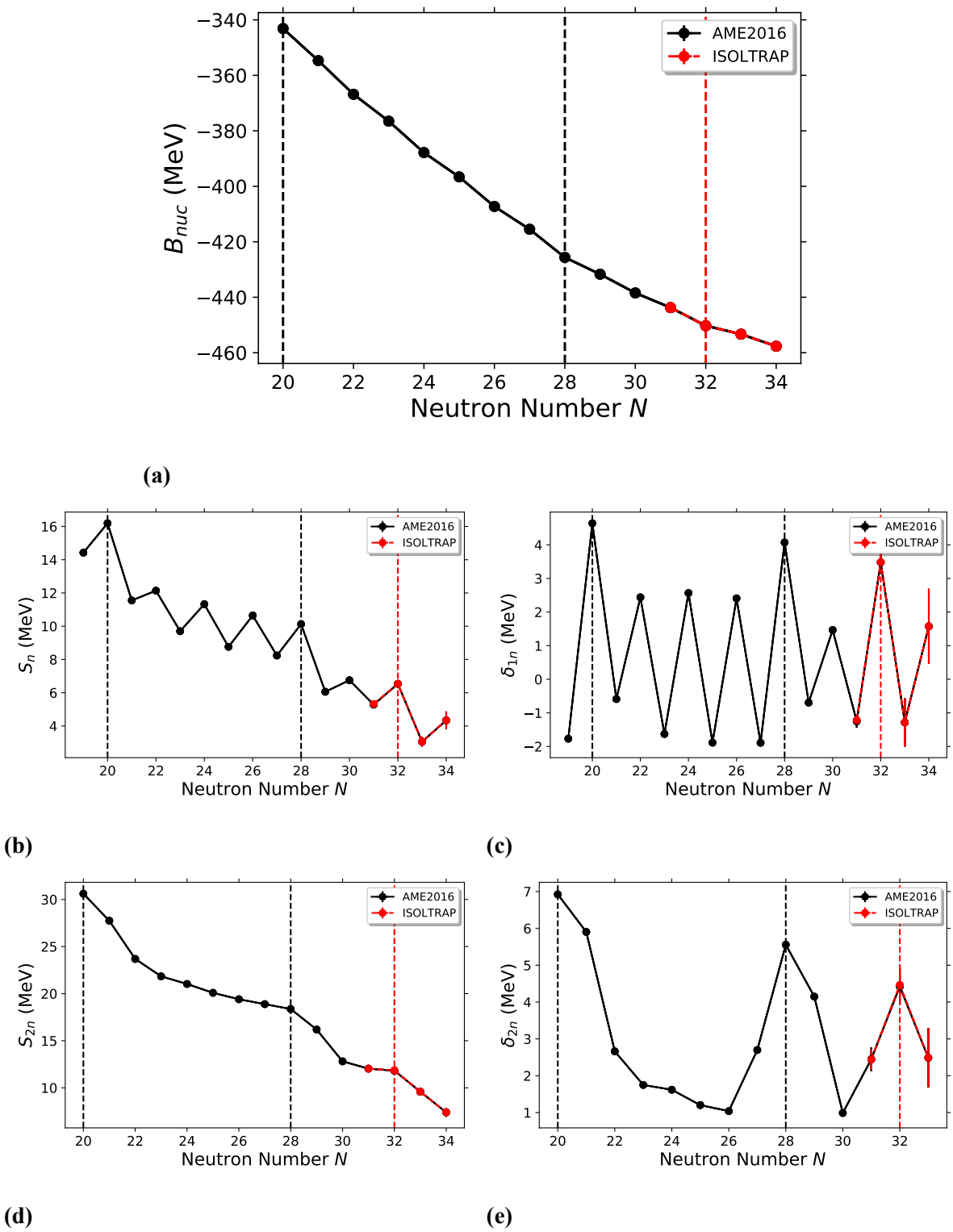

Figure 1.2. (a)- the trend of the binding energy in calcium isotopic chain [H^+17]. (b)- one neutron separation energy in calcium isotopic chain. (c)- one neutron shell-gap energy in calcium isotopic chain. (d)- Two neutron separation energy in calcium isotopic chain. (e)- two neutron shell-gap energy in calcium isotopic chain.

1.5. One can observe the magnitude of the changes through one neutron shell gap shown in figure1.2-(c).

The second filter is the two proton/neutron separation energy. This filter is equal to the energy being required to remove two protons/neutrons from the nucleus:

$$\begin{aligned} S_{2p}(Z,N) &= B_{nuc}(Z-2,N) - B_{nuc}(Z,N) \\ S_{2n}(Z,N) &= B_{nuc}(Z,N-2) - B_{nuc}(Z,N) \\ \delta_{2n}(Z,N) &= S_{2n}(Z,N) - S_{2n}(Z,N+2) \end{aligned} \tag{1.6}$$

S_{2p}, S_{2n} : two protons and two neutrons separation energy correspondingly
δ_{2n} : the two neutron shell gap

The effect of the S_{2n} filter can be seen in figure1.2-(d). First, this filter removes the odd-even staggering effect because in the equation 1.6 only odd or even nuclei are included. Second, this filter together with two neutron shell gap makes the nuclear structure effects more visible in the calcium isotopic chain in figure1.2-(e).

However, these filters are also sensitive to other nuclear structure effects. For example, the trend of S_{2n} mass filter in chromium isotopic chain [M$^+$18] shows approximately the same behavior as for neutron-rich calcium isotopes. There is a change in the two neutron separation energy at N=36. This region is so-called "island of inversion" where the inversion of shells occurs. The trends in two neutron separation energy in A=100 region show that the nucleonic system becomes less bound. These changes represent so-called "island of deformation" [M$^+$16a]. The investigation of the region requires the usage of complementary information.

To overcome the lack of information through the direct use of the mass filters, complementary properties are involved. As an example, the charge radii of the nuclei, the angular momentum, the excitation spectrum actively participate in the understanding of nuclear phenomena. A=100 region is an excellent example of such synergy. One can draw complementary nuclear observables, such as the charge radii and the energies of the first 2^+ excited states. For simplicity these properties are shown in figure 1.3 only for zirconium isotopes.

Let first have a look at two neutron separation energy in figure1.3-(a). The decreasing trend of the S_{2n} energy up to the N=59 does not show any irregularities. However, the sudden increase at N=60 indicates a structural change, especially, if taken into account the pronounced increase in the charge radii at N=60 (figure1.3-(b)). This increase of the charge radii suggests that neutrons start occupying states of much larger radial extension and this results in the low lying first 2^+ excited state at N=60 (figure1.3-(c)). The strong evidence of the onset of the deformation at N=60 in zirconium chain is a ratio between first 4^+ and first 2^+ excited states

which rises to almost 3.33 (figure1.3-(d)). This indicates that zirconium isotopes act as a rigid rotor at N>=60.

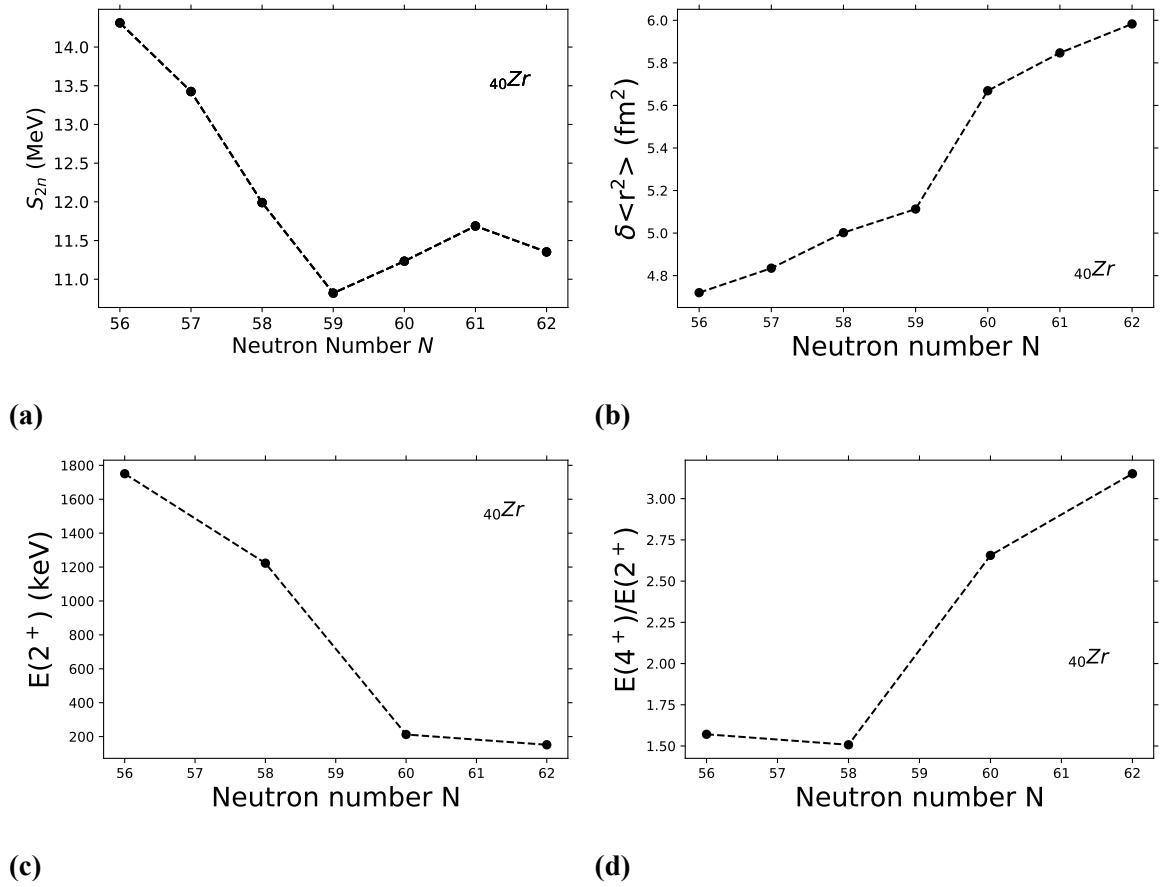

Figure 1.3. (a)- two neutron separation energy in zirconium isotopic chain [M$^+$21]. (b)- charge radii in zirconium isotopic chain [A$^+$13]. (c)- the energy of the first 2^+ excited state in zirconium isotopic chain [Lab]. (d)- the ratio between 4^+ and 2^+ excited states in zirconium isotopic chain.

To conclude, the large amount of data on the nuclei complements and supports interpretations of observed phenomena. Different points of view from different nuclear physics fields form the basis of the modern understanding of nuclear structure.

1.3 Subject of this work

In the frame of this thesis precise mass measurements of exotic nuclei for the nuclear binding energies determination will be discussed. The radioactive ions were produced at ISOLDE radioactive ion beam facility. ISOLDE is the Isotope Separation On-Line (ISOL) type of facility where exotic nuclei are produced through nuclear reactions of relativistic protons with the thick target material. The isotopes from the lightest up to heavy uranium can be produced. The ISOLTRAP mass spectrometer measures the masses of these isotopes by applying different

techniques. In this work, the focus is set on the multi-reflection time of flight (MR-ToF) mass spectrometry and the time of flight ion cyclotron resonance (ToF-ICR) technique.

Although the ISOLTRAP mass spectrometer has a diverse research program, krypton isotopes for nuclear structure objectives are discussed in this work. Experimental results are compared to the theoretical calculations.

Theoretical models rely on the different approaches which can be grouped in macroscopic, macroscopic-microscopic and microscopic methods. In 1935 German physicist Carl Friedrich von Weizsäcker proposed his famous formula [Wei35] based on liquid drop theory and empirical measurements. This is an example, of a macroscopic model. This semiempirical mass model went through modification to include microscopic parts which led to the development of the macroscopic-microscopic model namely the finite-range droplet model (FRDM) with the latest upgrade FRDM2012 [M$^+$16b]. The results of this global model will be compared particularly with A=100 region.

The self-consistent mean-field models with Skyrme type interactions are regarded as microscopic approaches. The predictions of the global HFB31 model [G$^+$13a] with Skyrme type interaction are also compared to experimental values in A=100 region. The SLy4 parametrization [S$^+$03] of the Skyrme force has been specially tailored for the nucleon-nucleon interaction and the prediction of this model is also shown.

A new model based on the density functional theory(DFT) and Skyrme type force resulted in the latest UNEDF0/UNEDF1 calculations [K$^+$10] and is particularly interesting in predicting nuclear properties in deformation regions. The UNEDF0/1 model was adjusted on spherical and deformed nuclei which makes it particularly interesting for A=100 region.

The Gogny force is well presented in the literature. There is a subshell-closure at N=56 and predictions of the Gogny D1S model [B$^+$91] can be tested on both subshell-closure and the deformation.

Finally, the progress on the machine learning techniques made it possible to establish the Svmin method [G$^+$06]. The machine learning techniques and Gogny interaction make it possible to provide new mathematical solutions and reduce the computational time [L$^+$20a].

In this work, the experimental results from the ISOLTRAP mass spectrometer on the krypton isotopes are compared to the aforementioned theoretical calculations.

The thesis is organized into three chapters:

- The first chapter describes different applications of precise mass measurements focusing on nuclear physics particularly on nuclear binding energy. The different mass-filters and accessible nuclear structure effects are also discussed. The complimentary nuclear data and their application for the investigation of the nuclear deformation are drawn.

- The second chapter introduces the ISOLDE facility and the ISOLTRAP mass spectrom-

eter. It describes the main components and techniques used for isotope production and mass measurements. It also introduces the data analysis of the IS532 [B^+14] and IS642 [A^+17] experimental campaigns. The source of systematic uncertainty of MR-ToF mass spectrometry is studied and discussed. The alignment of the horizontal beamline and the developments of a new device for control of the resonance frequency of the buncher device are also provided.

- The third chapter provides the detailed study of the A=100 deformation region through high precision mass measurements of neutron-rich krypton isotopes. It introduces the data analysis of $^{96-98}$Kr isotopes and investigations of sources of systematic uncertainty of the MR-ToF mass measurement technique. It applies a general specification of different theoretical models and interpretation of the results of their calculations. Finally, the experimental and theoretical results are compared.

- The last chapter provides a summary of the investigations of the work and an outlook.

Chapter 2

The ISOLTRAP Mass Spectrometer

Scientists have been interested in ”earthly” compounds since the Middle Ages. Centuries after centuries, they discovered new stable elements that could be found in mines or obtained through chemical reactions. Following the discovery of radioactivity, new elements have been found in nature [Kas13]. Even today, identifying chemical properties is required to include the new element in the periodic table [Oga10]. These elements form the Periodic table and nuclear centers try to find new elements. To list some of these facilities: Lawrence Berkeley National Laboratory [S$^+$09c], Joint Institute for Nuclear Research [OK15], GSI Helmholtzzentrum fur Schwerionenforschung [H$^+$12].

The isotopes have the same chemical properties and the same number of protons as a stable element but a different number of neutrons. The study of these isotopes led to discovering other parts of the nuclear chart away from stability. The production of rare isotopes requires different methods and techniques. One such technique is an in-flight production method and separation of radioactive ion beams. The synchrotron or a linear accelerator is used to accelerate a primary beam to the energy of hundreds of MeV/u. The beam is focused on a relatively thin production target where isotopes of interest are produced via projectile fragmentation or in the case of ^{238}U primary beam also via fission reactions. The positively charged products are separated by so-called $B\rho - \Delta E - B\rho$ separation, where $B\rho$ is the magnetic rigidity analysis, and ΔE are energy losses in a specially shaped material. The degrader is needed for an additional Z-selectivity. The world-famous facilities based on such method are GANIL, GSI, LEGNARO, RIKEN, IMP [BNVD13].

2.1 The ISOLDE facility and isotope production

The isotopes measured by the ISOLTRAP mass spectrometer and presented in this work have been produced at the ISOLDE facility at CERN [BB18]. The visual aid is shown in figure 2.1. The production technique applied at ISOLDE differs from the in-flight method. Instead

of hitting a thin target with an accelerated heavy primary beam, the isotopes of interest are produced by bombarding the thick target with protons of 1.4 GeV delivered by the Proton Synchrotron Booster(PSB). The isotopes are produced via spallation, fragmentation, or fission nuclear reactions. The structure, as well as the material of the target, varies depending on the demands [Got16]. For example, UC_x target was used to produce neutron-rich krypton isotopes; the tantalum foil target was used to produce scandium isotopes; bromine and arsenic isotopes were produced from zirconium oxide powder target. To make the production of neutron rich isotopes more efficient, tungsten rods can be installed parallel to the target body. They act as a neutron converter. The target is heated up to 2000 °C to make the diffusion and effusion processes more efficient. Via a transfer line, which is also heated, neutral atoms enter the ionization part of the target. The isotopes' production rate is limited by the chemical nature of the isotope of interest on the one hand and by the half-life on the other. Some isotopes interact with the target material so that they do not defuse out. While for the others, it takes so long that they decay before being ionized.

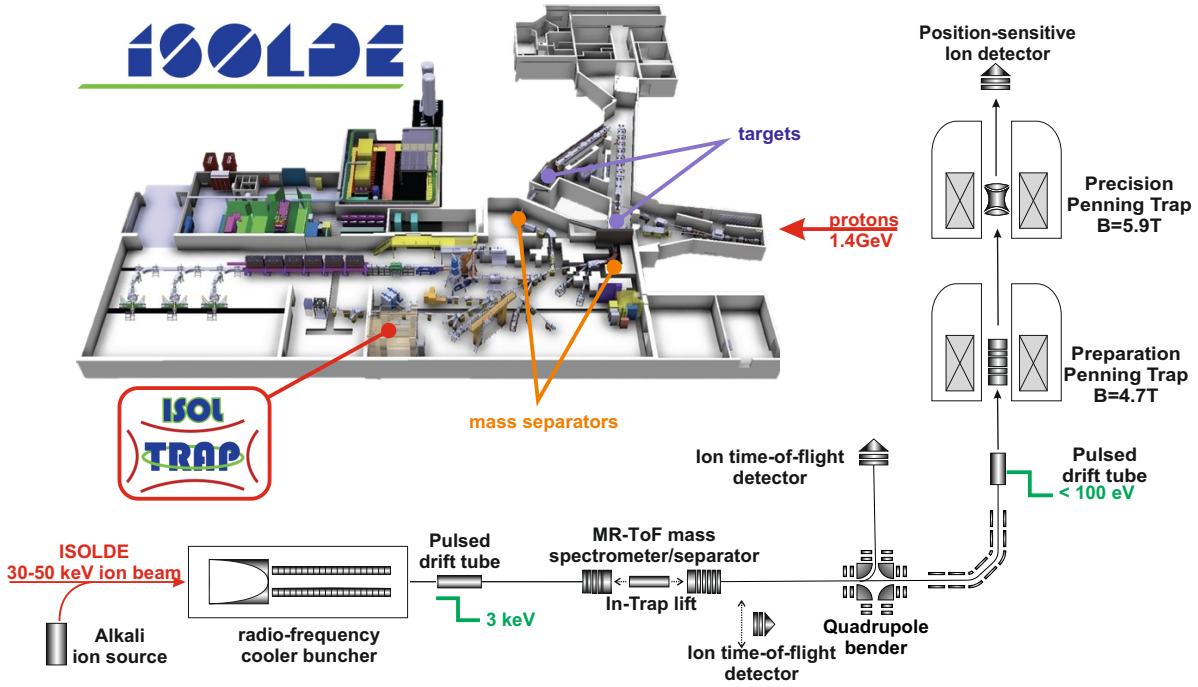

Figure 2.1. The schematic representation of the ISOLDE facility and the ISOLTRAP mass spectrometer. The recent installation of the high ISOLDE is not included in the figure [Jon17].

A neutral atom effuses in the hot transfer line to the ionization section. At ISOLDE, three different techniques are used to produce charged ions. One technique is the Resonance Ionization Laser Ion Source (RILIS) technique [F^+17a, M^+13b, MP^+18]. The ions are created by kicking out an electron. The level structure of an atom is unique for every isotope. The proper laser frequency adjustment makes the ionization method highly selective and efficient. The

second technique is surface ionization, when atoms get ionized by contacting the heated wall of the ion source cavity. The only parameter which can be varied is the temperature of the wall. Therefore, this method relies on the chemical properties of the element. For example, the alkali metals quickly lose their electron to the heated plate and get singly charged. The third method of ionization is plasma ionization. This technique is exceptionally efficient for ionizing gasses. The atoms enter the plasma ion source volume, consisting of an anode and a cathode. Electrons get accelerated from the anode to the cathode. These electrons create an arc discharge, and neutral atoms get ionized. A particular type of plasma ion source (VADIS) is used at the ISOLDE facility. It has a large working volume and less graphite, plus a water-cooled transfer line to reduce the contamination rate [P$^+$10, DG$^+$16].

The target and the ion source are floated with 30-60 kV; therefore, singly/doubly charged ions exiting the production section have the equivalent energy. The high-resolution separator(HRS) and general-purpose separator(GPS) are the dipole based magnetic separators with resolving power of 5000 and 1000, respectively [K$^+$00]. The radioactive beam of isobars can be selected by adequately adjusting the devices. The continuous isobaric beam is delivered to the ISOLTRAP setup [M$^+$08, K$^+$13]. The ISOLTRAP is a multi-functional mass spectrometer that consists of four different traps for cooling, bunching, isotope separation, and precise mass measurements. The details are provided in the following sections.

2.2 The buncher device

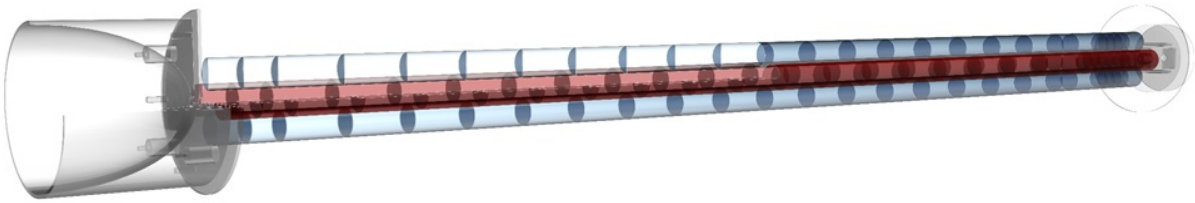

Figure 2.2. The basic layout of the RFQ buncher. It consists of an egg-cup electrode, rod system, and ejection electrodes [And18].

The radiofrequency quadrupole (RFQ) buncher is a linear Paul trap system filled with He buffer gas [H$^+$01b]. The device's primary purpose is to form a bunched beam and cool it down by collisions with buffer gas [S$^+$91a]. The entire device is placed inside a high voltage cage powered to 30-40 kV to adjust the setup to the energy of the incoming ISOLDE beam. Once ions enter the buncher, the RFQ field radially confines the ions in the device [Daw93]. The particular DC potential of a well configuration axially guides ions (see figure 2.3). The ions collide with He buffer gas, lose the energy and slowly accumulate in the potential well. The accumulation time varies between species of interest; however, it is in the order of tens of milliseconds. After

the bunch is formed, the DC potential of the last segment is switched off, and ions are ejected from the buncher device.

The RFQ consists of four segmented rods to which a voltage $\Phi_0(t) = U_{DC}(r,z) \pm V_{RF}(r) sin(\omega t)$ is applied. Every rod is divided into twenty-six segments. The segments form five groups: Bank 1, Bank 2, Segment 23, B-Trap, and Segment 26 to create the potential well. Equation 2.1 describes the evolution of the potential in the buncher device. The equation of ion motion 2.1(2) can be transformed to the standard Mathieu equation 2.1(3). The stable solution of this equation leads to stable ion trajectories in x and y directions and depends on $a_u = a_x = -a_y$ and $q_u = q_x = -q_y$. One can notice that a stable solution mostly depends on the ion mass and U_{DC}, V_{RF} amplitudes [BH08].

$$\Phi(\vec{r},t) = \frac{\Phi_0(t)}{2} * \frac{x^2 - y^2}{{r_0}^2} \tag{2.1}$$

$$\ddot{x} + \frac{e}{m{r_0}^2}\Phi_0 x = 0 \quad \text{and} \quad \ddot{y} - \frac{e}{m{r_0}^2}\Phi_0 y = 0$$

$$\frac{d^2u}{d\xi^2} + (a_u - 2q_u \cos 2\xi)u = 0$$

$\mathrm{a}_u = a_x = -a_y = \frac{4eU_{DC}}{m\omega^2{r_0}^2}$: constant which depends on amplitude of DC potential and ion mass
$\mathrm{q}_u = q_x = -q_y = \frac{2eV_{RFV}}{m\omega^2{r_0}^2}$: constant which depends on amplitude of RF potential and ion mass
$\xi = \frac{\omega t}{2}$: constant which depends on the period of the RF signal

This is the principle of using the buncher as a mass filter because only a certain range of masses can be stored in x and y direction for a given U_{DC}, V_{RF} parameters. The mass scan line (figure 2.3) is described by $a = \frac{2U_{DC}}{V_{RF}}q$ and depends on the Paul trap parameters. The closer the line to the hill, the better is the resolving power. Masses outside this stable region will be lost in x, y, or both directions. Stored ions oscillate around the z-axis with finite amplitude. Since ions are fixed in x and y directions, the amplitude decreases in the z-direction. The length z depends on the interactions of ions with the buffer gas.

Therefore, such parameters as the pressure of the buffer gas and applied U_{DC}, V_{RF} play a crucial role in cooling ions and bunch formation. These parameters are the subject of the following subsections.

2.2.1 Pressure of the buffer gas

If U_{DC}, V_{RF} guides the ions through the RFQ-trap and affects the bunch formation, the He buffer gas is responsible for cooling down the beam [S$^+$91a]. At first, the dependency of the count rate on the pressure has been taken (figure 2.4-(a)). There is an increase in the count rate when the He pressure increases. One of the most crucial parameters of the ISOLTRAP mass spectrometer

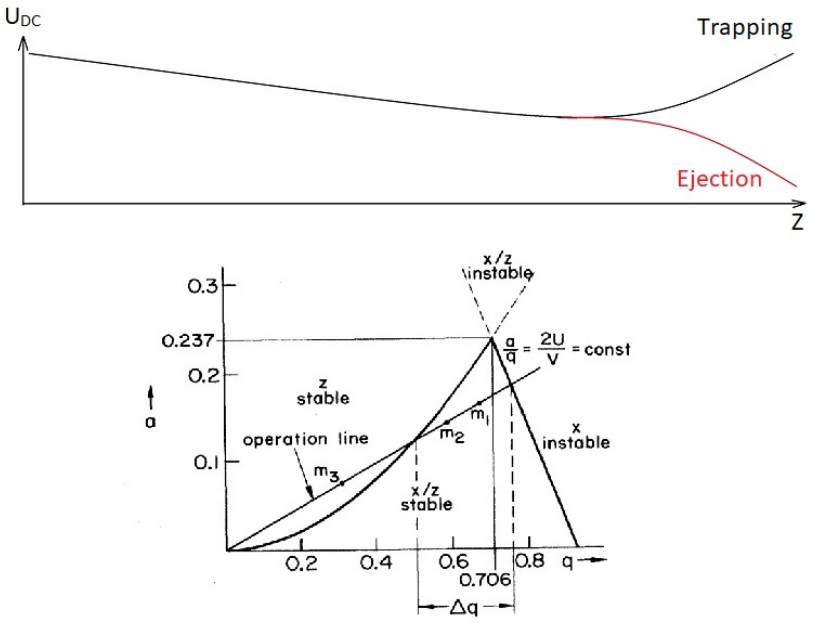

Figure 2.3. Top: schematic representation of the DC potential for axial confinement and bunch forming. Bottom: the triangle of stability for ion guiding in radial direction [Wol90].

is the achievable mass resolving power which is the quantity that allows separating the isobars in the beam. For the evolution of the resolving power, the number of counts has to be fixed because the resolving power depends on the number of counts. Figure 2.4-(b) shows how the resolving power depends on the pressure. It gets better with the pressure increase.

As second, the taken spectra were fitted with Gaussian and Exponential Gaussian Hybrid probability density functions using maximum likelihood estimation (details are in Section 2.3). The idea was to check how the peak shape asymmetry evolves with pressure. The criterion was chosen to be the difference between the mean values of Gaussian and exponential gaussian hybrid (EGH) probability density functions. As one can see from figure 2.4-(c), the difference is getting smaller the more He pressure is presented.

2.2.2 Resonance frequency

The second parameter to control in the buncher is V_{RF} amplitude applied to the buncher rods. In order to create the quadrupolar field, the RF frequency applied pair-wise to rods such that opposite electrodes have the same polarity. This is achieved by five matching boxes, where the $\Phi_0(t)$ has been created by splitting the transformer into two parts and grounding the common middle electrode. This configuration creates an RF signal of the same amplitude but the opposite sign. The typical scheme is shown in figure 2.5 top. In parallel to the transformer, the variable capacitor and buncher rods with their own capacitance are connected. According to equation

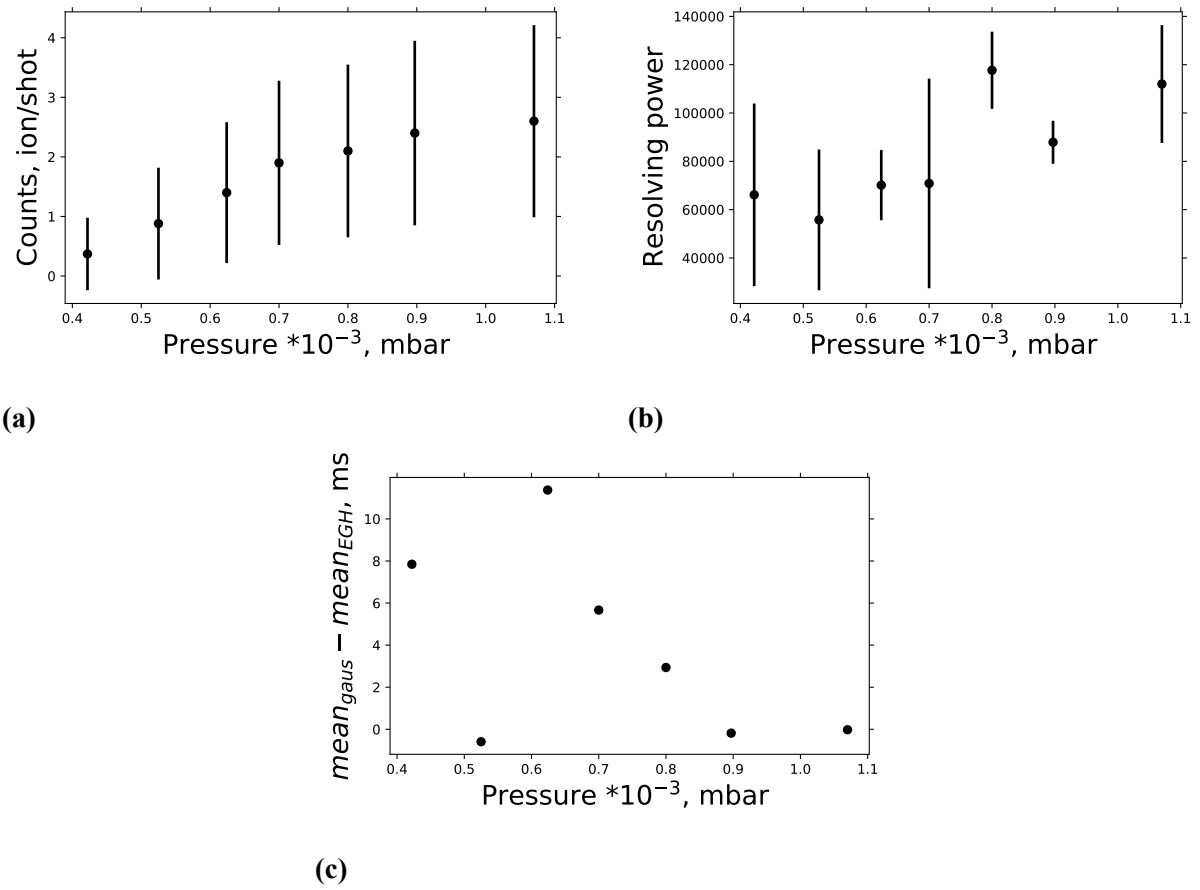

Figure 2.4. (a)- dependency of efficiency on pressure. (b)- evolution of the resolving power with pressure. (c)- evolution of the difference between mean values of Gaussian and exponential gaussian hybrid probability functions, errors are smaller the the sizes of points.

2.2, the resonance frequency of the circuit can be controlled by changing the capacitance of C_{var} because $C_{total} = C_{var} + C_{buncher}$ (C4 and C3 in figure 2.5 top). This gives access to the mass scan line of the triangle of stability, where the slope of the line depends on $\frac{2U_{DC}}{V_{RF}}$ ratio.

$$f_0 = \frac{1}{2\pi\sqrt{L_{total}C_{total}}} \tag{2.2}$$

The variable capacitor has many metallic plates which form layers with an air gap in-between as a dielectric. By rotating the layers, one changes the distances between them, and because $C_{var} = \varepsilon_0 \frac{KS}{d}(n-1)$, the capacitance can be tuned. ε_0 is the permittivity of free space constant, K is the dielectric constant of the material in the gap (air), S is the area of the plates, and d is the distance between the plates, n is the number of layers. C_{var} can be varied between 30 and 80 pF. $C_{buncher}$ depends on the length of the segment of the buncher rods. For Bank 1, Bank 2, it is 500 pF, and for Segment 23, B-Trap, Segment 26 is 100pF. The inductance of the transformer varies between segments as well and $L_{total} = \mu_0 N K \frac{\pi D^2}{4d}$, where μ_0 is the vacuum permeability, N is the number of windings, D the diameter of the coil, d the diameter of the

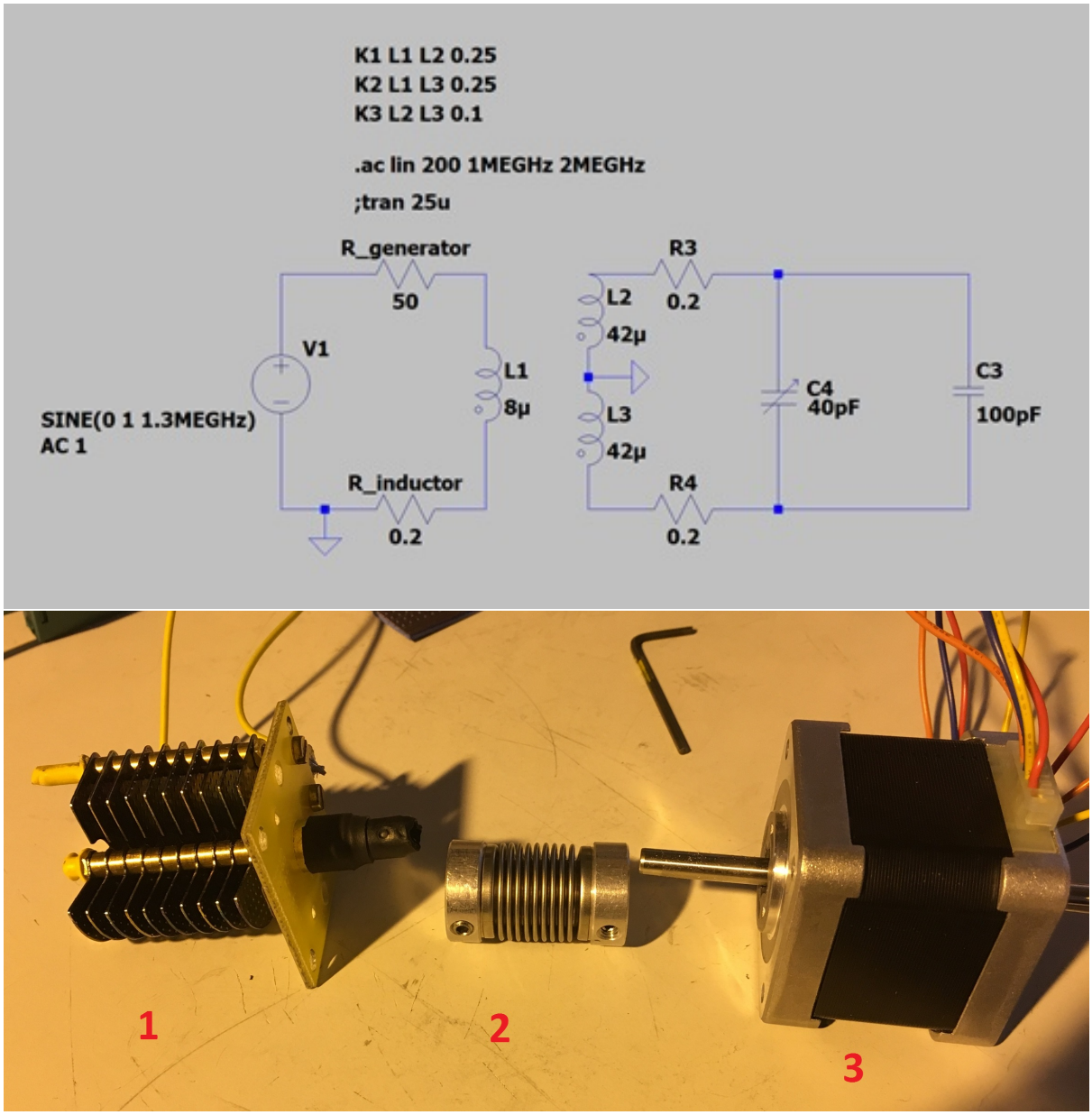

Figure 2.5. Top: the electronic scheme of the resonance circuit used for B-trap. The same schematic was used to simulate the frequency range in the LTspice software. The main elements of the circuit are discussed in the text. Bottom: 1- variable capacitor, 2- the coupler, 3 - the stepper motor.

wire, and K is a factor which depends on the ratio between the diameter and the length.

The idea was to couple the variable capacitor and the stepper motor as shown in figure 2.5 bottom to tune via LabVIEW and Arduino software the resonance frequency. This would allow using the matching boxes as steerer or lens to manipulate the count rate but based on a principle of the mass separator (according to equations of motions 2.1 and triangle of stability in figure 2.3). On top of this, there was a proposal to use the capacitor-diode, where the capacitance depends on the voltage applied to the diode base. Instead of mechanically turning the capacitor,

one could change the capacitance by changing the voltage applied to the base. This electronic component should survive a radio frequency signal of high voltage (more than 200 V), and no such capacitor-diode was found available on the market.

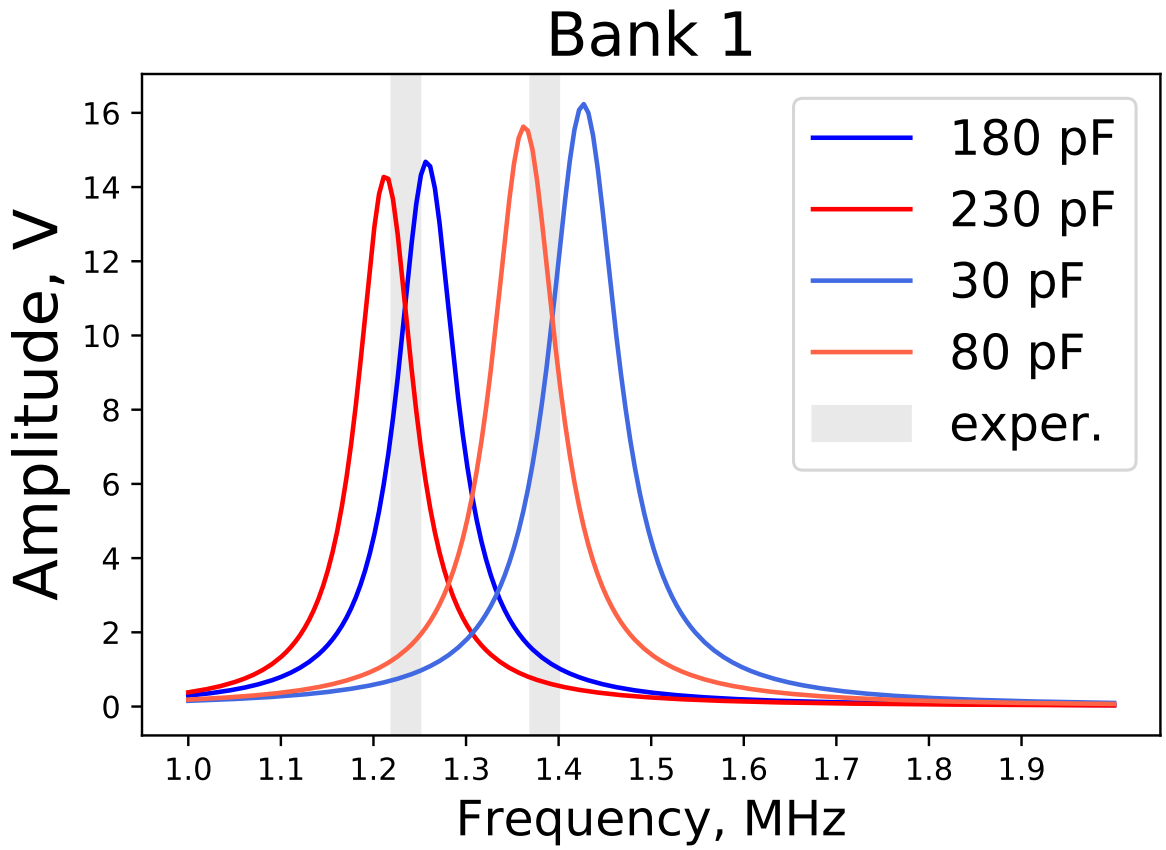

Figure 2.6. The results of the simulation in LTspice software. The capacitor varies between 30 and 80 pF. The V_{RF} amplitudes for minimum and maximum of the achievable capacitance are shown on the plot. The gray band represents the experimental results with the high voltage amplifier.

To obtain the value of the resonance frequency with chosen circuit parameters and to check the achievable frequency range, the simulation was performed in the LTspice software (figure 2.5 top). The variable capacitor is named $C4$, the buncher's rods capacitance is named $C3$. This schematic corresponds to either Segment 23, B-Trap or Segment 26 because they have the same length of the rods. L1, L2, L3 are the inductances of the solenoids while K1, K2, K3 are the coupling parameters. R3, R4, $R_{generator}$, $R_{inductor}$ are interior resistances of the elements. Finally, V1 is a frequency generator producing the sinusoidal signal of 1-volt amplitude and different ranges of frequencies. The simulation was also performed for $C3$=500 pF and the result is shown in figure 2.6. With given circuit parameters, the Banks' frequency could be varied between 1.36 and 1.43 MHz, while for Segment 23, B-trap, and Segment 26 it was 1.05-1.22 MHz. Therefore, an additional capacitor of 150 pF was added in parallel in Bank 1 and

Bank 2 resonance circuits. That allowed an expansion of the frequency range to the lower values of 1.25-1.3 MHz. The main results are listed in table 2.1. After the matching boxes were constructed, their performance was checked with a frequency generator and a frequency amplifier. The results are shown as a grey band in figure 2.6 and agree with the simulation.

Finally, the device was installed in place at the ISOLTRAP setup. It was possible to tune the frequencies online. As expected, the count rate depends on the resonance frequency, which depends on the configuration of the layers of the variable capacitors. Figure 2.7 shows the current amplitude V_{RF} applied to the buncher rods with the help of the new device. As one can see, the B-trap region plays the most significant role in the bunch forming. It was possible to tune capacitors so that the maximum number of ^{133}Cs ions have been counted, but at the same time, ^{85}Rb ions were utterly lost in the buncher device. That was the expected result from the triangle of stability.

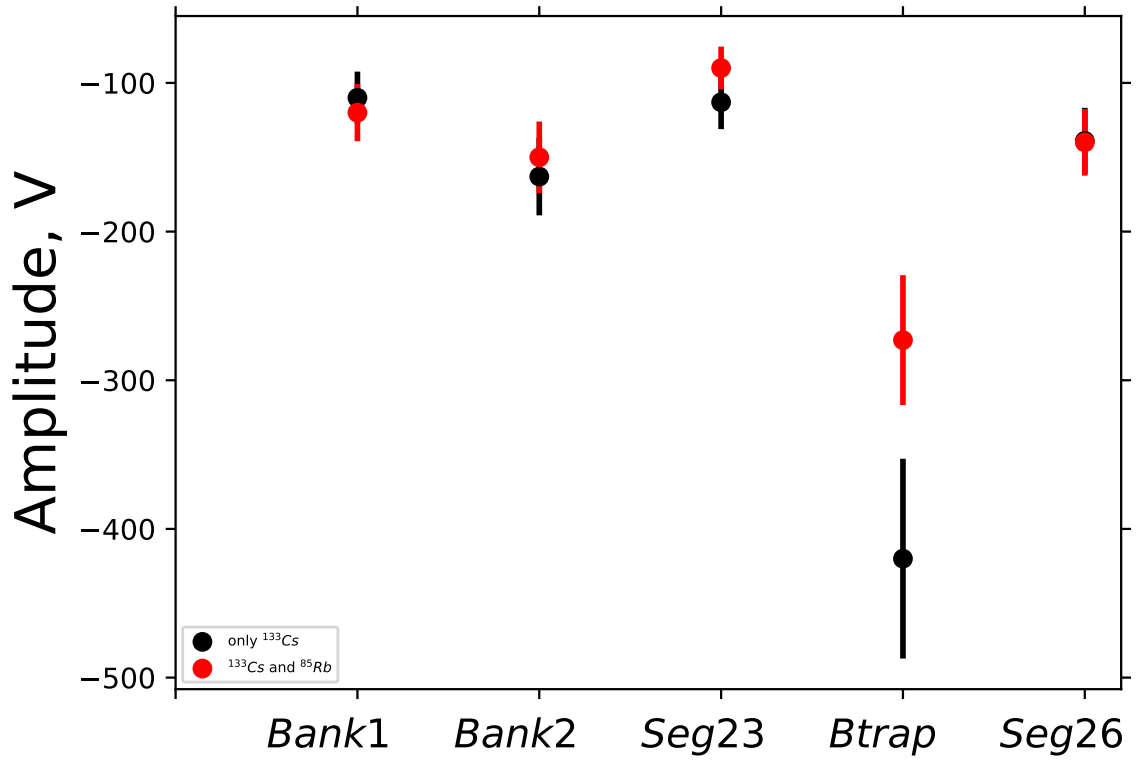

Figure 2.7. Top - the amplitude V_{RF} of the resonance frequencies reached on the segments of the buncher. Black dots correspond to the amplitude on the rods when the count rate was maximized on the ^{133}Cs ions; red dots correspond to the amplitude when both ^{85}Rb and ^{133}Cs ions were observed in the same bunch.

Table 2.1. The achievable frequency ranges of new build matching boxes. The first column represents the capacitance of the variable capacitor and does not include the capacitance of segments.

	Resonance Frequency, MHz				
Capacitance, pF	Bank 1	Bank 2	Segment 23	B-trap	Segment 26
30	1.435	1.395	1.225	1.235	1.185
80	1.395	1.355	1.095	1.105	1.075
180	1.295	1.285			
230	1.255	1.245			

2.3 The multi-reflection time of flight device

After the bunch of ions is extracted from the buncher, it enters the pulsed drift tube where the ions experience deceleration down to 3.2 keV by switching the drift tube's potential. Downstream there is a multi-reflection time of flight (MR-ToF) device [W$^+$12] which has two working modes. First, it can be used as an isobaric separator [W$^+$11b]. Second, the time of flight spectrum of ions can be recorded, which allows using the device as a mass spectrometer on its own [W$^+$13b].

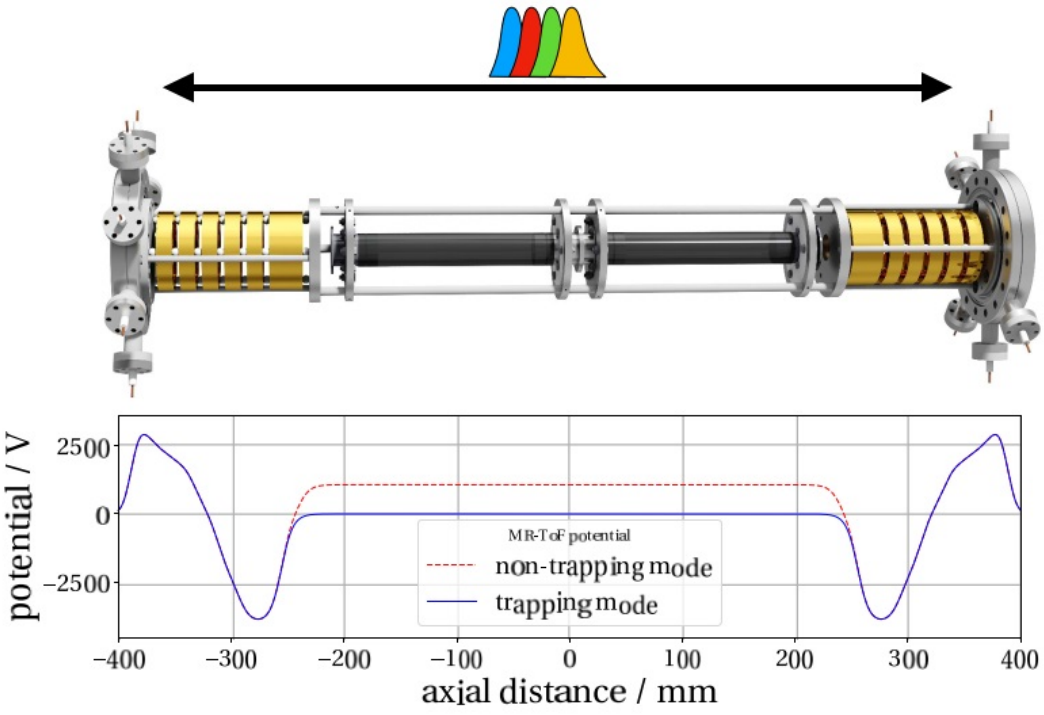

Figure 2.8. Top: the multi reflection time of flight device. Bottom: the in trap-lift technique [W$^+$13b] to store the bunch of ions between electrostatics mirrors.

The MR-ToF device schematically shown in figure 2.8. The bunch of isobars is trapped in the middle of the device by applying in trap lift potential [W$^+$17]. Once ions are stored, they revolve between two sets of five by five electrostatic mirrors. The fly-path of ions is increased to kilometers, and eventually, the isobars with a slightly different mass can be separated. The main parameter of the device is the mass resolving power $\frac{m}{\Delta m}$. At ISOLTRAP, the MR-ToF device reaches the resolving power of 130000. The trap lift potential can be set so that only the ions of interest are transported to the next device, namely the precision Penning trap. This allows to eliminate the contaminant species and increase the precision of the mass measurements in the Penning trap.

The advantage of the MR-ToF device is that it can also be used as a mass spectrometer. To achieve this goal, an electron multiplier detector is installed in combination with a multi-channel analyzer of the MCS6A model in the ISOLTRAP beamline. One of the most crucial advantages of the MR-ToF mass spectrometry that it is fast. Typically only 20 ms are required to split up the isobaric beam, which benefits when masses of fast decaying isotopes have to be investigated. Another advantage is that the device can perform the mass spectrometry of beams with low yields. The time of flight of an ion depends on its $\frac{m_i}{q_i}$ ratio according to the equation 2.3

$$t_i = \alpha\sqrt{\frac{m_i}{q_i}} + \beta \tag{2.3}$$

t_i : the time of flight of the ion
m_i : the mass of the ion
q_i : the charge of the ion
α, β : calibration constants

To calibrate the device, at least two reference ions with well-known masses are needed. For this purpose, an offline alkali source is installed. It provides beams of ^{39}K, ^{85}Rb and ^{133}Cs ions. The mass of the ion of interest can be determined through equation 2.4. However, to minimize the uncertainties coming from different trajectories of the offline and online beams, usually, one ToF spectrum from the offline ion source and one ToF spectrum from online measurement are used. Since the uncertainties of the reference masses contribute to the uncertainty of the mass of ion of interest, the measured mass is calculated as a C_{ToF} ratio.

$$\sqrt{\frac{m_i}{q_i}} = C_{ToF}\Delta_{Ref} + \frac{1}{2}\Sigma_{Ref} \tag{2.4}$$

$C_{ToF} = \frac{2t-t_1-t_2}{2(t_1-t_2)}$: depends only on the ToF's of the ion of interest and the reference
$\Delta_{Ref} = \sqrt{\frac{m_1}{q_1}} - \sqrt{\frac{m_2}{q_2}}$: depends only on the mass over charge ratio of reference ions
$\Sigma_{Ref} = \sqrt{\frac{m_1}{q_1}} + \sqrt{\frac{m_2}{q_2}}$: depends only on the mass over charge ratio of reference ions

2.3.1 The statistical uncertainty

The MCS6A card records counts and builds a histogram, the binning of which is equal to 0.8 ns based on the card's resolution. The analysis based on binned maximum likelihood estimation was performed. The method assumes that the distribution $P_i(\theta)$ with θ as parameters is Poisson distributed, and the probability to observe the event is given within likelihood function. The maximization of this function will result in the most likely parameters of the distribution [Myu03].

The experimental data are represented by the number of counts in the chosen time of flight window (figure 2.9). As a standard approach, all MR-ToF spectra are fitted with Gaussian distribution by applying binned maximum likelihood estimation. The outcome of the fitting procedure is a mean value of the distribution (most probable time of flight), the sigma value of the distribution and its statistical uncertainty.

$$P_i(\theta) = P(x, \mu, \sigma) = \frac{1}{\sigma\sqrt{2\pi}} e^{-\frac{1}{2}(\frac{x_i-\mu}{\sigma})^2} \tag{2.5}$$

2.3.2 The systematical uncertainty

One of the sources of systematical uncertainty comes from the voltage applied to the mirrors of the MR-ToF device [W$^+$20]. The studies show that the most significant influence on the trajectories of the ions inside the device comes from the voltage applied to the last mirror [W$^+$12]. The last mirror is a place where ions reflect, and the instability of the applied voltage results in the time of flight distortions. Therefore, it is essential to take one reference peak from online spectra (some stable isobars are always presented) and a reference peak from an offline source. This shift is on the level of 1 ns. To include the error to the C_{tof} ratio, the partial derivatives are taken and multiplied by the corresponding statistical uncertainties.

$$\sigma_{C_{ToF},stat} = \sqrt{(\frac{\partial C_{ToF}}{\partial t})^2\sigma_t^2 + (\frac{\partial C_{ToF}}{\partial t_1})^2\sigma_{t_1}^2 + (\frac{\partial C_{ToF}}{\partial t_2})^2\sigma_{t_2}^2} \tag{2.6}$$

$\frac{\partial C_{ToF}}{\partial t} = \frac{1}{t_1-t_2}$: the first coefficient
$\frac{\partial C_{ToF}}{\partial t_1} = \frac{t_2-t}{(t_1-t_2)^2}$: the second coefficient
$\frac{\partial C_{ToF}}{\partial t_2} = \frac{t-t_1}{(t_1-t_2)^2}$: the third coefficient

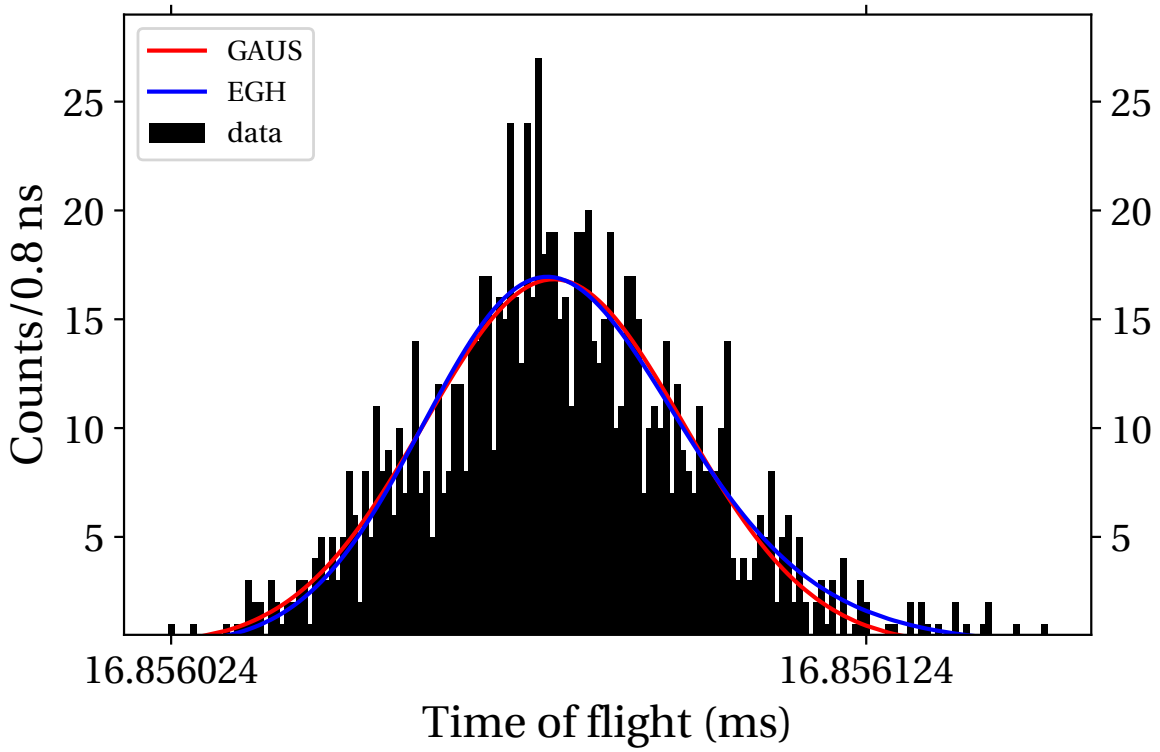

Figure 2.9. As an example, the time of flight spectrum of ^{49}Sc ions fitted by Gaussian and Exponential Gaussian Hybrid fit functions.

As it said earlier, the peak shape of the time of flight does not follow Gaussian distribution [LJ01]. One of the reasons can be the buncher device, which introduces the asymmetry through collisions with the buffer gas. The corresponding investigations are described in previous chapters and are still ongoing. To include the systematic shift of the mean time of flight value as the systematic uncertainty, another probability density function was used. A characteristic example is shown in figure 2.9. The exponential decay function well describes the right tail. The full function consists of the normal distribution on the left side and the exponential tail on the right side. This is the so-called exponential Gaussian hybrid (EGH) probability density function. The difference between C_{ToF} computed from Gaussian and EGH fit functions is taken as systematic uncertainty and is added in quadrature to the statistical uncertainty.

$$\sigma_{C_{ToF},pdf} = C_{ToF,Gauss} - C_{ToF,EGH} \tag{2.7}$$

The number of counts which are taken to build the histogram also affects the fitting procedure. The bigger the fitting window is, the more probable the situation when too much of the data is included and the background dominates the total distribution. On the contrary, a small fitting window may result that not all data is included in the fitting routine. For this purpose, the study was conducted on the evolution of the output Gaussian parameters depending on the

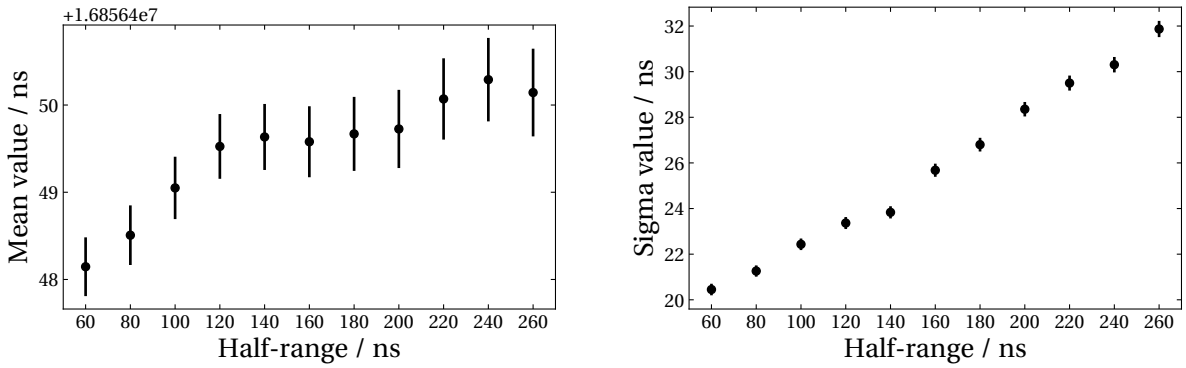

(a) **(b)**

Figure 2.10. The mean and sigma parameters of the Gaussian distribution in dependence of the half-range.

fit range. The fit range is the full width at half maximum. In figure 2.10 one can notice two plateaus. One plateau between 120 and 200 ns, the second plateau between 220 and 260 ns. The second plateau corresponds to the situation when too much of the data is included in the fitting procedure and background starts to play a significant role. The middle plateau corresponds to the situation when the most stable output fit parameters have been observed. There can be a situation when the third plateau is observed at smaller ranges, but this also has a physics explanation as not enough data has been included. The middle and small plateau has not been observed in every data set. Therefore, it can not be claimed as a universal criterion for the best choice of the fitting window. Thereby, the fitting window was chosen on a case-to-case basis. One half-range was chosen for the C_{ToF} evaluation. Let us assume as an example 80 ns. The difference in C_{ToF} between smaller half-range 60 ns and 80 ns and the difference between bigger half-range 100 ns and 80 ns were taken as systematical uncertainty coming from the variation of the data included in the fitting procedure [K$^+$20]. This is also part of the systematic uncertainty which comes from the unknown peak shape and is expressed:

$$\sigma_{C_{ToF},window} = 2C_{ToF,middle} - C_{ToF,small} - C_{ToF,big} \tag{2.8}$$

The total uncertainty is the sum of all three contributions:

$$\sigma_{C_{ToF},total} = \sqrt{\sigma^2_{C_{ToF},stat} + \sigma^2_{C_{ToF},pdf} + \sigma^2_{C_{ToF},window}} \tag{2.9}$$

2.3.3 The MR-ToF mass spectrometry data analysis

[1]

[1]This analysis has been published in [K$^+$20] by the author of the thesis as a primary author. Therefore, some pictures and text may be repeated

^{49}Sc

Ions of ^{49}Sc were stored in the MR-ToF device for 500 revolutions. Approximately 14000 ^{49}Sc ions were recorded in three data sets. The ToF spectra of $^{49}Sc^{+}$ were fitted by Gaussian, and EGH probability density functions. The ^{49}Ti ions were used as an online reference, and $^{39}K^{+}$ was chosen as an offline reference. Online and offline references were likewise fitted by Gaussian and EGH fit functions. The Gaussian fit function was used for computing the $\overline{C_{ToF}}$. The weighted relative statistical uncertainty amounted to 2.5×10^{-7}. The difference between scandium $\overline{C_{ToF}}$ values obtained from Gaussian and EGH fits was 3.45×10^{-7}. This value was added in quadrature to the total uncertainty as $\sigma_{C_{ToF},pdf}$. The optimal fitting window was chosen to be 80 ns. The obtained results for 100 ns and 60 ns fitting windows differed by 5.35×10^{-8} and 5.42×10^{-8}. Both values were added in quadrature to the total uncertainty as $\sigma_{C_{ToF},window}$. The weighted $\overline{C_{ToF}} = 0.500203363$ with the total uncertainty of 4.32×10^{-7} is listed in table 2.2

The first mass determination of ^{49}Sc was obtained from the Q-values of ^{49}Ca(β^{-})^{49}Sc [O^{+}56,M^{+}56] and ^{49}Sc(β^{-})^{49}Ti decays [R^{+}61,F^{+}69]. A few years later, this nucleus was used in several nuclear reaction experiments, giving additional Q-values [E^{+}66,W^{+}66,G^{+}68,V^{+}68]. The various number of β^{-}-decays and reaction experiments conducted with this nuclide constrained the mass excess value to -46561.3(27) keV. The new mass excess value obtained by our MR-ToF MS measurements agrees with AME2016 [H^{+}17], deviating by 3 keV. Moreover, the significance of the new direct mass excess value in the re-evaluated AME is 29 %. The new MR-ToF MS result is the first direct mass measurement of ^{49}Sc.

^{50}Sc

Ions of ^{50}Sc were stored in the MR-ToF MS for 500 revolutions. Altogether there were about 3600 ions of ^{50}Sc recorded in four data sets. Analogous analysis as for $^{49}Sc^{+}$ has been performed. The online reference was $^{50}Ti^{+}$ and the offline reference was $^{39}K^{+}$. The Gaussian fit function was used for computing $\overline{C_{ToF}}$. This led to the weighted $\overline{C_{ToF}}$=0.500633802 with the statistical uncertainty 2.34×10^{-7}. The difference due to the choice of the probability density function gave the systematic uncertainty of 4.01×10^{-7}. The systematic uncertainty from varying the fitting half-range amounted to 2.6×10^{-7} and 1.53×10^{-7} for the smaller and larger windows, respectively. The weighted result is $\overline{C_{ToF}} = 0.500633802$ and the total uncertainty is 8.4×10^{-7}.

The ^{50}Sc(β^{-})^{50}Ti decay [W^{+}69, C^{+}63] and the ^{48}Ca(He^{3},p)^{50}Sc reaction [O^{+}69] were the first experiments to provide the mass excess value of ^{50}Sc. The first direct mass measurement was performed at the TOFI spectrometer in 1998 [B^{+}98]. The uncertainty of the AME2016 [H^{+}17] value was mainly determined by the result from the ^{48}Ca(He^{3},p)^{50}Sc reaction, which

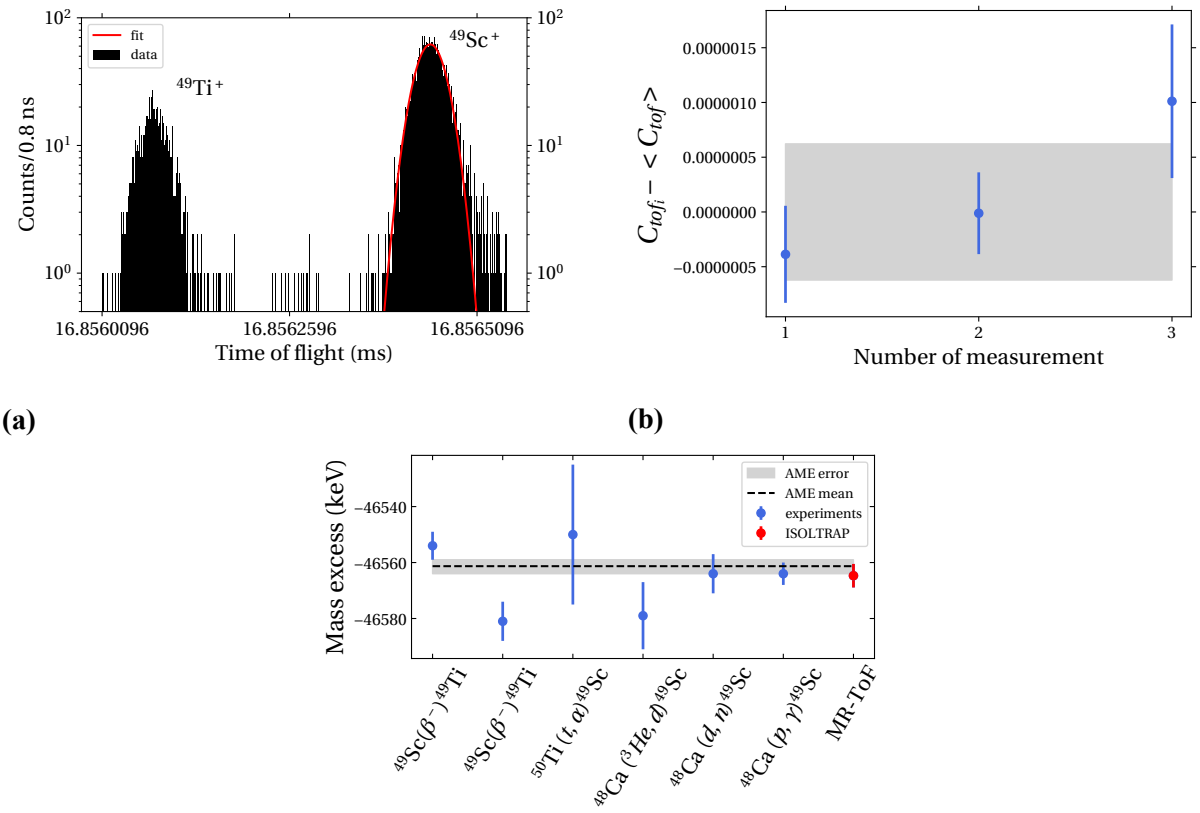

Figure 2.11. (a)- the Gaussian fit of ^{49}Sc ions. (b)-the difference between individual C_{ToF_i} and weighted $\overline{C_{ToF}}$. The total uncertainty is shown with a grey band. (c)-the experimental mass excess values of ^{49}Sc are taken from [R$^+$61, F$^+$69, E$^+$66, W$^+$66, G$^+$68, V$^+$68]. For a better visibility, the values from [O$^+$56, M$^+$56] are excluded from the plot since they have uncertainties of 50 and 100 keV.

is 15 times more precise than the uncertainty obtained by TOFI. Altogether they defined the mass excess value to -44547(15) keV. The new mass excess value measured by the MR-ToF MS technique with uncertainty of 9.1 keV agrees perfectly with the AME2016 value and, if included, contributes 73% to the re-evaluated mass excess value.

^{73}Br

The ^{73}Br ions were stored in the MR-ToF MS for 250, 500, and 1000 revolutions. There were three data sets recorded with a total number of about 4500 ions. The ^{61}Ni^{12}C molecule [SG89] contaminated the spectra (see figure 2.13-(a)). The mass resolving power $R = m/\Delta m = t/2\Delta t$ was 123000, while the minimum resolving power required to resolve these ion species is 118000 as calculated from AME2016. Thus, it was impossible to completely separate the ^{73}Br$^+$ and ^{61}Ni^{12}C$^+$ peaks. Therefore, a two-Gaussian fit function was used for computing the $\overline{C_{ToF}}$.

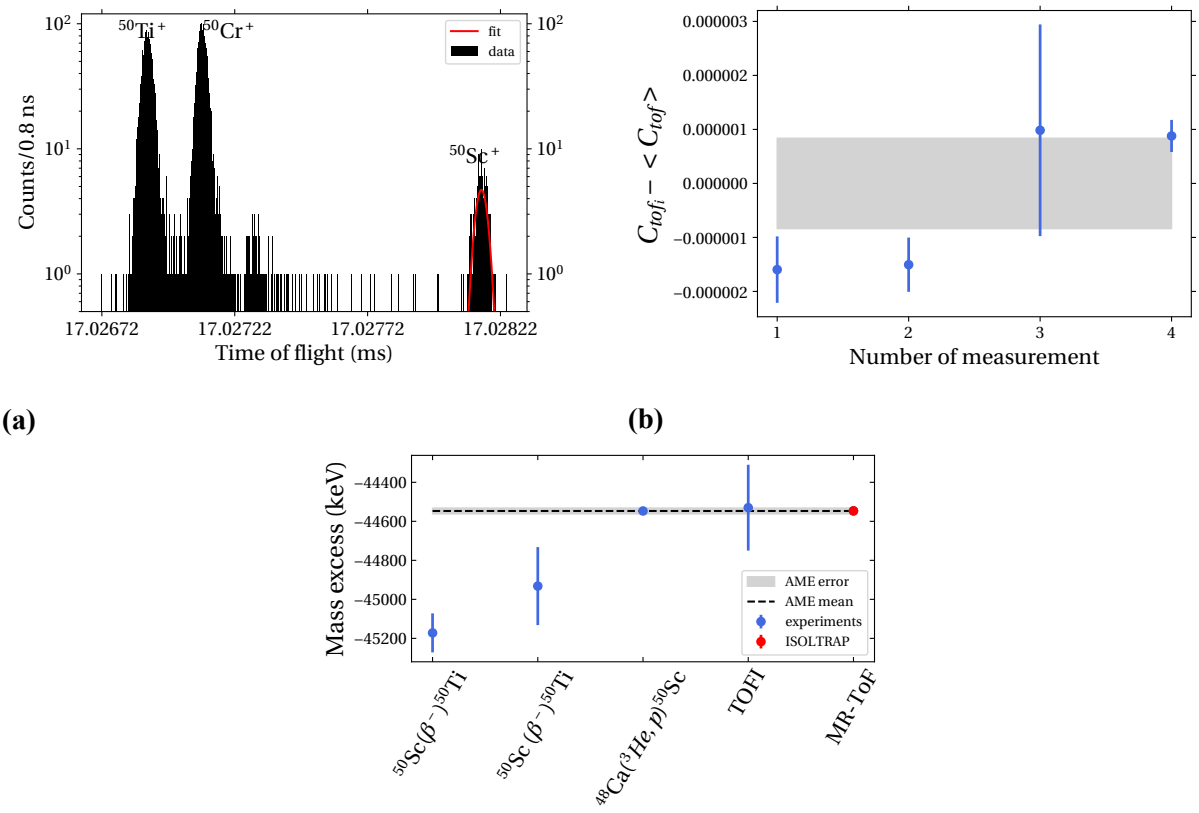

Figure 2.12. Same as figure 2.11 but for ^{50}Sc ions. The literature mass excess values of ^{50}Sc are taken from [W^{+}69, C^{+}63, O^{+}69, B^{+}98].

To employ the EGH and Gaussian fit functions, the fitting half-range had to be reduced to 80 ns. Otherwise, the peaks for bromine ions and ^{61}Ni^{12}C molecules were recognized as a single peak. The difference between the fit results with Gaussian and two-Gaussian fit functions was 2.17×10^{-8}. The corresponding difference between EGH and two-Gaussian functions was 2.63×10^{-7}. The systematic errors 1.23×10^{-6} and 1.0×10^{-6} were obtained as above by varying the fitting window. The optimum window was found to be 80 ns. The latter small window was the main source of systematic uncertainty. The final uncertainty of 1.63×10^{-6} was determined.

There are seven previous mass measurements of ^{73}Br: four beta decay studies [T^{+}01, R^{+}74, H^{+}87, M^{+}70], one ESR storage ring experiment [H^{+}01a], a ToF-ICR value measured by ISOLTRAP [H^{+}11], and two results obtained via deflection-voltage ratios of ^{73}Br and ^{72}Br in a magnetic dipole separator at the Chalk River TASCC facility [S^{+}89, S^{+}91b]. The evaluated mass excess value obtained from those experiments is -63647(7) keV and is mainly determined by the ToF-ICR result from ISOLTRAP reported in 2011. The new mass excess value obtained by MR-ToF MS agrees with the literature value within the error bars and contributes 14% to the re-evaluated mass excess.

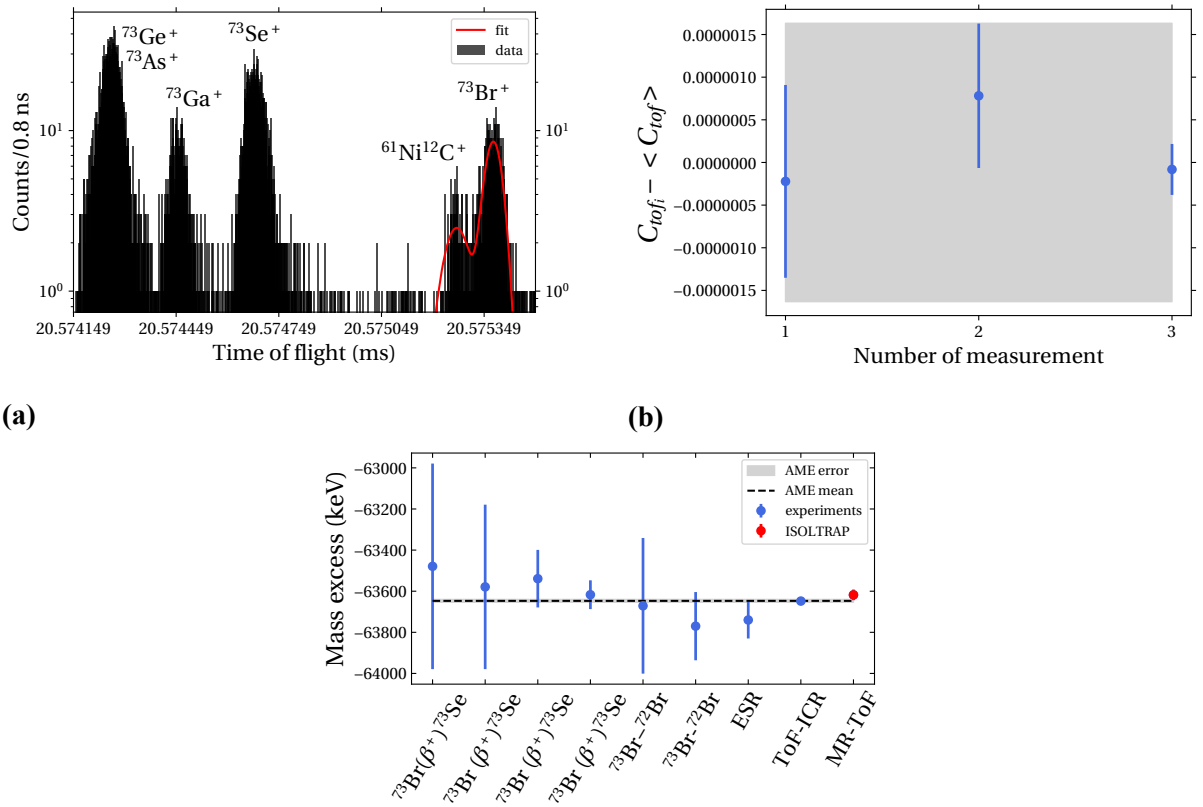

Figure 2.13. Same as figure 2.11 but for ^{73}Br ions. The literature mass excess values of ^{73}Br are taken from [T$^+$01, R$^+$74, H$^+$87, M$^+$70, H$^+$01a, H$^+$11, S$^+$89, S$^+$91b].

2.4 Alignment of the horizontal beam line

As one can see from figure 2.1, the ISOLTRAP mass spectrometer consists of two sections one horizontal and one vertical section. All devices discussed so far are part of the horizontal section.

The alignment of the vertical section was performed in 2015. It was imperative to inject the beam into the lower trap as straight as possible. The injection to the upper trap where the actual mass measurements are performed and the region between the upper trap and the top multi-channel plate detector was even more substantial [E$^+$14]. The final vertical alignment was checked with an electron beam.

The horizontal alignment procedure was done with the assistance of the trained CERN team. All elements of the horizontal beamline were taken apart and covered with target holders. The radial position was reconstructed based on the laser reflection on mirrors placed in the target holders. Based on the reconstruction (fiducialization), the adjustment of elements was made to minimize misalignments. Before the vacuum pumping, the positions of elements were checked with the theodolite—the results of two different methods supported each other. At the final step,

the beamline was pumped, and the final position of elements has been checked (red symbols in figure 2.14). The vacuum pumping moved the beamline elements, and readjustment was performed one more time. The overall misalignment was reduced to less than 1 millimeter in the horizontal section.

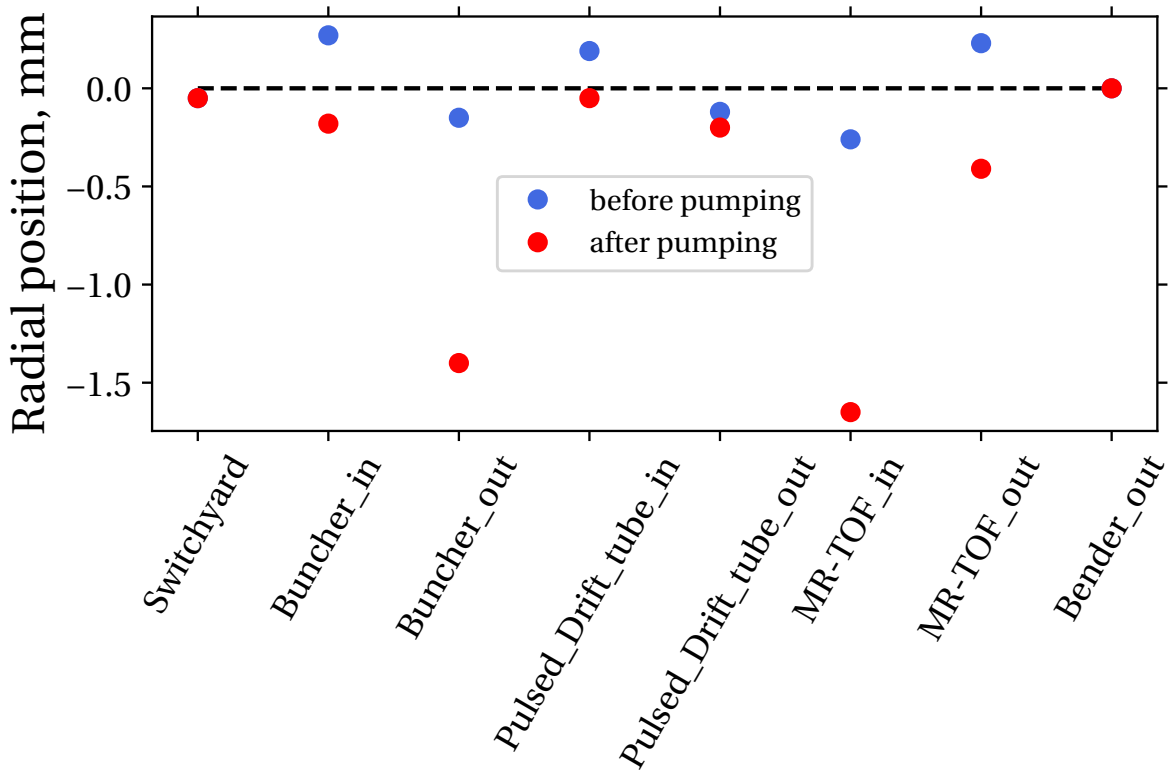

Figure 2.14. The final radial position of the horizontal beam line parts. The switchyard and the bender_out elements are taken as reference points.

2.5 ISOLTRAP Penning trap tandem

One of the most precise methods to measure the mass of an ion is based on cyclotron frequency measurements. This can be achieved by applying special manipulations of the ion motions in the electro-magnetic field of a particular configuration inside the Penning trap [Bla06]. The technique to confine ions was developed by W. Paul and H. Dehmelt [Deh90] based on the idea of F.M. Penning [Pen36]. Nowadays, it is widely used for accumulation, bunching, cooling, and charge breeding operations on the beams of ions. Moreover, the applications are broad and include fields such as mass spectrometry, antimatter studies, spectroscopy, quantum computers.

At ISOLTRAP, two types of Penning traps are used. One of the Penning traps has a cylindrical shape of electrodes, and it is used for cooling the ions and further purification from the isobaric contaminants [S^{+}91a]. The second trap has a hyperbolic shape of electrodes configu-

ration and is used for precision mass measurements. Both traps are placed in superconducting magnets. A strong magnetic field is needed to confine ions radially. The electric field is used to confine ions axially. The following paragraphs will describe the basics of the ion motions in an ideal hyperbolic Penning trap. However, all equations and general physics can be applied to cylindrical traps as well.

The quadrupolar electric potential can be written as equation 2.10 and created by the potential V_0 applied to a set of electrodes. The trap consists of three electrodes: one ring electrode, and two end cups electrodes, the hyperbolic shape of which creates a quadrupolar potential. The characteristic of the trap $2d^2 = z_0^2 + \rho_0^2/2$ is the minimum distance between the trap center and the electrodes. It depends on the distance between the end-cup electrode and the ring electrode. As it was said earlier, such a potential confines ions axially [B$^+$90a].

$$V(z,\rho) = \frac{V_0}{4d^2}(\rho^2 - 2z^2) \tag{2.10}$$

The magnetic field confines the ions in the radial direction and is aligned with the z axis of the trap. The ion's motion inside the Penning trap has been studied in great details by J.F. Berger [B$^+$91] and can be summarized by equations:

$$\ddot{x} + \omega_c\dot{y} - \frac{1}{2}\omega_z^2 x = 0 \tag{2.11}$$

$$\ddot{y} + \omega_c\dot{x} - \frac{1}{2}\omega_z^2 y = 0$$

$$\ddot{z} + \omega_z^2 z = 0$$

$\omega_z = \sqrt{\frac{qV_0}{md^2}}$: axial oscillation frequency
$\omega_c = \frac{q}{m}B$: angular oscillation frequency

The axial motion among z axis (2.11(3)) is a simple harmonic motion and it is fully decoupled from the radial motion. In turn the radial motion has a complex structure and consists of two circular motions. The solutions of equation 2.11(1-2) gives angular eigenfrequencies:

$$\omega_\pm = \frac{1}{2}(\omega_c \pm \sqrt{\omega_c^2 - 2\omega_z^2}) \tag{2.12}$$

These two motions are called modified cyclotron motion ω_+ and the magnetron motion ω_-. The magnetron motion is a drift motion in the electromagnetic field around the trap center.

The ω_c is pure cyclotron frequency and from equation 2.12 one can obtain the invariance theorem [BG86] which couples the cyclotron, magnetron, modified cyclotron and axial frequencies:

$$\omega_c = \omega_+ + \omega_- \tag{2.13}$$

$$\omega_c^2 = \omega_+^2 + \omega_-^2 + \omega_z^2$$

Because the cyclotron frequency ω_c is equal $\frac{q}{m}$B, the precise measurement of the frequency will result in a precise mass determination. A couple of techniques have been used to manipulate these frequencies and trajectories of ions inside the Penning trap. First of all, to minimize the amplitude of the axial motion, the voltage of the end cup electrode and the time of the injection are optimized. Second of all, the ring electrode has been divided into four segments. This allows the application of a bipolar or quadrupolar sinusoidal signal, which in turn allows addressing the radial motions.

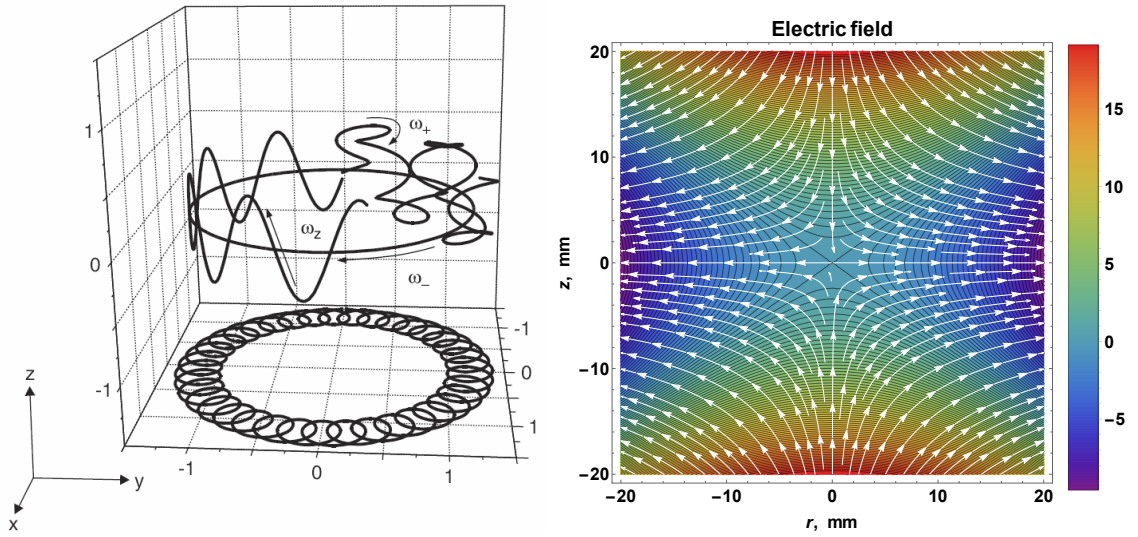

Figure 2.15. Left: the trajectory of an ion. It consists of three motions: modified cyclotron, magnetron and axial motion. Right: the electric field of a quadrupolar shape. The pictures are taken from [Din16].

In the case of the dipole field, the frequencies of the pulses are tuned to resonate with one of the radial ion motion [W$^+$05]. This allows increasing or decreasing one of the radial motions depending on the phase and amplitude of the applied pulses. One of the applications of bipolar excitation is bipolar cleaning. Because the modified cyclotron frequency is mass-dependent, one can apply a bipolar field to this motion to remove contaminant species. The other application is to prepare all ions to have the same radius of the magnetron motion. The magnetron motion is first-order mass-independent, and preparing the ions on the same magnetron radius is crucial before applying quadrupolar excitation.

If the bipolar excitation gives the excess to manipulate the ion motions individually, the quadrupolar excitation operates the sum of modified cyclotron and magnetron motion [K$^+$95b]. Applying the quadrupole excitation results in coupling these two motions. This leads to a periodic transformation of one motion into the other one. During the first part of the conversion, the radius of the magnetron motion is decreasing while the radius of the cyclotron motion is

increasing. This procedure continues until the whole conversion is achieved. At the end of the cycle, the amplitude of the cyclotron motion is equal to the initial amplitude of the magnetron motion. The period of the conversion is given by:

$$T_{conv} = 2\pi B \frac{a^2}{V_{RF}} \frac{\omega_+ - \omega_-}{\omega_c} \tag{2.14}$$

a : the radius
V_{RF} : the amplitude of the applied signal

2.5.1 Preparation penning trap

When entering the vertical section, ions are first decelerated to 100 eV by a second pulsed drift tube. Then ions are trapped in the preparation Penning trap, which has a cylindrical shape and placed in the superconducting magnet of 4.7 T strength [RH$^+$97]. The primary purpose of the device is to clean the beam from isobaric contaminants and to further cool it down by interaction with He buffer gas [S$^+$91a]. The trap consists of 20 cylindrical electrodes and filled with He gas at 10^{-6} mbar. By collisions with the buffer gas, ions lose their kinetic energy to the temperature of the buffer gas. The He gas is well known to have low chemical reactivity. This makes it perfect for cooling because ions of interest will not chemically interact with the gas. Moreover, the He atom has a full-filled atomic structure, and the ion loss will be minimal due to the charge exchange. The resulting damping force can be expressed by equation 2.15. The damping coefficient δ depends on the buffer gas properties such as temperature and pressure.

$$\overrightarrow{F} = -\delta m \overrightarrow{V} \tag{2.15}$$

$\overrightarrow{F}$: the dumping force
m : mass of an ion
δ : damping coefficient
$\overrightarrow{V}$: the velocity vector of an ion

Without a buffer, gas ions have the motions, as discussed early. However, the presence of the gas damps the axial motion by buffer gas collisions. Then the magnetron motion is excited by bipolar excitation to the radius bigger than the aperture of the ejection electrode. The quadrupolar excitation is then applied at the cyclotron frequency of the ion of interest. This leads to the conversion of the magnetron motion to the cyclotron motion. The radius of magnetron motion decreases during the conversion, while the radius of modified cyclotron motion

is reduced by the collisions with buffer gas. Consequently, the ions of interest are centered in the Penning trap at a smaller radius while the contaminant ions stay on the initial magnetron radius bigger than the aperture of the end cap electrode. During the ejection, the ions of interest are transported to the precision Penning trap, but contaminant ions hit the end cap electrode. This is the so-called mass-selective resonant buffer-gas cooling technique [S$^+$91a].

In conclusion, the preparation Penning trap can be used for purification and cooling of the beam. However, the main disadvantage of the technique is the preparation time. It takes approximately 150 ms to purify the beam, which is a significant limitation for the short-lived ions of interest. On the other hand, the MR-ToF device with the same resolving power of 10^5 performs the purification in 20 ms. Therefore, at the current stage, the MR-ToF device is preferable for the purification of the beam, and the preparation Penning trap is only used for cooling the beam.

2.5.2 Precision penning trap

After the ions are well cooled and all contaminants have been removed in the previous sections of the setup, they are injected into the precision Penning trap. At first, the ions are prepared by bipolar excitation on the smaller magnetron radius. In this way, ions experience fewer imperfections of the electric field. Second, the quadrupolar excitation is applied at $\nu_{rf} = \nu_+ + \nu_-$ with amplitude V_{rf}. If the period is correct, the magnetron motion will convert to pure cyclotron motion. The radial motion bears a certain magnetic moment $\overrightarrow{\mu} = \frac{E_r}{B}\overrightarrow{e_z}$. When the ions are ejected from the precision Penning trap, they experience a strong gradient in the magnetic field (from 6 T to some mT). This leads to a force accelerating the ions.

$$\overrightarrow{F} = -\overrightarrow{\mu}(\overrightarrow{\nabla}\overrightarrow{B}) \tag{2.16}$$

The radial kinetic energy E_r strongly depends on the modified cyclotron frequency. If the conversion from magnetron motion to modified cyclotron motion reaches maximum the ions will be accelerated most by force according to equation 2.16. In other words, resonant ions will reach the multi channel plate detector faster. The figure 2.16 is the schematic representation.

This is a so-called time of flight ion cyclotron resonance (ToF-ICR) mass measurement technique [B$^+$90a]. During the experiment, the frequency of the quadrupolar excitation is scanned around the approximate cyclotron frequency of the ion of interest ν_c. Every new ion bunch ejected out of the trap corresponds to a new frequency step. The typical ToF-ICR resonance can be recorded. The deep minimum in figure 2.17-(a) corresponds to a pure cyclotron frequency. Every point represents the mean value and the standard deviation of multiple ejected ions at the scanned excitation frequency. The shape of the resonance can be explained by the Fourier transform of the square shape of the time profile of the applied excitation. The resolving

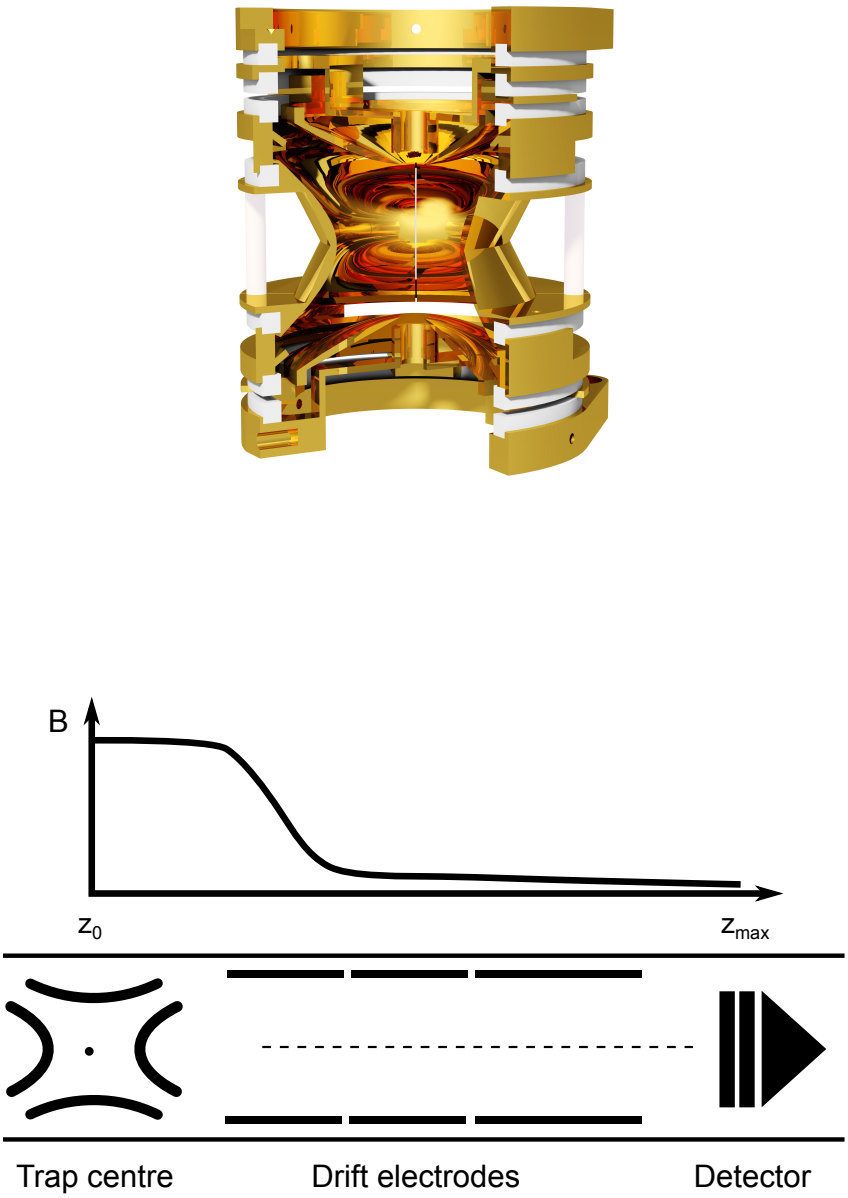

Figure 2.16. Top: the precision Penning trap [M$^+$18]. Bottom: schematic representation of the principle of the time of flight ion cyclotron resonance detection technique [Din16].

power and the precision of the technique essentially depend on the length of the quadrupolar excitation T_{RF}. The deeper and narrow the minimum, the higher is the precision. The longer the pulse the higher the resolving power. At ISOLTRAP, the length of the quadrupolar excitation T_{RF} varies between 0.2 and 1.2 seconds. This depends on the half-life of the studied ions.

$$R = \frac{\nu_c}{\delta\nu_c} = \nu_c T_{RF} \frac{\sqrt{N}}{c} \tag{2.17}$$

N : number of events

c : parameter ≈ 0.9 which slightly depends on the quality of the data

One single pulse of quadrupolar excitation couples two radial motions [GKT80]. Two pulses with some waiting time in between can be applied during the conversion. This is the so-called Ramsey type excitation. The typical resonance is shown in figure 2.17-(b). The resonance is symmetric around the cyclotron frequency. The Ramsey type [Ram90] excitation results in three times nigher precision for the same excitation time as a single pulse ToF-ICR.

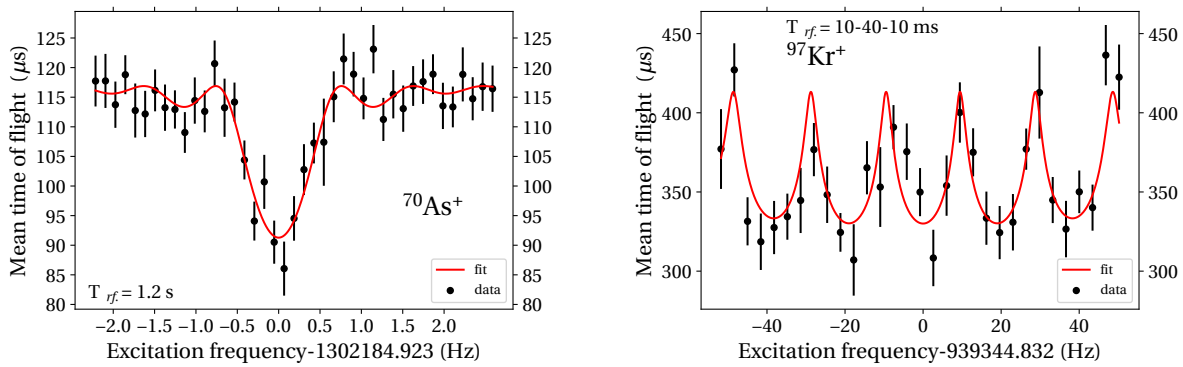

(a) **(b)**

Figure 2.17. (a)- a typical ToF-ICR resonance of ^{70}As ions using a single rf-excitation pulse of 1.2 seconds duration. (b)- a ToF-ICR resonance of ^{97}Kr ions obtained by Ramsey excitation with duration of 10-40-10 milliseconds. The line represents a fit of the theoretical lineshape to the data points [K^{+}95b]

A new technique has been developed recently. It is based on the projection of the ion motion on the position-sensitive detector. It is so-called phase image ion cyclotron resonance technique (PI-ICR) [E^{+}14]. The new approach is 25 times faster than the regular ToF-ICR and allows for 40 times higher precision. Unlike ToF-ICR, it is a no-scanning technique, and every single ion contributes to the cyclotron frequency measurement.

Applying ToF-ICR and PI-ICR techniques results in the loss of ions on the detector. These are destructive techniques, and after the mass measurement is performed, the ions of interest are entirely lost in the detector. However, there is one more technique when the beam has not been absorbed by the detector. It is a Fourier-transform ion cyclotron resonance technique (FT-ICR) [C^{+}74]. The trapped ions induce electrical signals on the electrodes of the Penning trap which follow the oscillations of the ions inside of the trap [M^{+}02]. After applying the Fourier transformation, one can reconstruct the frequencies while ions are still trapped. The only disadvantage of the technique is the noise. Therefore, such a technique requires electrodes to be cryogenically cooled and special low noise electronic devices and cables.

2.5.3 The statistical and systematical errors

In reality, the Penning trap is not an ideal system. Some imperfections lead to shifts in frequencies affecting the mass determination. Being aware of these effects, one can include them as a systematic error.

The magnetic field B has to be stable and known with high precision. Calibration of the magnetic field is performed using well-known reference masses provided from the offline ion source. The cyclotron frequency $\nu_{c,ref}$ of one of the $^{39}K^{+}$, $^{85}Rb^{+}$ or $^{133}Cs^{+}$ reference isotopes is measured before and after measuring ν_c of the ions of interest and its value at the time when the ion of interest was measured is linearly interpolated. The atomic mass is given:

$$m = \frac{\nu_{c,ref}}{\nu_c}\frac{q}{q_{ref}}(m_{ref} - q_{ref} \cdot m_e) + q \cdot m_e, \tag{2.18}$$

where m_e is the electron mass, m_{ref} is the mass of the reference ion and q, q_{ref} are the charge states of ion of interest and reference ion. Equation 2.18 assumes that the electron binding energy of the removed electrons is negligible. To account for a possible re-adjustment of the employed reference masses in future measurements, the mass of the isotope of interest is reported as a measured primary frequency ratio $r_{icr} = \nu_{c,ref}/\nu_c$.

Three factors limit the statistical uncertainty of the ToF-ICR method. All three of them rise from the beam production, contamination conditions, and decay properties of the studied cases. The first factor is the number of detected ions. A higher number of detected ions leads to a smaller statistical uncertainty. The production rate of the ion of interest, the transport efficiency of the setup, and the half-live of measured species are often the limitations of the very precise mass measurements. The second factor is the quality of the recorded spectra. The ripple of voltages, the ionization of the gas by the decay products of the studied ions, the optimization of trap excitation pulses results in a deviation of the spectrum from the theoretical line shape. As we saw, contamination leads to the shift of the cyclotron frequency and is usually included as a systematic uncertainty. The last factor is the duration of the excitation. The longer the excitation is, the more precise the measurement is. The half-live of the studied case is the limitation of the excitation time. All of these contributions can be summarized in the empirical equation 2.19. However, these factors do not strongly affect the reference measurements provided by the offline ion source. That means the statistical uncertainty of the cyclotron frequency of the ion of interest mostly dominates the final statistical uncertainty of the mass value.

$$(\frac{\delta\nu_c}{\nu_c})_{stat} = \frac{1}{\nu_c}\frac{c}{\sqrt{N}T_{RF}} \tag{2.19}$$

The first imperfection which contributes to the systematical uncertainty is the electric field [B^{+}90a]. Due to the finite size of electrodes, manufacturing tolerances, and the injection/ejection holes, the final configuration of the electric field deviates from the ideal quadrupolar shape.

Such effect is treated by storing ions with a small amplitude of the axial motion. This is achieved by properly cooling the ions. Moreover, the correction electrodes are introduced around the injection/ejection holes to compensate for the field imperfections. The imperfection of the electric field leads to so-called mass-dependent shift. The deviation from a cyclotron frequency ratio is induced through the mass difference between the reference ions and the ions of interest. The effect can be summarized by:

$$(\frac{\delta r}{r})_m = 1.6 * 10^{-10}(m - m_{ref})/u \tag{2.20}$$

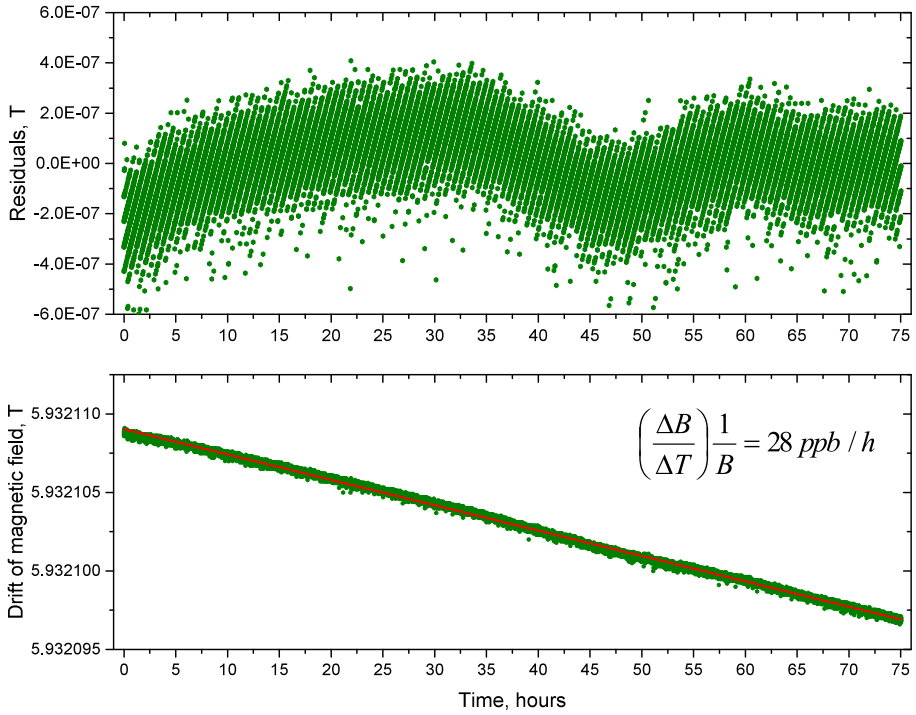

Figure 2.18. The drift of the magnetic field over 75 hours. Top picture represents residual fluctuations and bottom picture represents the long drift of the magnetic field. Pictures are taken from [Din16].

As one can notice, the measurement of the cyclotron frequency requires a very stable and homogeneous magnetic field. Currently, at ISOLTRAP, two superconducting magnets are in use, the homogeneity of which is in the order of $\Delta B/B < 10^{-7}$. The temporal magnetic stability $(\Delta B/B)/\Delta T \approx 28 ppb/h$. In figure 2.18 one can see the magnetic field drift over three days. To improve the magnetic field properties, usually, oxygen-free high-conductivity copper and ceramics are used for the trap components. For example, the trap's electrodes themselves are made out of copper. The linear drift of the magnetic field presented in figure 2.18 taken into account by linear interpolation of the magnetic field between two reference measurements. There is a nonlinear part in the drift coming from the temperature and pressure fluctuations of

the helium inside the cryostat. The nonlinear contribution has been quantified in and expressed by:

$$(\frac{\delta\nu_c}{\nu_c})_B = 6.35 * 10^{-11}\Delta T/min \tag{2.21}$$

The alignment of the magnetic field axis in the ideal case shall be parallel to the trap's axial plane. However, there is always a presence of a tilt, which leads to the shift in frequencies. This tilt was minimized during the first long shut down at CERN in 2013. The misalignment was as small as 0.08 mrad. Usually, such effects are taken as residual systematic uncertainty and show the limit of the spectrometer performance. The limit of the ISOLTRAP mass spectrometer's accuracy has been estimated in the same study. The scattering of the cyclotron ratios was still greater than one (χ^2>1). The carbon cluster source was used to estimate the residual systematic uncertainty of the ISOLTRAP setup which equals:

$$(\frac{\delta r}{r})_{res} = 8 * 10^{-9} \tag{2.22}$$

The last known systematic effect comes from the ion-ion interaction [K$^+$03]. When many ions are stored together in a small volume, the Coulomb force modifies the ion motions. If the difference in mass between the ions of interest and the contamination ions is ample, the contaminating species introduce a shift in the resonance frequency. If the resolving power is sufficient to resolve both species, a double resonance is observed. However, each frequency will be shifted towards a lower value. This shift is proportional to the number of the contaminating ions. Such effect so-called z-class analysis is treated by recording less than five ions per injection and using the MR-ToF and preparation Penning trap for the purification.

For the data analysis, the EVA software is wildly used among the trap experiments and the uncertainty of a single measurement can be expressed as:

$$\delta r_i = \sqrt{(\delta r_i)^2_{stat} + (\delta r_i)^2_B} \tag{2.23}$$

The measurement consists of a set of measurements which yield the weighted cyclotron ratio:

$$\overline{r} = \frac{\sum r_i/(\delta r_i)^2}{\sum 1/(\delta r_i)^2} \tag{2.24}$$

with an associated error:

$$\delta\overline{r} = \sqrt{\frac{1}{\sum 1/(\delta r_i)^2}} \tag{2.25}$$

The total uncertainty can be expressed:

$$\delta\overline{r}_{total} = \sqrt{(\delta\overline{r})^2 + (\delta r_m)^2 + (\delta r_{rest})^2} \tag{2.26}$$

2.5.4 ToF-ICR data analysis

[2]

^{70}As

The mass measurement of $^{70}As^{+}$ was done with the Penning trap by applying the ToF-ICR technique. A single-excitation-pulse ToF-ICR technique was used. Figure 2.16 (top) shows the measured ToF spectrum of $^{70}As^{+}$. Two ToF-ICR spectra were taken for two excitation times of 0.1 and 1.2 seconds. The reference spectrum of ^{85}Rb ions was taken every time before and after the mass measurement to account for changes in the magnetic field. The total statistical uncertainty was 1.8×10^{-8}. The correction for the difference in the mass between the ion of interest and the reference ion gave an error of 4.3×10^{-9}. To avoid ion-ion interaction shifts in the trap, the number of ions detected per ejection was fixed to be ≤ 5. Furthermore, the residual systematic uncertainty 8×10^{-9} [K^{+}03] of the ISOLTRAP mass spectrometer was added in quadrature. The frequency ratio is r_{icr}=0.8235704146 with the total uncertainty 1.8×10^{-8}. The mass of ^{70}As was known from Q-values of ^{70}As(β^{+})^{70}Ge [B^{+}63, S^{+}17] and ^{70}Se(β^{+})^{70}As decays [L^{+}75, T^{+}01]. Since ^{70}Ge is a stable nucleus with a well-known mass, the Q-value of the former decay is more precisely known. It constrains the mass excess value of ^{70}As yielding -64340(50) keV. The new mass excess value measured by ToF-ICR technique is 36 times more precise. Therefore, the re-evaluated mass excess value is now entirely determined through this ISOLTRAP measurement.

^{196}Hg

The mass measurement of $^{196}Hg^{2+}$ was done with the Penning trap by applying the ToF-ICR technique with a single-excitation-pulse. Four ToF-ICR spectra were taken. One spectrum with 0.4 seconds and the other tree with 0.6 seconds of excitation time. The reference spectrum of ^{39}K ions was taken every time before and after the mass measurement. The total uncertainty was 1.6×10^{-7}. The dominant part in this uncertainty was the correction for the mass difference between $^{196}Hg^{2+}$ and the reference $^{39}K^{+}$. This resulted in the mass-dependent systematic uncertainty of 1.4×10^{-7}. $^{196}Hg^{2+}$ being doubly charged, the ToF-ICR resonance was contaminated by charge-exchange products. As a result, the analysis was found to be dependent on the half-range chosen for the initial time-of-flight cut, leading to an additional systematic uncertainty of 2.1×10^{-7}. The residual systematic uncertainty of the ISOLTRAP mass spectrometer of 8×10^{-9} [K^{+}03] was added in quadrature as well. The number of ions detected per ejection from the trap was fixed to ≤ 5. Finally, the frequency ratio is r_{icr}=2.5147440758

[2] This analysis has been published in [K^{+}20] by the author of the thesis as a primary author. Therefore, some pictures and text may be repeated

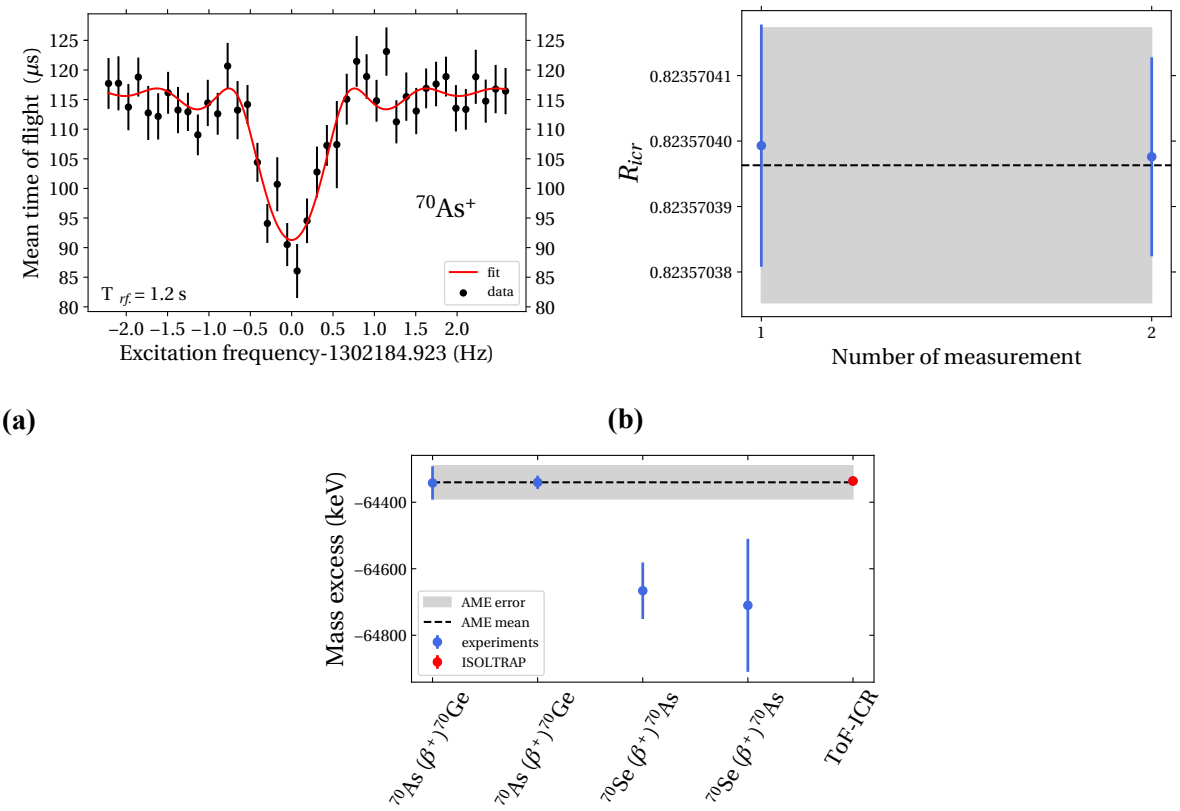

Figure 2.19. Same as Figure 2.11 but for ^{70}As ions. The literature mass excess values of ^{70}As are from [B$^+$63, S$^+$17, L$^+$75, T$^+$01].

with the total uncertainty 2.1×10^{-7}. The mass of stable ^{196}Hg was mostly determined from deflection-voltage ratios of ^{196}Hg and ^{198}Hg^{35}Cl molecule [K$^+$80]. Combined with the Q-value of the ^{196}Au(β^-)^{196}Hg decay [W$^+$62] the evaluated mass excess value is -31825.9(29) keV. The mass of ^{196}Hg was as well determined by ISOLTRAP in the past [S$^+$01]. The new mass value measured by ToF-ICR technique is in excellent agreement with all literature values and contributes 4% to the new re-evaluated value.

2.6 Summary

The technical developments of the ISOLTRAP mass spectrometer have been presented. The realignment of the horizontal beamline has been performed, overall misalignment of below 1 mm has been achieved. The performance of the buncher device was examined. The count rate and the peak shape of the bunched beam do depend on the pressure of the He buffer gas. The difference between mean values of Gaussian and EGH fit functions was checked independence on the buffer gas pressure. The new device has been built to control the bunch forming. The groundwork on the device has been made. The simulations in LTspice software and the experi-

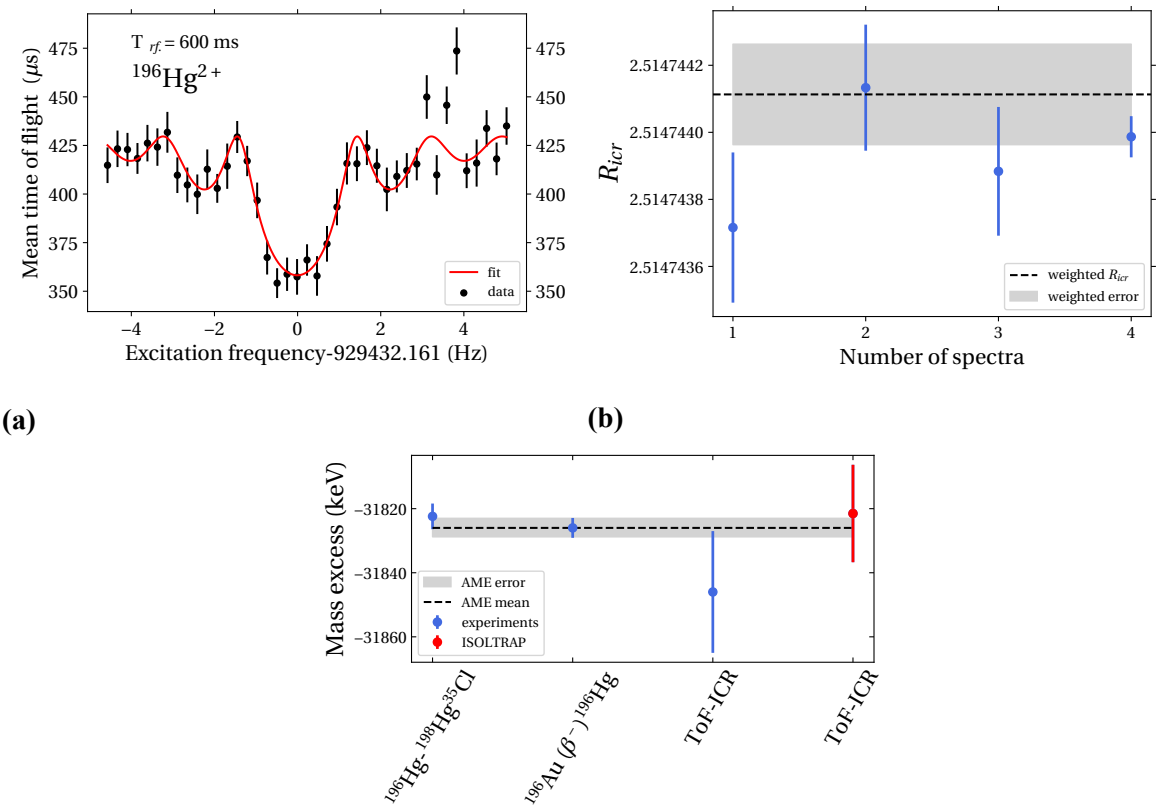

Figure 2.20. Same as Figure 2.11 but for ^{196}Hg ions. The literature mass excess values of ^{196}Hg are taken from [K^{+}80, W^{+}62, S^{+}01].

ment results with a frequency generator plus an amplifier support each other. The performance of the device as part of the ISOLTRAP mass spectrometer was checked. With this device, the online tuning of the resonance frequency has been enabled.

The masses of the short-lived ^{49,50}Sc, ^{70}As, and ^{73}Br as well as stable ^{196}Hg nuclides have been investigated by the versatile mass spectrometer ISOLTRAP. The results are summarized in figure 2.21 and table 2.2. Overall, the new experimental values agree with the literature values within the reported error bars. The uncertainties were reduced by factors 1.6 and 35 for ^{50}Sc and ^{70}As nuclei, respectively. These two isotopes have the biggest impact on the re-evaluated values in the updated AME. The agreement of the new data obtained with the MR-ToF MS confirms the reliability of this complementary mass measurement technique. Considering the achieved small uncertainties, all isotopes addressed in this work can be used as online references in future experiments at ISOLTRAP or elsewhere.

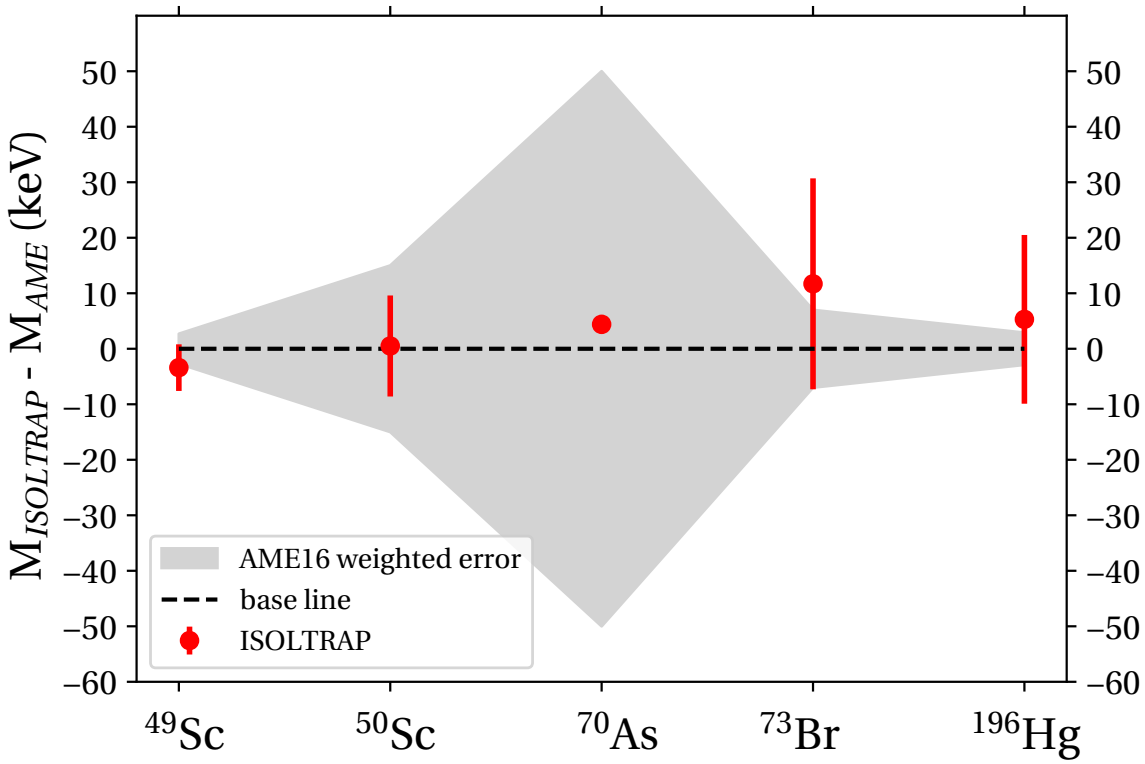

Figure 2.21. Comparison of the mass excess values determined in this work (red symbols) and the literature values taken from AME2016 [H$^+$17]. The gray shaded background represents the AME2016 uncertainties.

Table 2.2. Summary of the R_{icr} and C_{ToF} ratios as well as mass excess values of ^{49,50}Sc, ^{70}As, ^{73}Br and ^{196}Hg nuclides. Reference masses are taken from AME2016 [H$^+$17] and $T_{1/2}$ values are from NUBASE2016 [WA$^+$17]. The last column provides the significance of the ISOLTRAP results in the re-evaluated mass excess values if included into AME.

				Mass excess (keV)			
Nuclide	$T_{1/2}$	References	R_{icr}, C_{ToF}	This work	AME2016	re-evaluated	Sign.
^{49}Sc	57.2 min	^{49}Ti, ^{39}K	C_{ToF}=0.500203363(432)	-46564.7(42)	-46561.3(27)	-46562.4(23)	29 %
^{50}Sc	102.5 sec	^{50}Ti, ^{39}K	C_{ToF}=0.500633802(840)	-44546.5(91)	-44547(15)	-44546.8(78)	73 %
^{70}As	52.6 min	^{85}Rb	r_{icr}=0.823570415(18)	-64334.0(14)	-64340(50)	-64334.0 (14)	100 %
^{73}Br	3.4 min	^{73}Se, ^{85}Rb	C_{ToF}=0.49957242(163)	-63635(19)	-63647(7)	-63645.8(67)	14 %
^{196}Hg	stable	^{39}K	r_{icr}=2.514744076(209)	-31822(15)	-31825.9(29)	-31825.8(29)	4 %

Chapter 3

The shape coexistence in neutron-rich krypton isotopic chain

At first, the nuclear deformation was observed in the rare-earth region. The γ-ray emission spectra were showing the rotational-like behavior. During the γ-spectroscopy study of fission fragments of ^{252}Cf, similar behavior has been noticed at A=100. Furthermore, the energies of the first 2^+ excited state indicated the nuclear deformation. The A=100 region was identified as a new region of deformation [Joh65]. Since then, many experimental and theoretical efforts were addressed to study this region. It has been studied in great detail for the molybdenum, niobium, zirconium, strontium, yttrium, and rubidium isotopic chains. All the experimental observables indicate the shape deformation, especially in zirconium and yttrium cases. The krypton isotopic chain attracted much scientific attention over the last ten years because of the unobservable shape transition at N=60.

3.1 A=100 region

Many mass spectrometers extensively studied the A=100 region. The direct observation of irregularities of two neutron separation energies was noticed by the JYFLTRAP Penning trap system at the IGISOL facility. There was evidence of a strong correlation between the nuclear deformation and the two neutron separation energies in neutron-rich strontium, zirconium, and niobium isotopic chains [H$^+$06]. A year later, this experimental group reported even more noticeable changes in the yttrium isotopic chain and smooth irregularities in the molybdenum isotopes [H$^+$07] [R$^+$07]. The TITAN Penning trap experiment contributed to measurements of masses of rubidium and strontium isotopes and also observed irregularities in two neutron separation energies [K$^+$16] [S$^+$12]. The endpoint of the mass measurements in rubidium and strontium isotopic chains was done by the ISOLTRAP mass spectrometer, where confirmation of the deformation was shown until the neutron number N=65 [DR$^+$17]. However, one ques-

tion remained open. Where is the lower Z-bound of the deformation region? Is it the krypton isotopic chain? And if so, at which neutron number? In 2010 the mass measurement from the ISOLTRAP mass spectrometer got the mass of ^{97}Kr, and no irregularities in two neutron separation energy were found [N^{+}10]. It was established as a critical point boundary [A^{+}12]. Authors conclude in [M^{+}13a] that the nuclear deformation may start at ^{98}Kr.

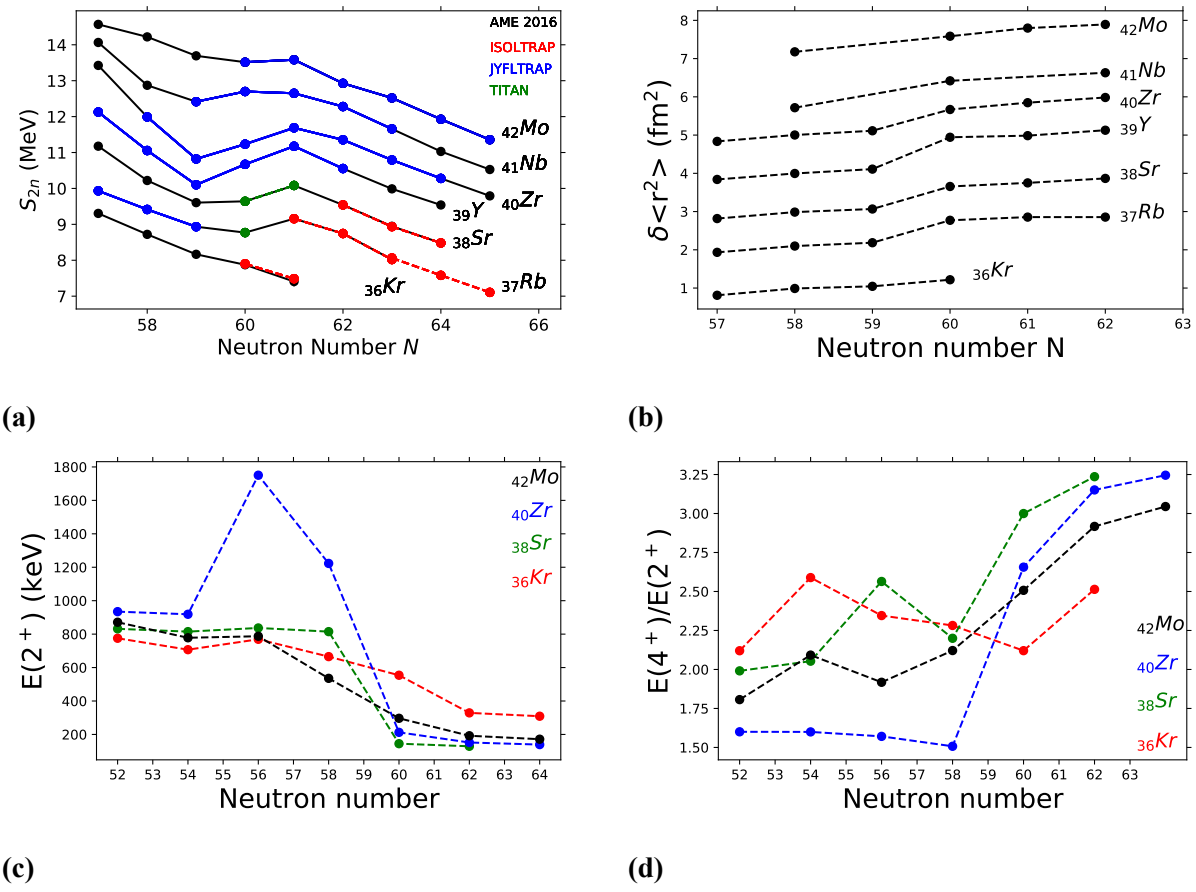

Figure 3.1. (a)- the two neutron separation energy trend [H^{+}17]. (b)- the evolution of the charge radii in A=100 region [A^{+}13]. (c)- the evolution of the energy of the first 2+ excited state [Lab]. (d)- the trends of the ratio between 4+ and 2+ excited states.

The change in the shape of a nucleus is experimentally observed through the evolution of the mean-square charge radii [A^{+}13], extracted from the isotope-shift measurements and hyperfine-structure measurements [K^{+}95a, T^{+}81, B^{+}90b, L^{+}91, C^{+}07, C^{+}02]. The mean-square charge radii show a rising trend at N=60 for zirconium, yttrium, strontium, and rubidium isotopes, which is a clear indication of the deformation [C^{+}97, F^{+}03, C^{+}16]. Unlikely, the charge radii for ^{97}Kr and ^{98}Kr are not yet available.

Another experimental evidence is the reduced energies of the first 2+ excited states, which have been experimentally observed for strontium, zirconium, and molybdenum isotopes at N=60. There were contradictions between mass measurements [M^{+}13a] and γ-ray spectroscopy

measurements [M$^+$09] on the ^{96}Kr isotope. Authors of [M$^+$09] measured the energy of 2+ state and concluded the deformation of this isotope. However, newer results from γ-ray spectroscopy and Coulomb excitation experiments do not observe the energy drop of 2+ excited state at ^{96}Kr isotopes [D$^+$17, A$^+$12]. The γ-ray spectroscopy research [F$^+$17b] up to ^{100}Kr isotope spotlights the drop at ^{98}Kr. Moreover, the ratio between 4+ and 2+ excited states indicates that the deformation starts at N=62 in the krypton isotopic chain.

3.2 Data analysis

Two different campaigns have taken place at CERN in 2015 and 2017. Radioactive ions were produced and delivered by the ISOLDE facility. In both cases, krypton isotopes were produced by bombarding the UC_x target with 1.4 GeV proton pulses and an average intensity of 1.3 μA. Nuclides diffused and effused out of the target and were ionized by a cold plasma ion source in VADIS mode. The ToF-ICR mass spectrometry was performed on the ^{97}Kr isotope in 2015. The MR-ToF mass spectrometry was performed on $^{96-98}$Kr isotopes in 2017.

3.2.1 ToF-ICR

^{97}Kr

Three spectra of ^{97}Kr isotope were taken in 2015. Two spectra with 50 ms excitation time and one TOF-ICR spectrum of Ramsey scheme with excitation of 10-40-10 ms. The Ramsey resonance is shown in figure 2.17-(b) and a single pulse ToF-ICR resonance is shown in figure 3.2-(a). The ^{39}K ions were chosen to make a linear extrapolation of the drift of the magnetic field. The total statistical uncertainty is equal to 7.2×10^{-7}. The correction for the difference in mass between ^{39}K and ^{97}Kr ions is equal to 5×10^{-8}. The last systematic uncertainty is the residual uncertainty of the ISOLTRAP mass spectrometer which is equal to 8×10^{-9}. As one can see from figure 3.2-(b) the R_{icr} ratio obtained by Ramsey type of excitation (third point on the figure) agrees well with the single pulse ToF-ICR scheme but is two times more precise. As a check of Coulomb interactions inside the Penning trap, the histogram in figure 3.2-(c) was plotted. As one can see, most ejections have 0 number of ions, and only a few have more than three ions per ejection. That means that ”z”-class analysis is unneeded because mostly it was one ion per ejection. The new mass excess value (figure 3.4-(d)) agrees well with previous mass measurement which was done in 2010 in the preparation Penning trap applying different technique [N$^+$10]. Moreover, it agrees well with MR-ToF mass spectrometry value provided later in work. Final mass excess value is listed in table 3.1.

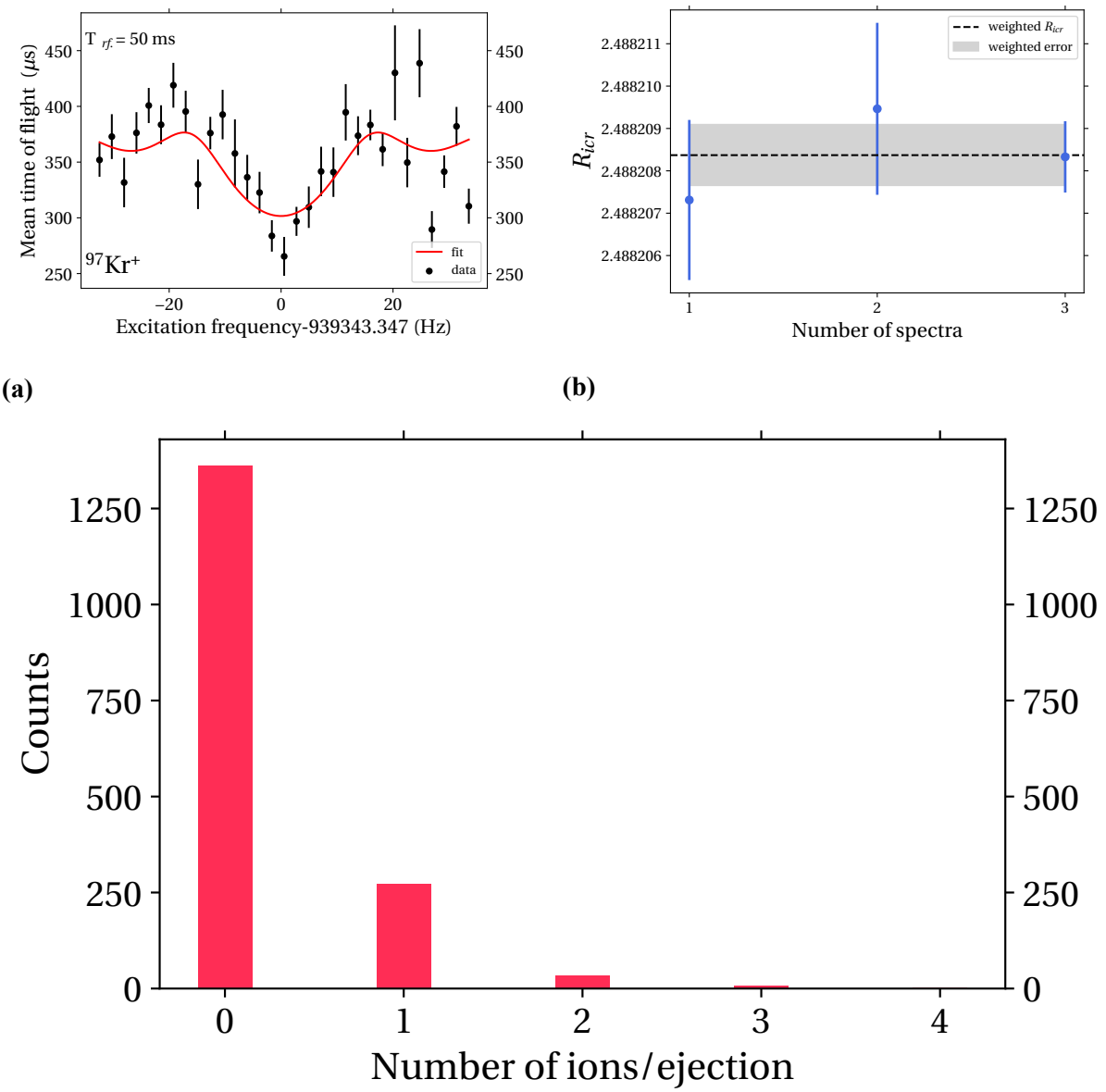

Figure 3.2. (a)- the single pulse ToF-ICR resonance of ^{97}Kr ions. (b)- the spread of the R_{icr} ratio of ^{97}Kr ions. (c)- the dependence of counts on number of ions per ejection.

3.2.2 MR-ToF

^{96}Kr

The MR-ToF data was recorded in 2017. For the mass determination of ^{96}Kr ions, 150 files were recorded with 201 ions of interest in total. Files were summed and grouped into 12 data sets. The number of revolutions was the same in all spectra and equaled 1000 revolutions. The ^{96}Kr ions were measured as double-charged ions. As an online reference, ^{48}SO molecule was chosen, and ^{85}Rb as an offline reference. It was fitted by Gaussian and EGH fit functions based on the

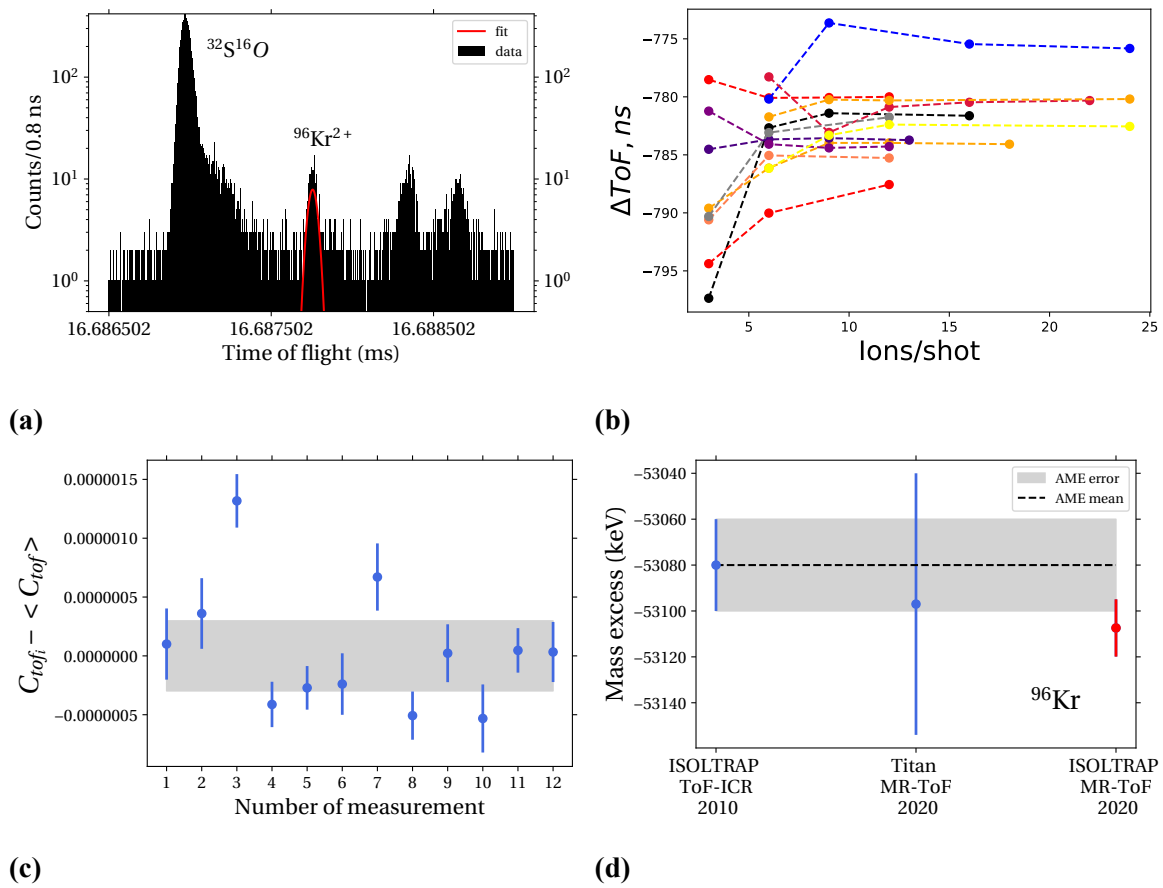

Figure 3.3. (a)- the time of flight spectrum of ^{96}Kr ions. (b)- the time of flight difference between two peaks vs the number of ions per ejection. Every color represents different set of files. (c)- the difference between the individual C_{tof} ratios and weighted $\overline{C_{ToF}}$ ratio of ^{96}Kr ions. (d)- the comparison between experimental and literature values from AME16 [H$^+$17]

maximum likelihood estimation and yielded the systematic uncertainty $\sigma_{C_{ToF},pdf}$=2.8 $\times$ 10^{-7} coming from an unknown peak shape. The Gaussian fit function was used for computing the $\overline{C_{ToF}}$=0.499858112. The weighted statistical uncertainty amounted to 6.7 $\times$ 10^{-8}. The range study was performed. The optimum range was 70 ns for ^{96}Kr ions and reference ions. The $\sigma_{C_{ToF},window}$ systematic error was not considered in this analysis. The other study on the MR-ToF systematics was performed instead. The idea was to see how the time of flight difference between two peaks depends on the number of ions present in the device. Figure 3.3- (b) represents this dependency. As one can see the difference between the two peaks is getting smaller with more ions in the shot. The systematic error coming from the number of ions present in the device can be expressed:

$$\sigma_{C_{ToF},z-class} = C_{ToF}(min + next, ions/shot) - C_{ToF}(max, ions/shot) \quad (3.1)$$

$C_{ToF}(min + next, ions/shot)$: calculated for the pre-minimum number of ions/shot.

It yielded 6.2×10^{-8} of the systematic uncertainty. The final C_{ToF} values which were used to compute $\overline{C_{ToF}}$ were taken at maximum ions per shot. The total uncertainty 3.2×10^{-7} can be expressed as square root of the sum of contributions:

$$\sigma_{C_{ToF},total} = \sqrt{\sigma^2_{\overline{C_{ToF}},stat} + \sigma^2_{\overline{C_{ToF}},pdf} + \sigma^2_{\overline{C_{ToF}},z-class}} \tag{3.2}$$

The new mass value agrees well (see figure 3.3- (d)) with ToF-ICR measurement from ISOLTRAP and with MR-ToF mass measurement from TITAN experiment based at the TRI-UMF facility [M$^+$20]. The final results are listed in table 3.1.

^{97}Kr

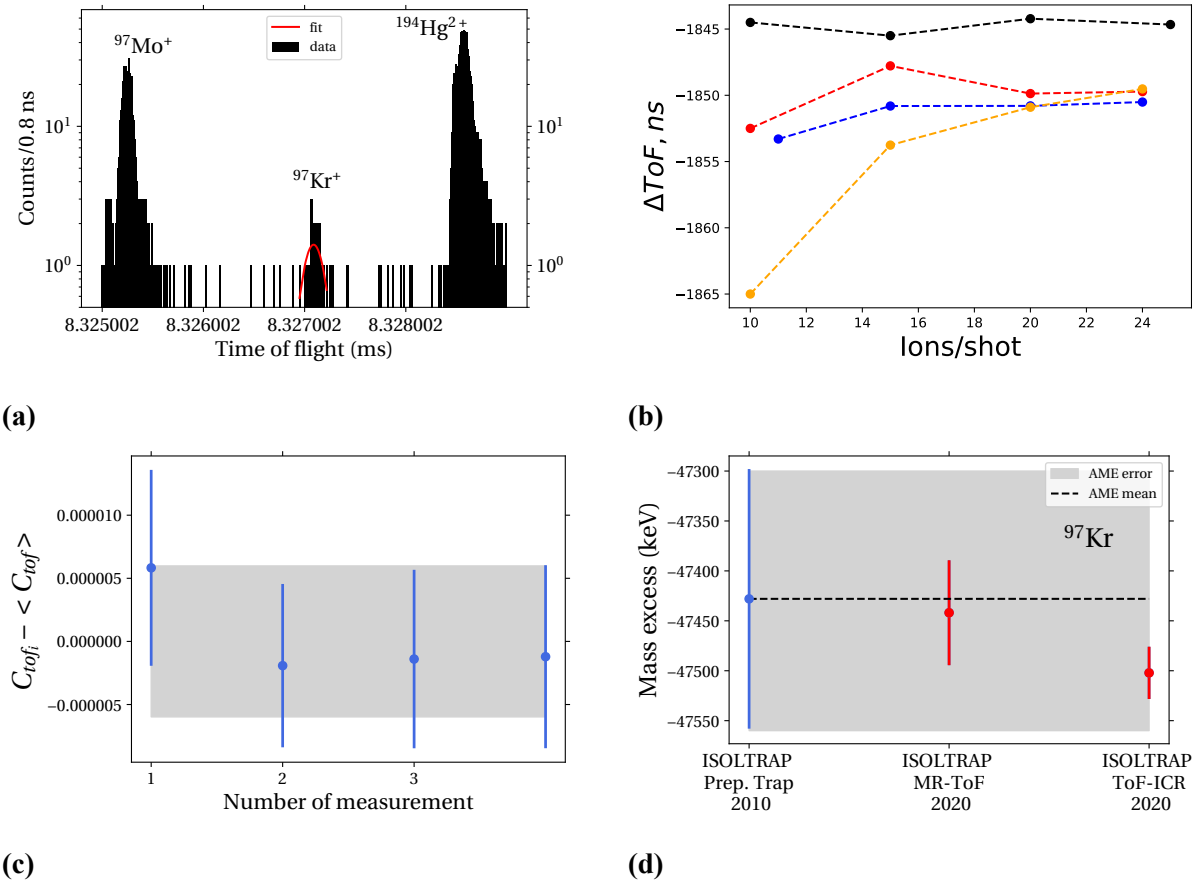

Figure 3.4. (a)- the time of flight spectrum of ^{97}Kr ions. (b)- the time of flight difference between two peaks vs the number of ions per ejection. Every color represents different set of files. (c)- the difference between the individual C_{tof} ratios and weighted $\overline{C_{ToF}}$ ratio of ^{97}Kr ions. (d)- the comparison between experimental and literature values from AME16 [H$^+$17]

A limited statistic is available for ^{97}Kr isotope. Only four files were recorded with 19 ions in total at 350 revolutions. The spectra were fitted by Gaussian and EGH fit functions. ^{97}Mo was taken as an online reference and ^{85}Rb as an offline. It was fitted by Gaussian, and EGH fit

functions based on the maximum likelihood estimation and yielded the systematic uncertainty $\sigma_{C_{ToF},pdf}$=1.8×10^{-6} coming from an unknown peak shape. The Gaussian fit function was used for computing the $\overline{C_{ToF}}$=0.503474279. The weighted statistical uncertainty amounted to 3.6×10^{-6}. The range study was performed. The optimum is 70 ns for references and 150 ns for the ion of interest. However, it was not included in the systematic uncertainty. The same analysis was performed as for the ^{96}Kr isotope. The trend of the differences shows the same behavior as for ^{96}Kr ions. It resulted in the 3.9×10^{-6} of systematical uncertainty coming from the "z-class" analysis. The total uncertainty is equal to 5.6×10^{-6}. The comparison of results between different techniques is shown in figure 3.4-(d). As one can see the result is in good agreement with previous mass measurement from 2010 and also with a new mass excess value obtained by ToF-ICR technique. The final results are listed in table 3.1.

^{98}Kr

The mass of ^{98}Kr isotopes was not previously measured. It is an exotic isotope with a tiny production. There are 182 files with 37 ions of interest in total. To make sure that observed ions are krypton ions one spectrum was taken without any protons on the target. That led to the disappearance of krypton ions in the ToF spectrum. The spectra were grouped in 9 files and were fitted by Gaussian and EGH fit functions with maximum likelihood estimation. The systematic uncertainty is $\sigma_{C_{ToF},pdf}$=3.5×10^{-6} and comes from unknown peak shape. Since the count rate of ^{98}Kr was low, it had no sense to fit the spectra at small ranges and 150 ns was chosen for all files. ^{98}Mo was chosen as an online reference. The optimal range for Gaussian fit of ^{98}Mo was chosen 60 ns for all spectra. ^{85}Rb was chosen as an offline reference with 60 ns range. The Gaussian fit function was used for computing the $\overline{C_{ToF}}$=0.503501959. The weighted statistical uncertainty amounted to 3.9×10^{-6}. The actual MR-ToF spectrum is shown in figure 3.5-(a). To see how much of the data is included by equation 3.1 the histogram 3.5-(c) was built. It shows the difference between individual differences and the difference at maximum ions per injection. The mean value of the distribution is equal to 0.851 ns. The exponential fit is plotted to show the trend and red counts are those which have been excluded. As one can see, most of the deviations are included by the applied equation 3.1. Overall this analysis resulted in the 6.0×10^{-6} of systematical uncertainty. The total uncertainty is equal to 7.98×10^{-6}. The final results are listed in table 3.1.

The results of the data analysis can be summarised in figure 3.6. The observed trend of two neutron separation energy does not indicate a clear shape transition in the krypton chain up to N=62.

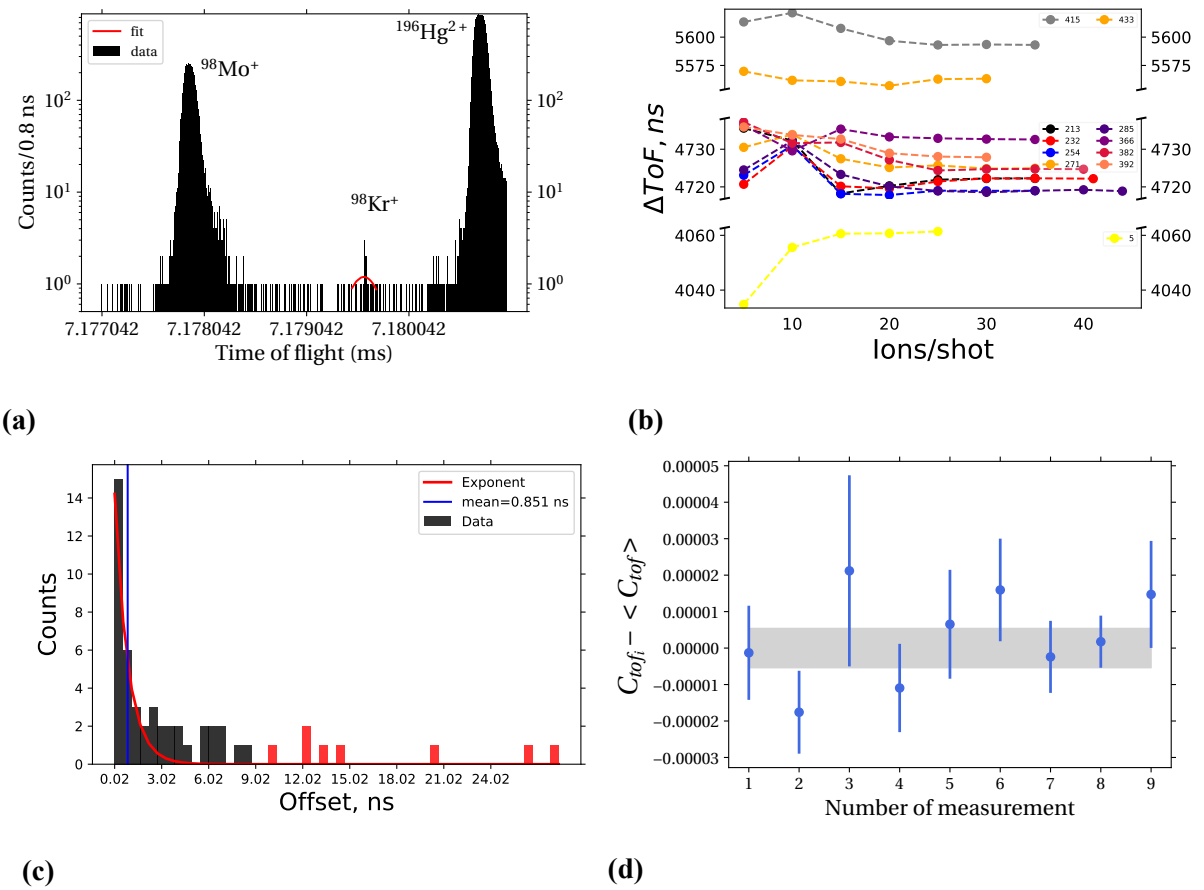

Figure 3.5. (a)- the time of flight spectrum of ^{98}Kr ions. (b)- the time of flight difference between two peaks vs the number of ions per ejection. Every color represents different set of files. (c)- the histogram of the differences between ΔToF_i and $\Delta ToF_{max,ions/shot}$ for details see text. (d)- the difference between of the individual C_{tof} ratios and weighted $\overline{C_{ToF}}$ ratio of ^{98}Kr ions.

3.3 Theoretical approaches

The main aim of theoretical nuclear models is to describe the experimentally observed properties of nuclei. The nucleus consists of protons and neutrons, which also have compound nature (they consist of quarks). All together, they form a complex system, and understanding all interactions within the system is a challenging task. Modern theoretical models can describe some nuclear properties. However, there is no such model that can describe everything at once.

If one wants to find the mass of the nuclei, the naive approach would be to sum up the mass of all protons and neutrons constituting the nuclei. With developments of mass spectrometers [BL13], scientists quickly realized that this is not the case and the mass of a nucleus is less than the sum of the mass of its constituents. This statement has been expressed by equation 1.3. This mass difference was identified as the energy that bounded the nucleus and was named binding energy.

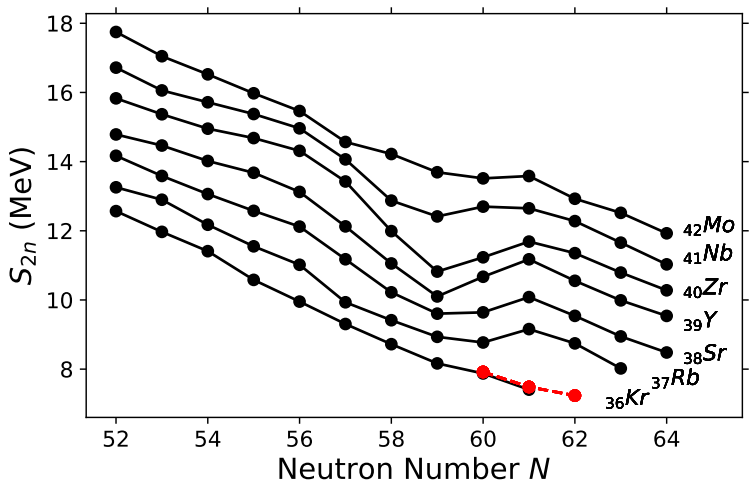

Figure 3.6. The evolution of the two neutron separation energy in molybdenum, niobium, zirconium, strontium, yttrium, rubidium and krypton isotopic chains. The literature values taken from AME2016 [H+17]. The new experimental two neutron separation energies obtained by ISOLTRAP mass spectrometer are colored in red.

Figure 3.7 summarizes the average binding energy per nucleon as a function of nucleon number. First, the rapid increase can be spotlighted in the light nuclei region until sodium. Each additional nucleon is attracted by other nearby nucleons, and thus more tightly bound to the whole system by the short-handed nuclear force. Second, the steady decrease of the binding energy after iron can be explained as nuclei have become big enough that the nuclear force is almost equal to the electromagnetic forces between protons.

3.3.1 Liquid drop model

The first attempts to describe the nucleus and observed trends of the binding energy were done by Gamow and further developed by Bohr and Wheeler [GR30]. They assumed that the nucleus is a drop of incompressible fluid of very high density, held together by the nuclear force. In 1935 German physicist Carl Friedrich von Weizsäcker proposed his famous formula [Wei35] based on liquid drop theory and empirical measurements:

$$B_{nuc} = a_{vol}A - a_{surf}A^{2/3} - a_c\frac{Z(Z-1)}{A^{1/3}} - a_I\frac{(N-Z)^2}{A} + \delta(N,Z) \tag{3.3}$$

The first term is the volume term, and it is directly proportional to the sum of nucleon masses. This term represents short-handed nuclear interaction meaning that nucleon can interact only with its neighbors. The second term is the surface term. The term can be associated with the surface tension of the liquid. This is a correction for the volume term because nucleons on the surface have fewer neighbors. The third term represents the Coulomb force. The fourth term

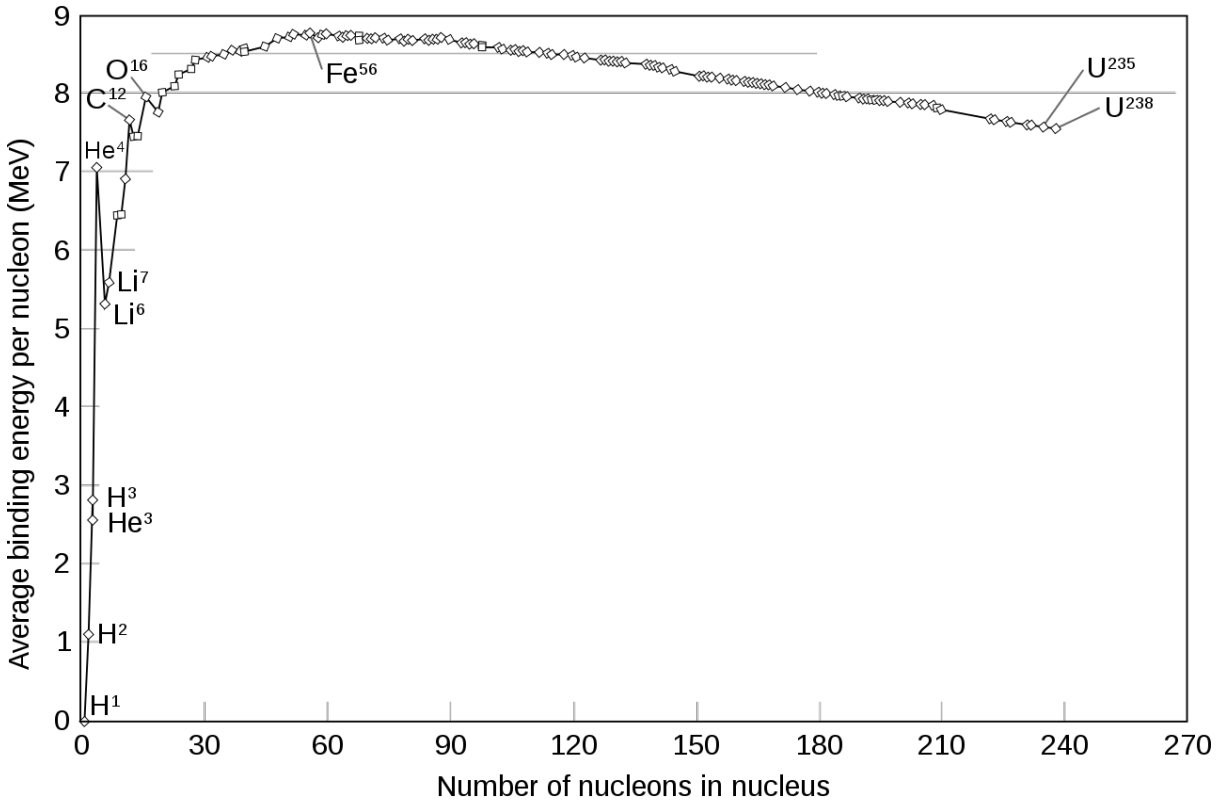

Figure 3.7. The dependence of the average binding energy per nucleon as a function of the number of nucleons in the nucleus.

considers the asymmetry energy coming from the Pauli principle. The last term considers the odd-even staggering effect through the function δ which depends on the number of protons Z and the number of neutrons N and their tendency to form pairs.

The liquid drop model is a macroscopic approach to describe the nucleus. The advantage of the liquid drop model is that it describes the binding energy trend shown in figure 3.7. Also, it provides a good description of the fission mechanism and nuclear reactions at low energies. However, it falls short of describing peaks at He^4, C^{12}, O^{16}б so-called magic numbers where the gain of the binding energy appears and the nuclear deformation [M$^+$95].

In order to obtain the a_{vol}, a_{surf}, a_c and a_I constants one have to fit the model to the entire nuclear chart. The latest FRDM2012 model [M$^+$16b] which also includes some microscopic contributions shows rather well agreement with the experimental data collected in AME2003. The root-mean-square(RMS) deviation is the quantity that shows the ability of the mass model to describe the experimental values. For the FRDM2012 the RMS is equal to 560 keV. This calculation is based on 2169 nuclei of the nuclear database. Figure 3.8 shows the trends of two neutron separation energy in A=100 region based on the experimental values and the values calculated by this model. The model indicates some nuclear structure effects at N=56 and N=60. The experimental trends (black dots) represent the N=56 sub-shell closure and the deformation at N=60. The model, indeed, is not sensitive to separate these two effects well. Especially

in strontium and zirconium chains model mixes these two effects which lead to the average increase of the two neutron separation energy between N=56 and N=60.

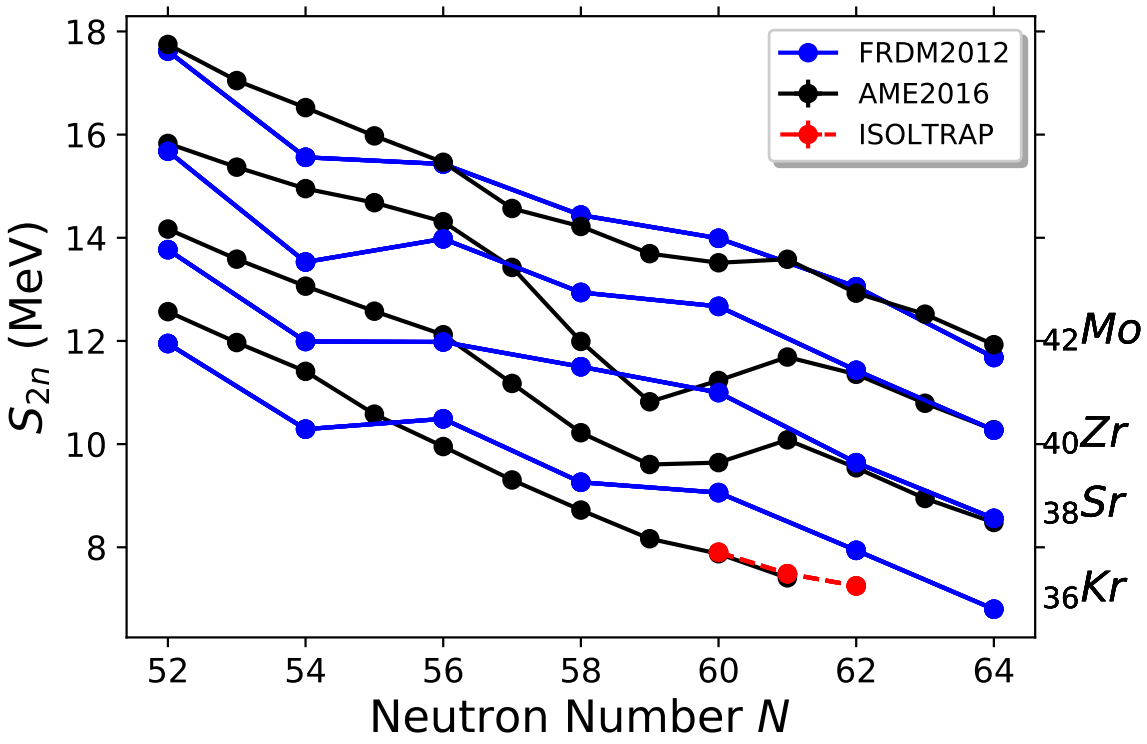

Figure 3.8. The evolution of the two neutron separation energy in neutron-rich krypton, strontium, zirconium and molybdenum isotopic chains. The black two neutron separation energy trends are taken from AME2016 [H$^+$17]. Red two neutron separation energies calculated from the new $^{96-98}$Kr mass measurements. The blue values are taken from FRDM2012 [M$^+$16b]. For the visibility error bars are omitted.

Overall the predictive power of the modern FRDM2012 model is not sufficient to conclude the effects discussed in this work.

3.3.2 Shell model

The observed periodicity in the nuclear binding energy was quickly rethought with the shell structure of an atom. Mayer and Haxel proposed the shell structure of a nucleus in the fifties. In this model, the neutrons and protons fulfill independent shells, and the shell closure corresponds to the fulfilled states [May48].

In nuclear structure calculations, one has to solve the Schrodinger equation:

$$\hat{H}|\psi>=E|\psi> \tag{3.4}$$

with Hamiltonian defined as:

$$\hat{H} = \hat{T} + \hat{V} = \sum_{i=1}^{A} \frac{\boldsymbol{p_i^2}}{2m_i} + \sum_{i<j}^{A} V_{ij} \tag{3.5}$$

The first term is kinetic energy, and the second term is potential energy considering only two-body interactions. For simplicity, the higher orders of interaction have been omitted. It is challenging to find the exact solution when calculating the interactions in the Hamiltonian by summing over all states. It is the famous many-body problem [Rin00]. It has been solved strictly only for the lightest nuclei [P$^+$01]. In most models only two-body interactions are considered. In the shell model the system of two-body interacting bodies is replaced by a system of independent particles interacting in a well-chosen average potential. Therefore, the potential term in the Hamiltonian can be written as:

$$\hat{V} = \hat{V}_0 + \hat{V}_{rest} \tag{3.6}$$

In the first independent particle model the rest interaction was neglected. The shell model treated the nucleus as a system of independent particles orbiting in the spherical potential. The model was built on a simple harmonic oscillator (S.H.O) [May48] for neutrons and protons separately:

$$V_0(\vec{r}) = \frac{1}{2}\hbar\omega^2\vec{r}^2 \tag{3.7}$$

It reproduces well the energy levels up to magic number 20. The S.H.O. potential has two weak points: the nucleons are infinitely bound at a large radius, and each level is actually a degenerate multiplet, unresolved using the oscillator's quantum number. The second attempt was a slight modification of the S.H.O potential to a Woods-Saxon [C$^+$87] shape:

$$V_0(\vec{r}) = \frac{V_0}{1 + \exp\frac{\vec{r}-R}{a}} \tag{3.8}$$

V_0 : the depth of the potential
$\vec{r}$: the distance from the center of the potential
$R = 1.2A^{1/3}$: the radius
a : is a measure of how rapidly the potential falls to zero

Even this modification could not replicate all the magic numbers. So the last modification takes into account the spin-orbit interaction. After applying the spin-orbit term into the single-particle Hamiltonian the success of the shell model was confirmed. The potential can be described by equation 3.9. For the visualization all the potentials and corresponding shell structure are summarized in figure 3.9.

$$V_0(\vec{l},\vec{s}) = -V_{ls}\frac{dV_0(\vec{r})}{d\vec{r}}\vec{l}\vec{s} \tag{3.9}$$

V_{ls} : the strength constant
$\vec{l}$: the orbital angular momentum
$\vec{s}$: the intrinsic spin of the nucleon

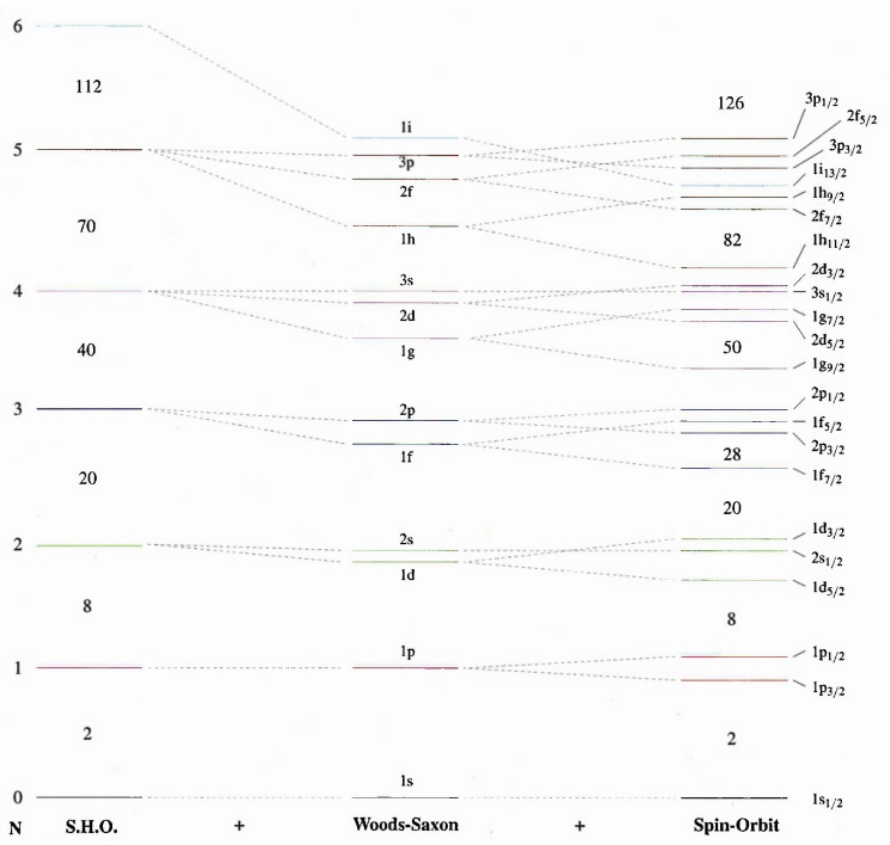

Figure 3.9. The shell ordering with different potentials [MJ55]

.

For simplifying the calculations the restriction on the number of active nucleons outside of a certain core is often applied in shell model calculations. In most cases the inert core corresponds to a doubly magic nucleus and the orbits are forced to be full. At the same time, the valence nucleons are those which occupy valence orbits. The deformation at A=100 firstly has been studied via shell model calculations on zirconium isotopes. An inert core of ^{88}Sr was assumed for the shell model calculation of even $^{96-100}$Zr isotopes. Authors determined the deformation as the results of the proton-neutron correlation between $1g_{9/2}$ orbital for protons and $1g_{7/2}$, $3s_{1/2}$ and $2d_{3/2}$ orbitals for neutron [FP79]. The other method to keep the sizes of the Hamiltonian matrices manageable is to use Monte Carlo mathematical method. The large-scale Monte Carlo

Shell Model (MCSM) calculations on even-even Zr isotopes have been studied [T$^+$16]. Both methods reproduced the experimentally observed trend of the first 0^+ and 2^+ excited states of even zirconium isotopes. Finally, there are other methods studying the region - the projected shell model, discussed in detail in [V$^+$08].

The experimentally measured masses of neutron rich $^{96-98}$Kr isotopes are a clear call to perform shell model calculations. So far, only calculations for zirconium and strontium isotopes are well presented in the literature. A quantum phase transition has been shown to occur in zirconium and strontium neutron-rich isotopes.

3.3.3 Self-consistent mean field model

The nuclear shell model assumes that the residual interactions are small compared to the mean field. And this is true for the reproduction of the magic periodicity of the binding energy. However, the energy spacing between subshells can have values close to the residual interaction energy scale. Although residual interactions make a relatively small contribution to the total binding energy of the nucleus, they largely determine the bond of valence nucleons and the spin, magnetic, and quadrupole moments of nuclei. However, how to divide the single-particle information and two-body interactions in the total sum?

A special method was developed by Hartree and Fock (HF) [Rin00] to replace the exact Hamiltonian 3.5 by its two-body approximation. In this method the potential for nucleons is computed from the nucleonic wave functions. In the following only the main results of the formalism will be highlighted [Rin00].

The methods starts from the general variational principle. It has been shown that exact Schrodinger equation 3.4 is equivalent to the variational equation:

$$\delta E[\psi] = 0 \tag{3.10}$$

$$E[\psi] = \frac{<\psi|\hat{H}|\psi>}{<\psi|\psi>}$$

The wave functions $|\psi>$ are restricted to be trial and simple. From this variational method we do not know the exact wave function ψ, we can find only an approximation $|\phi>$. This approximation corresponds to the variationaly optimized single-particle operator with Hamiltonian of the spherical harmonic oscillator:

$$\hat{H} = \sum_{i,j} t_{ij} a_i^\dagger a_j + \frac{1}{4} \sum_{i,j,k,l} \overline{\nu}_{ij,kl} a_i^\dagger a_j^\dagger a_l a_k \tag{3.11}$$

$$t_{i,j} =< i|\hat{t}|j >$$

$$\overline{\nu}_{ij,kl} =< ij|\overline{\nu}|kl > - < ij|\overline{\nu}|lk >$$

The first and the second term are the matrix elements of the kinetic-energy and two-body potential between states. $a_i^\dagger$ and a_i represents the creation and annihilation operators for the state i. The latter includes the Pauli principle through the anti-commutation relations. The Slater determinant $|\phi >$ can be expressed as product of creation operators of A particles corresponding to the arbitrary but orthogonal single particle wave functions ϕ:

$$|\phi >= \prod_{i=1}^{A} a_i^\dagger|- > \tag{3.12}$$

The expectation value of the energy of the unknown state $|\phi >$ can be expressed as a functional of the single-particle density matrix $\rho_{ij} =< \phi|a_j^\dagger a_i|\phi >$. The minimization of the energy with respect to the Slater determinant is equal to the minimization with respect to ρ when $\rho^2 = \rho$:

$$\frac{\delta}{\delta\phi} < \phi|\hat{H}|\phi >= 0 \tag{3.13}$$

$$\frac{\delta}{\delta\rho}E[\rho] = \sum_{i,j} t_{ij}\rho_{ij} + \frac{1}{2}\sum_{i,j,k,l}\rho_{ki}\overline{\nu}_{ij,kl}\rho_{lj} = 0$$

which leads to the Hartree-Fock equations:

$$\sum_j h_{ij}D_{jk} = \epsilon_k D_{ik} \tag{3.14}$$

$$h_{ij} = t_{ij} + \Gamma_{ij} = t_{ij} + \sum l, k\overline{\nu}_{ik,jl}\rho_{lk}$$
$$b_j^\dagger = \sum_i D_{ij}a_i^\dagger$$

where h_{ij} is a single particle Hamiltonian and D_{ij} is the transformation form for the initial single-particle to the eigenbasis of $\hat{h}$. The single-particle Hamiltonian contains the kinetic energy term and self-consistent field Γ. It is a one-body field and the average over all two-body interaction. By plugging the transformation D to the single-particle density matrix one can get a self-consistent equations for the transformation from the initial to the HF basis:

$$\sum_j (t_{ij} + \sum_{l,k}\sum_{m=1}^{A}\overline{\nu}_{ik,jl}D_{lm}D_{km}^*)D_{jk} = \epsilon_k D_{ik} \tag{3.15}$$

By solving these equations iteratively one can get the resulting Hartree-Fock field Γ which is a one-body approximation of the given two-body interaction ν_{ij}. Usually, parameters of the transformation D_{ij} are found from the fit to the experimental data.

The method can reproduce the ground state properties of spherical nuclei. However, for middle-mass nuclei, the pairing interaction between nucleons plays a significant role. The HF

approach takes into account only the long-range part of the nucleon-nucleon interaction. For the short-range interaction, the Bardeen–Cooper–Schrieffer correction has been applied [BZ13]. Hartree-Fock-Bogoliubov(HFB) method [B$^+$03] also is widely used. However, the detailed description of the HFB approach is outside of the scope of this work.

Skyrme Interaction

The attempts were made to derive ν_{ij} effective interactions directly from the bare nucleon-nucleon interaction. The breakthrough came when the connection to the bare nucleon-nucleon force was abandoned, and effective interactions tailored to mean-field calculations were directly adjusted to the observables of the finite nuclei.

One of such interaction is zero-range Skyrme interaction written for two-body part in the coordinate representation as:

$$\nu_{ij} = t_0(1 + x_0 P^\sigma)\delta(\vec{r}_{ij}) + \tag{3.16}$$
$$+\frac{1}{2}t_1[\delta(\vec{r}_{ij})\vec{k}^2 + \vec{k}^2\delta(\vec{r}_{ij})] + +t_2\vec{k}\delta(\vec{r}_{ij})\vec{k} +$$
$$+iW_0(\vec{\sigma}^1 + \vec{\sigma}^2)\vec{k} \times \delta(\vec{r}_{ij})\vec{k}$$

The first term is a pure zero-range delta force with a spin exchange. The second and third term simulates an effective range and the last term represents the spin-orbit term [Rin00]. The five constant t_0, t_1, t_2, t_3, x_0 and W_0 are adjusted to the experimental binding energies.

Similar to the FRDM2012 model, the HFB method with Skyrme interaction was applied to fit the global nuclear chart and led to the development of HFB-31 model [G$^+$13a]. The total binding energy can be given, as an example, as the sum of the kinetic energy, the Skyrme energy functional (the effective interaction between particles), the Coulomb energy, the pairing energy and the correction for the spurious motion (as in formula 1.4). The HFB31 model has an RMS deviation of 576 keV based on 2353 nuclei of the global nuclear chart. The figure 3.10 shows a comparison between experimental data and the global calculations. First of all the model on average reproduce the experimental trend. However, it is absolutely inconsistent with the observed experimental trends (black dots) representing the N=56 sub-shell closure and the deformation at N=60 in the region. The model instead averages the general trend and is not sensitive to the deviations.

In the frame of this work the considered parametrizations of the Skyrme force is SLy4 [S$^+$03]. This parametrization depends on three parameters, the strength of the pairing interaction and how the pairing strength is distributed as a function of the nuclear density. Consequently, different types of pairing can be obtained depends on the distribution of the pairing

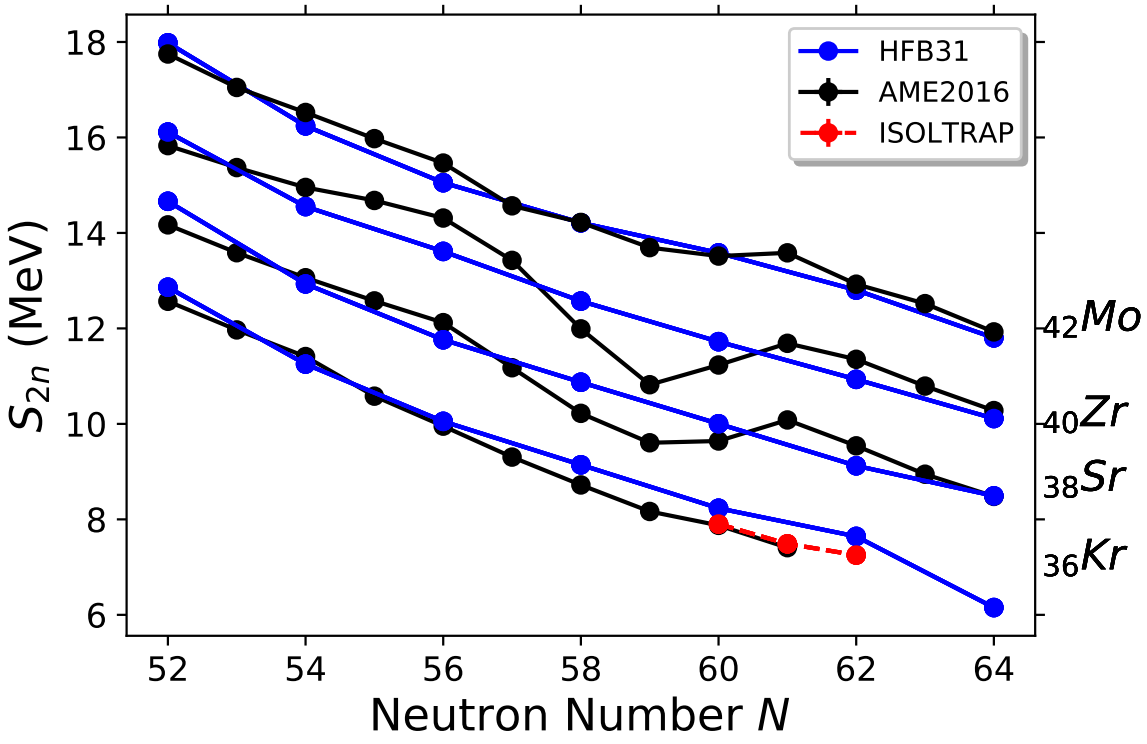

Figure 3.10. The evolution of the two neutron separation energy in neutron-rich krypton, strontium, zirconium and molybdenum isotopic chains. The black-colored two neutron separation energies are taken from AME2016 [H$^+$17]. Red two neutron separation energies calculated from the new $^{96-98}$Kr mass measurements. Blue color corresponds to the HFB31 calculations [G$^+$13a]. For the visibility error bars are omitted.

strength, as an example, two extreme cases are the volume-type pairing and the surface type pairing can be parametrized. The SLy4 model was adjusted only to five doubly magic nuclei.

As we noticed from equation 3.13(2) the binding energy is a function of the nuclear density. This concept can be linked to density functional theory(DFT) [Rin00]. The second parametrization is UNDEF0 which is also an optimization of a nuclear energy density of Skyrme type in the frame of extension of the DFT theory to a nuclear many-body problem. The particle interactions are optimized simultaneously. This model includes a description of both spherical and deformed nuclei and a new model-based, derivative-free optimization algorithm [K$^+$10].

The model which describes the region of interest the best is UNEDF0. One can see in figure 3.11-(b) an excellent agreement between the experimental data and the model in the strontium isotopic chain. First of all, the model predicts the nuclear sub-shell closure at N=56 in the strontium isotopic chain. Second, it also does predict the deformation at N=60 for strontium isotopes. This model predicts a weaker shape transition in the krypton isotopic chain which agrees with observed experimental trends. The SLy4 model does not predict trends of the entire

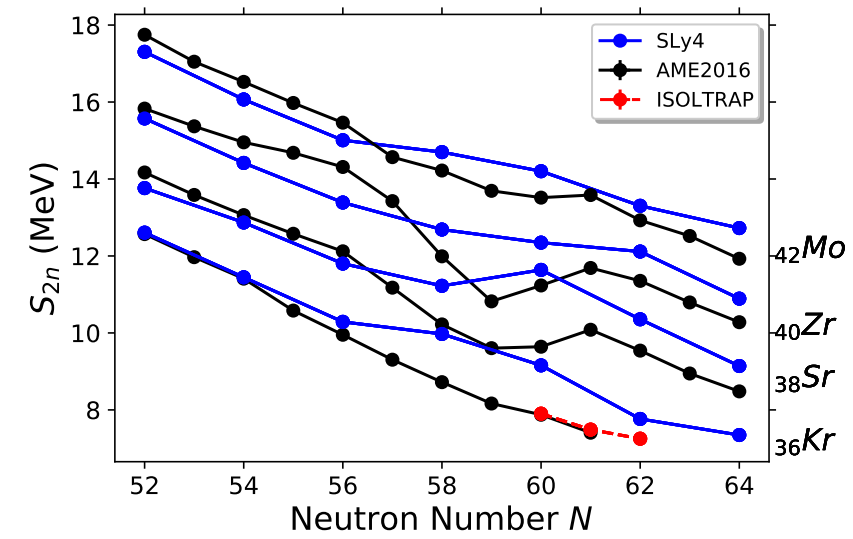

(a)

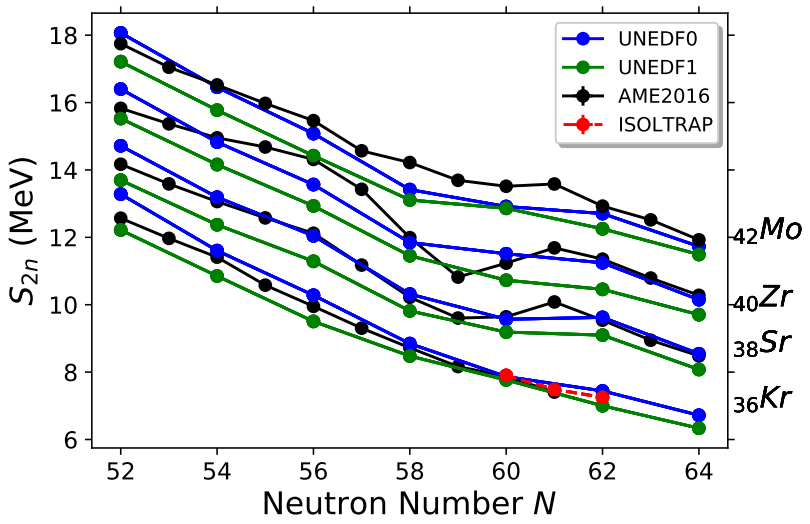

(b)

Figure 3.11. (a)- The evolution of the two neutron separation energy in neutron-rich krypton, strontium, zirconium and molybdenum isotopic chains. The black colored two neutron separation energies are taken from AME2020. Red two neutron separation energies calculated from the new $^{96-98}$Kr mass measurements. Blue color corresponds to the SLy4 calculations [S^{+}03]. (b)- The evolution of the two neutron separation energy in neutron-rich krypton, strontium, zirconium and molybdenum isotopic chains. The black colored two neutron separation energies are taken from AME2016 [H^{+}17]. Red two neutron separation energies calculated from the new $^{96-98}$Kr mass measurements. Blue/green color corresponds to the UNEDF0/1 calculations [K^{+}10]. For the visibility error bars are omitted.

region. For visibility the theoretical calculations have a 1 MeV offset. However, the model seems to globally consider nucleon-nucleon interaction because it indicates nuclear structure but with a shift.

Despite the success of interest of Skyrme interaction the models are not able to adequately describe the interaction in the nuclei. As a result in figures 3.10 and 3.11(a) the HFB31 and SLy4 models do not efficiently separate the sub-shell closure at N=56 and the deformation at N=60. The UNEDF0 model is adjusted to spherical and deformed nuclei and this can be a reason for a good agreement between this model and the experiment.

Gogny Interaction

In 1970 Gogny suggested adding a density-dependent interaction as well as a spin-orbit term. He subsequently proposed a finite-range interaction which is now called the Gogny force.

$$\begin{aligned}\nu_{ij} = \sum_{i=1}^{2} e^{-\vec{r}_{ij}^2/\mu_i^2}(W_i + B_i P^\sigma - H_i P^\tau - M_i P^\sigma P^\tau) + \\ + iW_0(\vec{\sigma}^1 + \vec{\sigma}^2)\vec{k} \times \delta(\vec{r}_{ij})\vec{k} + \\ + t_3(1 + P^\sigma)\delta(\vec{r}_{ij}))\rho^{1/3}(\frac{1}{2}\vec{r}_{ij})\end{aligned} \tag{3.17}$$

The first term represents the central finite range part of the force, the second term is the spin-orbit term having a zero range, the last part represents the density-dependent term [Rin00].

The Gogny D1S model [DG80] [B$^+$91] was adjusted to the entire nuclear chart in order to find constants in equation 3.17. Also, there is a parametrization [B$^+$07] called 5DCH to calculate better correlation energies and shapes [RG14]. Figure 3.12 provides the experimental trends of the two neutron separation energies of both models. On the one hand, the Gogny D1S model(blue) seems to overestimate the N=56 sub-shell closure. On the other hand, it does not reproduce the trend of two neutron separation energies at N=60 for both strontium and krypton isotopes. The 5DCH parametrization treats the overestimation of the sub-shell. Still, it shows only a slight decrease in two neutron separation energy at N>62, which results from the nature of this interaction. This interaction is particularly well suited for representing the pairing correlation which is experimentally visible at shell and sub-shell levels.

Artificial neural network

An artificial neural network(ANN) is a mathematical model built on the principle of the organization and functioning of biological neural networks as in the brain of the biological organism. Nowadays, such models are gaining more popularity and have been applied in nuclear physics.

ANN is a system of simple processors (artificial neurons). Such processors are usually quite simple. Each processor of such a network deals only with signals that it periodically receives

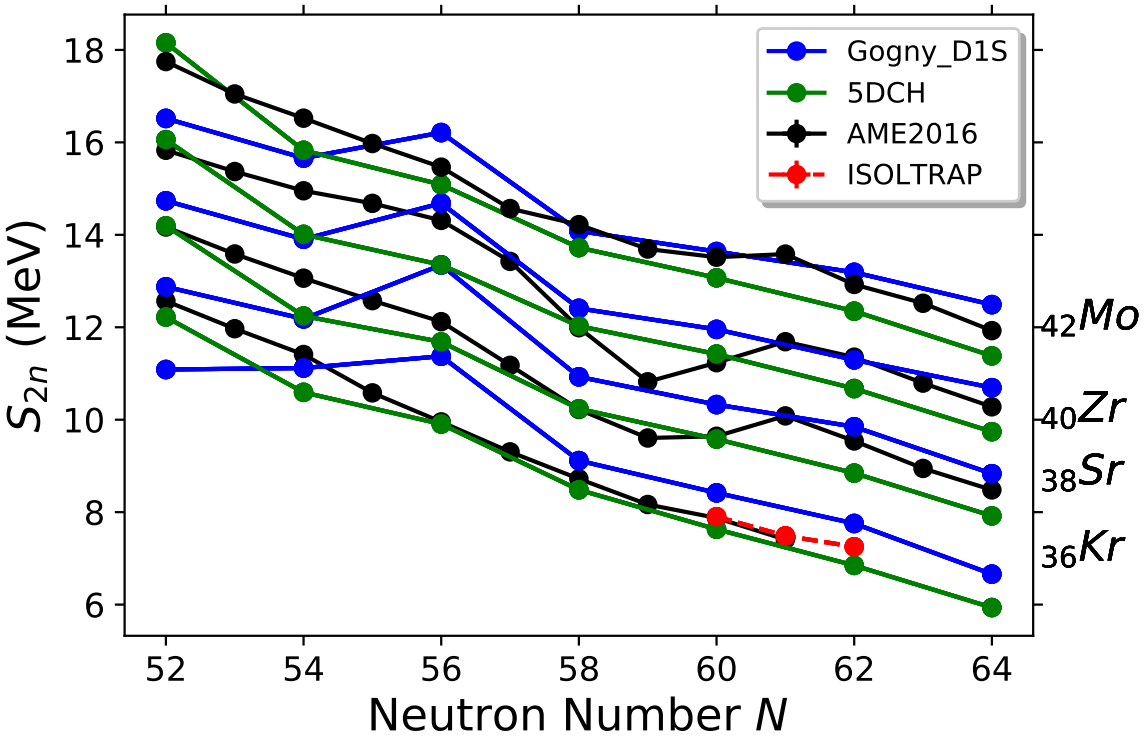

Figure 3.12. The evolution of the two neutron separation energy in neutron-rich krypton, strontium, zirconium and molybdenum isotopic chains. The black-colored two neutron separation energies are taken from AME2016 [H$^+$17]. Red two neutron separation energies calculated from the new $^{96-98}$Kr mass measurements. Blue color corresponds to the Gogny D1S calculations [DG80], green color corresponds to 5DCH parametrization [RG14]. For visibility error bars are omitted.

and sends to other processors. And, nevertheless, when connected in an extensive enough network with controlled interaction, such individually simple processors together are capable of performing rather complex tasks. The processor receives an actual number, and the output of each processor is computed by some non-linear function of the sum of its inputs. Output depends on the weights and the whole network adjusts with learning. The weight decreases or increases the strength of the signal. Technically, training consists of finding the coefficients of connections between neurons.

The ANN approach [L$^+$20a] was used to predict the ground-state properties and exciting energies for only strontium and krypton isotopes with Gogny 5DCH effective interaction to compile the properties. Figure 3.13 provides the results of the calculations. Because of the chosen interaction the new approach does almost the same as the standard Gogny D1S 5DCH approach but in a much shorter time. One of the reasons for this might be that not enough information about deformation is taken into the model. Another model based on similar math-

ematical solutions is Svmin. There is no clear description in the available literature on the underlying interaction used for the model [G+06].

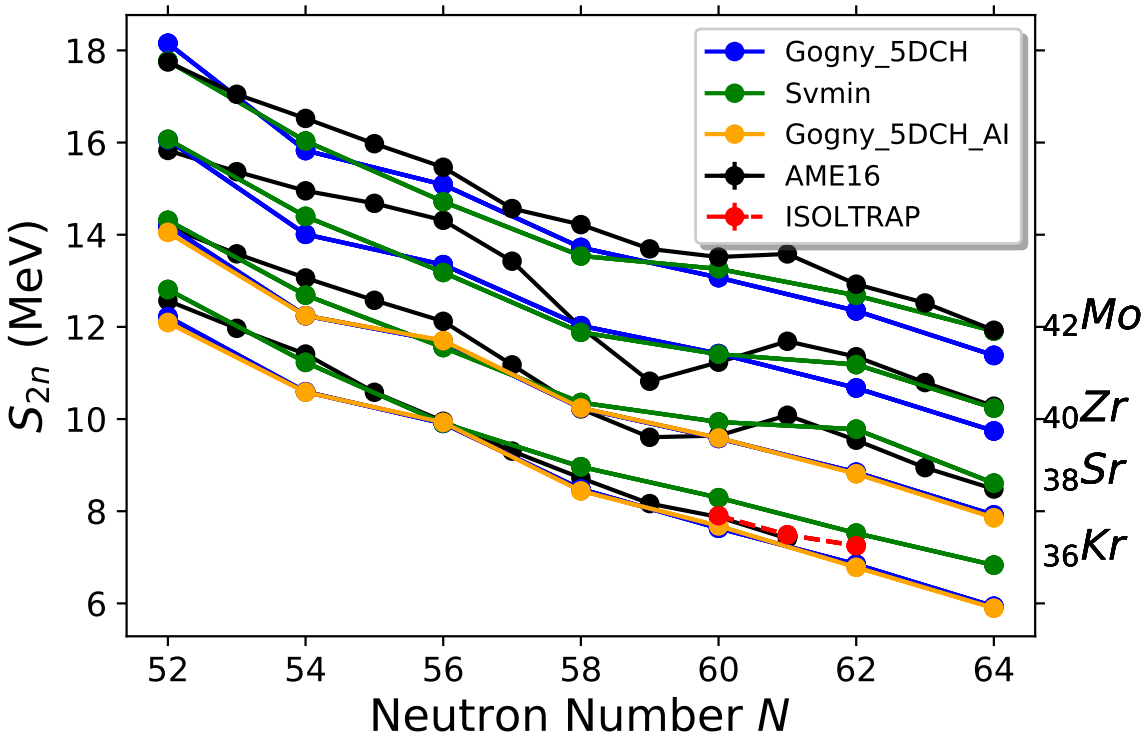

Figure 3.13. The evolution of the two neutron separation energy in neutron-rich krypton, strontium, zirconium and molybdenum isotopic chains. The black-colored two neutron separation energies are taken from AME2020. Red is two neutron separation energies calculated from the new $^{96-98}$Kr mass measurements. Blue color corresponds to the Gogny D1S 5DCH calculations [RG14]. Svmin colored in greed [G+06]. The ANN calculations with Gogny D1S 5DCH parametrization are colored in orange [L+20a]. For visibility error bars are omitted.

The comparison of the first 2^+ excited state predicted by Gogny D1S 5DCH interaction and the new approach is shown in figure 3.14-(a-b). The black dashed line corresponds to the experimental values. The trend of the 2^+ excited states is reproducible by both models. The spotlight of the deformation is a sudden decrease of the excited state energy as shown in figure 3.1-(c) and both models predict this behavior. However, calculations show a more steady decrease of energy compares to the experimental values. The new calculations based on neural networks reproduce the general trends of the energy. However, the major disadvantage is that it does not reproduce the absolute value of the energy as in figure 3.14-(c).

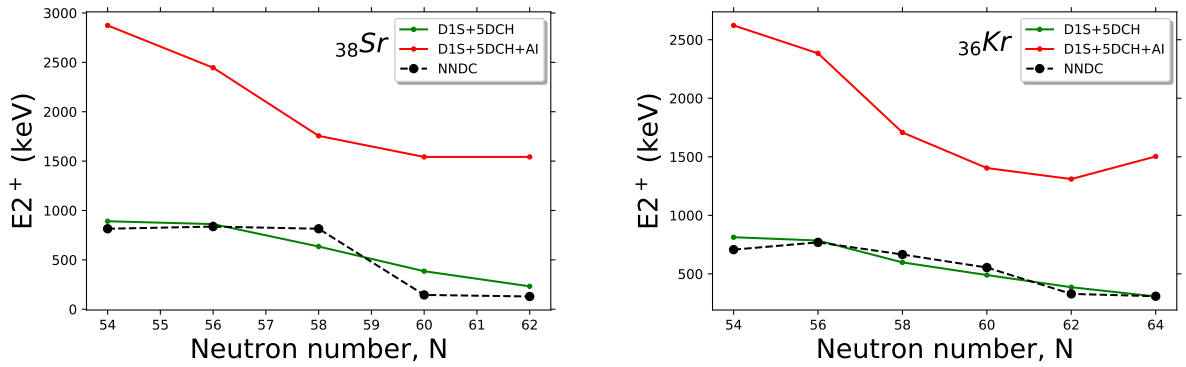

(a) **(b)**

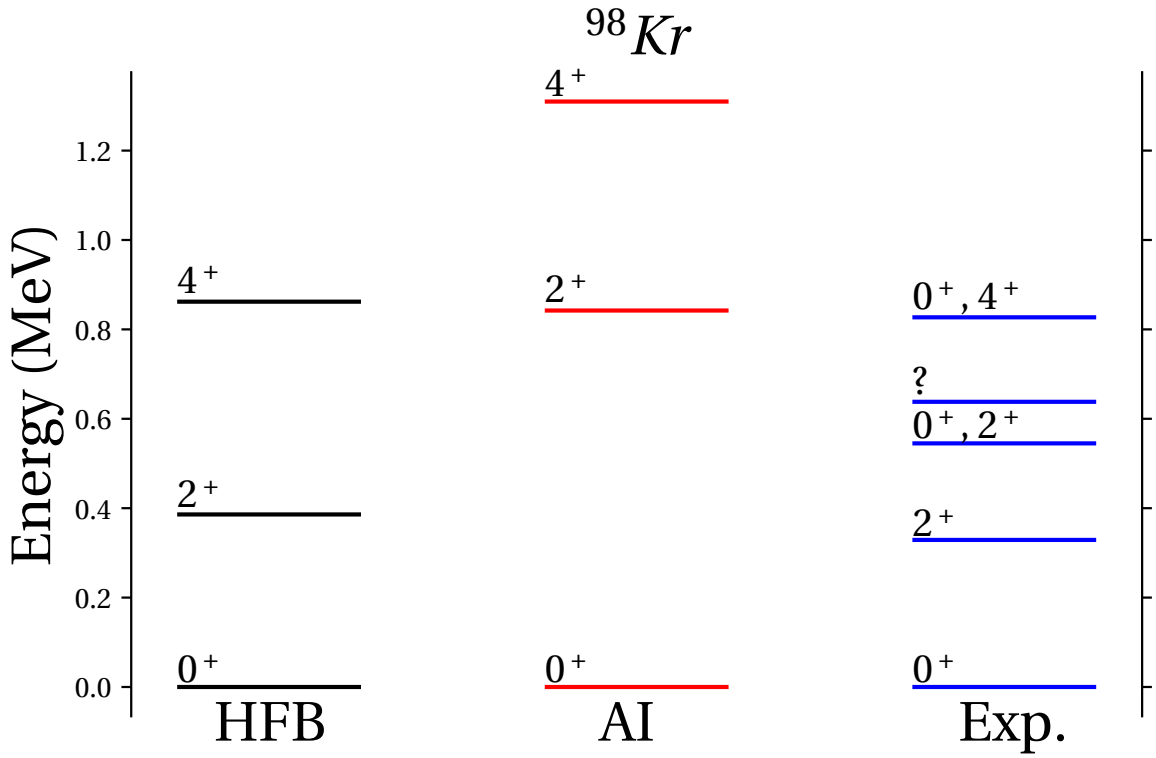

(c)

Figure 3.14. (a)- the first 2^+ excited states in $_{38}$Sr isotopes. (b)- the first 2^+ excited states in $_{36}$Kr isotopes. (c)- the representation of the energy levels for ^{98}Kr isotope. The HFB value is calculated by HFB approach with Gogny interaction, the AI value calculated by the same approach but with artificial neural network, experimental values are taken from [Lab].

3.4 Summary

The new mass measurements of $^{96-98}$Kr isotopes using the versatile ISOLTRAP mass spectrometer have been measured and presented. ^{96}Kr ions were measured by MR-ToF mass measurement technique. The new mass value agrees well with previous experimental values. One measurement was done applying ToF-ICR technique at ISOLTRAP and another applying MR-

ToF mass measurement technique at the TITAN experiment. The mass value does not affect the smooth trend of the two neutron separation energies. ^{97}Kr ions were measured with two different techniques (ToF-ICR and MR-ToF) and in different years (2015 and 2017). Both measurements agree well with the previous mass measurement which was also performed at ISOLTRAP but in the preparation Penning trap. New mass measurement confirms a previously observed trend of the two neutron separation energies but with a much smaller uncertainty. The mass of ^{98}Kr isotope is determined for the first time by applying MR-ToF mass spectrometry. The observed trend of the two neutron separation energies possibly indicates a smooth shape coexistence starting at ^{98}Kr isotope. This result agrees with another experimental property namely the energy of the first 2^+ excited state. A comparison with theoretical calculations available in the literature has been drawn. The macro-micro models FRDM2012 and HFB31 do not predict the region well. The UNEDF0 parametrization shows the best agreement with the experimental values, possibly because of its adjustment of the spherical and deformed nuclei. Gogny D1S and its 5DCH parametrization; Skyrme and its SLy4 parametrization do not predict the region well. The new 5DCH calculations base on the deep neural network methods were made and compared to the well-established methods. The new approach predicts the ground state properties but does not predict the excited state energies.

Table 3.1. Summary of the R_{icr} and C_{ToF} ratios as well as mass excess values of $^{96-98}$Kr ions. Reference masses are taken from AME2016 [H$^+$17] and $T_{1/2}$ values are from NUBASE2016 [WA$^+$17].

				Mass excess (keV)	
Isotope	$T_{1/2}$	References	R_{icr}, C_{ToF}	This work	AME16
^{96}Kr	80 ms	^{48}SO,^{85}Rb	C_{tof}=0.499858112(320)	-53124(13)	-53080(20)
^{97}Kr	62.2 ms	^{39}K	R_{icr}=2.4882083741(720)	-47502(26)	-47420(130)
^{97}Kr	62.2 ms	^{97}Mo,^{85}Rb	C_{tof}=0.503474279(556)	-47442(64)	-47420(130)
^{98}Kr	42.8 ms	^{98}Mo,^{85}Rb	C_{tof}=0.503501959(798)	-44217(100)	-44310(300)

Chapter 4

Conclusion

The work presented in this dissertation can be divided into two sections. The first section describes the measurement steps from the production of radioactive ions at the ISOLDE facility until these ions are detected by ISOLTRAP mass spectrometer. For the mass measurement, different techniques are used, namely Multi-Reflection Time of Flight mass spectrometry and Time of Flight Ion Cyclotron Resonance technique. The techniques, as well as the ISOLTRAP mass spectrometer, have been described. The IS532 [B^+14] and IS642 [A^+17] experimental campaigns were claiming to measure the nuclear sub-shell closure at N=32 in neutron rich $^{50-55}$Sc isotopes and contribute to the determination of Ft-value of ^{70}Br isotope. However, the desired ions were not produced in enough quantity and/or were highly contaminated by stable isotopes. However, the data analysis was performed on ^{49}Sc, ^{50}Sc, ^{70}As, ^{73}Br ions. The idea was to establish a protocol for the MR-ToF mass spectrometry data analysis. For this, the stability of the output fit parameters of Gaussian and EGH fit functions was investigated. The results of the analysis have been published in Nuclear Physics A. These two experimental campaigns and the followed data analysis raised again the question about the transport efficiency of the ISOLTRAP mass spectrometer. It was estimated to be only 0.25 %. The significant losses happen during cooling and bunching in the buncher device. For this, a new set of radio-frequency coils was built. The new device can increase the count rate by remotely tuning the resonance frequency. Also, the effect of the pressure inside the buncher has been studied. The idea was to see how the pressure of the gas inside the buncher affects the peak shape of the beam. Another treatment of the transport efficiency problem was the realignment of the horizontal beamline. Less than 1 mm has been achieved.

The second section of the work is devoted to the deformations at A=100 region. This has been a hot topic for many years. The new mass measurements of the $^{96-98}$Kr isotope demonstrate the evolution of collectively beyond N=60. Masses of ^{96,97}Kr isotopes demonstrate good agreement with previous mass measurements in the region. The mass of ^{98}Kr isotope has been determined for the first time. The uncertainties have been reduced for all cases. A compari-

son with micro-macro and mean-field calculations available in the literature has been drawn. The Skyrme interaction was used in the calculations with the UNEDF0 parametrization. Because this interaction was adjusted on the spherical and deform nuclei the calculations give the best description of the region. It agrees well with experimentally observed trends of the two neutron separation energies. Also, it predicts the smooth shape transition in the krypton isotopic chain. The second nucleon-nucleon interaction which was considered is Gogny with the D1S parametrization. The model does not predict the trends in the region as well as five-dimensional collective Hamiltonian (5DCH) extension. The new 5DCH calculations based on the deep neural network methods were considered. The new calculations require less computational time. However, it predicts the region similar to the previously mentioned theoretical calculations. Moreover, the new approach misses predicting excited state energies. It predicts only the ground state properties. The experimental evidence from both γ-ray spectroscopy and direct mass measurements lead to the same conclusion - the smooth shape transition occurs at N=62 in the krypton isotopic chain.

An outlook of this work is to perform potential energy calculations with HFBTHO and UNEDF0. The evolution of oblate/prolate/global two neutron separation energies would show the energy depth of the two shapes in $^{96-98}$Kr isotopes compared to strontium and zirconium and answer the question of why the kink in two neutron separation energies occurs in strontium isotopic chain but only a flattening in krypton. Also, BMF calculations using the SLy4 Skyrme interaction, within a symmetry-restored generator coordinate method (GCM) are in process. The results are planned to be submitted to the peer-reviewed journal.

Chapter 5

List of published works

- I. Kulikov, A. Algora, D. Atanasov, P. Ascher, K. Blaum, R.B. Cakirli, A. Herlert, W.J. Huang, J. Karthein, Yu.A. Litvinov, D. Lunney, V. Manea, M. Mougeot, L. Schweikhard, A. Welker, F. Wienholtz, Masses of short-lived 49Sc, 50Sc, 70As, 73Br and stable 196Hg nuclides, *Nuclear Physics A, Volume 1002, 2020, 121990*
- M. Mougeot, P. Ascher, D. Atanasov, K. Blaum, K. Chrysalidis, G. Hagen, J.D. Holt, W. Huang, G.R. Jansen, J. Karthein, I. Kulikov, Y. Litvinov, D. Lunney, V. Manea, T. Miyagi, T. Papenbrock, L. Schweikhard, A. Schwenk, T. Steinsberger, Z. H. Sun, A. Welker, F. Wienholtz, S.G. Wilkins, and K. Zuber, Challenging ab-initio nuclear theory near the iconic 100Sn through mass measurements of 99-101In, *Submitted to Nature Physics*
- K. Blaum, J. Karthein, I. Kulikov, Y. Litvinov, D. Lunney, V. Manea, M. Mougeot, L. Nies, W.-J. Ong, H. Schatz, L. Schweikhard, A. Schwenk, F. Wienholtz, K.Zuber, Mass measurement of the self-conjugate 98In for nuclear and astrophysical studies, *Proposal to the ISOLDE and Neutron Time-of-Flight Committee*

Bibliography

[A+03] M. Arnould et al. The p-process of stellar nucleosynthesis: astrophysics and nuclear physics status. *Physics Reports*, 384, 2003.

[A+07] M. Arnould et al. The r-process of stellar nucleosynthesis: Astrophysics and nuclear physics achievements and mysteries. *Physics Reports*, 450(97), 2007.

[A+12] M. Albers et al. Evidence of a Smooth Onset of Deformation in the Neutron-Rich Kr Isotopes. *Physical Review Letters*, 108(062701), 2012.

[A+13] I. Angeli et al. Table of experimental nuclear ground state charge radii: An update. *Atomic Data and Nuclear Data Tables*, 99(1), 2013.

[A+15] D. Atanasov et al. Precision Mass Measurements of $^{129-131}$Cd and Their Impact on Stellar Nucleosynthesis via the Rapid Neutron Capture Process. *Physical Review Letters*, 115(232501), 2015.

[A+16] D. Atanasov et al. Penning-trap mass measurements of Zn and Cu isotopes relevant for the astrophysical rp-process. Technical Report CERN-INTC-2016-040. INTC-P-475, CERN, Geneva, Jun 2016.

[A+17] A. Algora et al. Q_{EC} value determination of the superallowed β-decay of ^{70}Br. Technical Report CERN-INTC-2017-047. INTC-P-514, CERN, Geneva, May 2017.

[A+19] P. Ascher et al. Mass measurements of neutron-rich isotopes near N=20 by in-trap decay with the ISOLTRAP spectrometers. *Physical Review C*, 100(014304), 2019.

[And18] Welker Andree. Implementation and commissioning of the phase-imaging ion-cyclotron-resonance method and mass measurements of exotic copper isotopes with isoltrap, 2018.

[B+57] E. Margaret Burbidge et al. Synthesis of the elements in stars. *Reviews of Modern Physics*, 29, 1957.

[B+63] P. Born et al. On the decay of ^{70}As. *Physica*, 29(4), 1963.

[B+90a] G. Bollen et al. The accuracy of heavy-ion mass measurements using time of flight-ion cyclotron resonance in a Penning trap. *Journal of Applied Physics*, 68, 1990.

[B+90b] F. Buchinger et al. Systematics of nuclear ground state properties in $^{78-100}$Sr by laser spectroscopy. *Physical Review C*, 41(6), 1990.

[B+91] J. Berger et al. Time-dependent quantum collective dynamics applied to nuclear fission. *Computer Physics Communication*, 63(365), 1991.

[B+98] Y. Bai et al. Mass measurement in the fp-shell using the TOFI spectrometer. *AIP conference proceedings*, 455, 1998.

[B+03] M. Bender et al. Self-consistent mean-field models for nuclear structure. *Reviews of Modern Physics*, 75:121–180, 2003.

[B+07] G. F. Bertsch et al. Systematics of the First 2+ Excitation with the Gogny Interaction. *Physical Review Letters*, 99(032502), 2007.

[B+10] K. Blaum et al. Penning traps as a versatile tool for precise experiments in fundamental physics. *Contemporary Physics*, 51:149–175, 2010.

[B+14] D Beck et al. Seeking the purported magic number N=32 with high-precision mass spectrometry. Technical Report CERN-INTC-2014-024. INTC-P-317-ADD-1, CERN, Geneva, Jan 2014.

[B+20] P. A. Butler et al. Evolution of octupole deformation in radium nuclei from coulomb excitation of radioactive ^{222}Ra and ^{228}Ra beams. *Physical Review Letters*, 124(042503), 2020.

[BB18] M. J. G. Borge and K. Blaum. Focus on Exotic Beams at ISOLDE: A Laboratory Portrait. *Journal of Physics G*, 45(1), 2018.

[BG86] L.S. Brown and G. Gabrielse. Geonium theory: Physics of a single electron or ion in a Penning trap. *Review of Modern Physics*, 58, 1986.

[BH08] K. Blaum and F. Herfurth. *Trapped charged particles and fundamental interactions*. Lecture Notes in Physics, 2008.

[BL13] K. Blaum and Y. Litvinov. 100 years of mass spectrometry. *International Journal of Mass Spectrometry*, 349-350, 2013.

[Bla06] K. Blaum. High-accuracy mass spectrometry with stored ions. *Physics Reports*, 425(1), 2006.

[BNVD13] Y. Blumenfeld, T. Nilsson, and P. Van Duppen. Facilities and methods for radioactive ion beam production. *Physica Scripta*, T152(014023), 2013.

[BZ13] R.A. Broglia and V. Zelevinsky. *Fifty Years of Nuclear BCS, Pairing in Finite Systems*. World Scientific, 2013.

[C+63] G. Chilosi et al. Lower excited states of ^{50}Ti. *Nuovo Cimento*, 28, 1963.

[C+74] B. Comisarow et al. Fourier transform ion cyclotron resonance spectroscopy. *Chemistry Physics Letters*, 25, 1974.

[C+87] S. Cwiok et al. Single-particle energies, wave functions, quadrupole moments and g-factors in an axially deformed woods-saxon potential with applications to the two-centre-type nuclear problems. *Computer Physics Communications*, 46:379–399, 1987.

[C+97] P. Campbell et al. The isotope shift of $^{90-91}$Zr by collinear ion-laser beam spectroscopy. *Journal Physics B*, 30:4783, 1997.

[C+02] P. Campbell et al. Laser Spectroscopy of Cooled Zirconium Fission Fragments. *Physical Review Letters*, 89(8), 2002.

[C+07] B. Cheal et al. The shape transition in the neutron-rich yttrium isotopes and isomers. *Physical Letters B*, 645:133–137, 2007.

[C+16] E. Clément et al. Spectroscopic Quadrupole Moments in $^{96-98}$ Sr: Evidence for Shape Coexistence in Neutron-Rich Strontium Isotopes at N=60. 116(022701), 2016.

[C+21] J. J. Cowan et al. Origin of the heaviest elements: The rapid neutron-capture process. *Review of Modern Physics*, 93(015002), 2021.

[Cab63] N. Cabibbo. Unitary symmetry and leptonic decays. *Physical Review Letters*, 10(531), 1963.

[Cha32] J. Chadwick. Possible Existence of a Neutron. *Nature*, 129, 1932.

[D+17] J. Dudouet et al. $^{96}_{36}Kr^{60}$–Low-Z Boundary of the Island of Deformation at N = 60. *Physical Review Letters*, 118(0162501), 2017.

[Daw93] Peter H Dawson. *Quadrupole mass spectrometry and its applications*. American Inst. of Physics, 1993.

[Deh90] H. Dehmelt. Experiments with an isolated subatomic particle at rest. *Review of Modern Physics*, 62, 1990.

[DG80] M. Decharge and D. Gogny. Hartree-Fock-Bogolyubov calculations with the D1 effective interaction on spherical nuclei. *Physical Review C*, 21(1568), 1980.

[DG+16] T. Day Goodacre et al. Blurring the boundaries between ion sources: The application of the RILIS inside a FEBIAD type ion source at ISOLDE. *Nuclear Instruments and Methods in Physics Research B*, 376, 2016.

[Din16] Atanasov Dinko. Precision mass measurements for studies of nucleosynthesis via the rapid neutron-capture process, 2016.

[DR+17] A. De Roubin et al. Nuclear deformation in the A=100 region: Comparison between new masses and mean-field predictions. *Physical Review C*, 96(014310), 2017.

[E+66] J.R. Erskine et al. Energy Levels in ^{49}Sc from ^{48}Ca(He^3,d)^{49}Sc and Other Reactions Proceeding from ^{49}Ca. *Physial Review*, 142(3), 1966.

[E+08] S. Elissev et al. Search for new candidates for the neutrino-oriented mass determination by electron-capture. Technical Report CERN-INTC-2008-012. INTC-P-242, CERN, Geneva, Jan 2008.

[E+14] S. Eliseev et al. A phase-imaging technique for cyclotron-frequency measurements. *Applied Physics B*, 114, 2014.

[F+69] D. Flothmann et al. β spectroscopy of ^{32}P, ^{49}Sc, ^{204}Tl, ^{210}Bi using solid state detectors. *Zeitschrift für Physik*, 225(164), 1969.

[F+03] D H. Forest et al. Related content Laser spectroscopy of neutron deficient zirconium isotopes Collinear laser spectroscopy of radioisotopes of zirconium. Technical report, 2003.

[F+12] D. Fink et al. Q Value and Half-Lives for the Double-β-Decay Nuclide ^{110}Pd. *Physical Review Letters*, 108(062502), 2012.

[F+17a] V. Fedosseev et al. Ion beam production and study of radioactive isotopes with the laser ion source at ISOLDE. *Journal of Physics G*, 44(8), 2017.

[F+17b] F. Flavigny et al. Shape evolution in Neutron-Rich Krypton Isotopes Beyound N=60: First spectroscopy of ^{98,100}kr. *Physical Review Letters*, 118(0242501), 2017.

[FP79] P. Federman and S. Pittel. Unified shell-model description of nuclear deformation. *Physical Review C*, 20, 1979.

[G+68] T.B. Grandy et al. The ^{48}Ca(d,n)^{49}Sc reaction at E_d=5.5 and 6.0 MeV. *Nuclear Physics A*, 113, 1968.

[G+06] Klaus Gernoth et al. Modeling nuclear properties with support vector machines. In *Condensed Matter Theories, Vol. 20*, pages 505–519. Nova Science Publishers, 2006.

[G+13a] S. Goriely et al. Further explorations of Skyrme-Hartree-Fock-Bogoliubov mass formulas. XIII. The 2012 atomic mass evaluation and the symmetry coefficient. *Physical Review C*, 88(024308), 2013.

[G+13b] S. Goriely et al. New fission fragment distributions and r-process origin of the rare-earth elements. *Physical Review Letters*, 111(242502), 2013.

[G+19] J. Glorius et al. Approaching the Gamow Window with Stored Ions: Direct Measurement of ^{124}Xe(p,γ)in the ESR Storage Ring. *Physical Review Letters*, 122(092701), 2019.

[GK78] G. Gartner and E. Klempt. A direct determination of the proton-electron mass ratio. *Zeitschrift für Physik A*, 287, 1978.

[GKT80] G. Graff, H. Kalinowsky, and J. Traut. A direct determination of the proton electron mass ratio. *Zeitschrift für Physik A*, 297, 1980.

[GM64] M. Gell-Mann. A schematic model of baryons and mesons. *Physics Letters*, 8, 1964.

[Gor01] S. Goriely. Nuclear masses and the r- and p-processes of nucleosynthesis. *Hyperfine Interaction*, 132, 2001.

[Got16] A. Gottberg. Target materials for exotic ISOL beams. *Nuclear Instruments and Methods*, 376, 2016.

[GR30] G. Gamow and Ernest Rutherford. Mass defect curve and nuclear constitution. *Proceedings of the Royal Society of London. Series A, Containing Papers of a Mathematical and Physical Character*, 126(803):632–644, 1930.

[H+87] K. Heiguchi et al. The states of ^{73}Se populated by the beta decay of ^{73}Br. *Nuclear Physics A*, 474(2), 1987.

[H+01a] M. Hausmann et al. Isochronous Mass Measurements of Hot Exotic Nuclei. *Hyperfine Interactions*, 132(1-4), 2001.

[H+01b] F. Herfurth et al. A linear radiofrequency ion trap for accumulation, bunching, and emittance improvement of radioactive ion beams. *Nuclear Instruments and Methods in Physics Research Section A*, 469(2), 2001.

[H+06] U. Hager et al. First precision mass measurements of refractory fission fragments. *Physical Review Letters*, 96(042504), 2006.

[H+07] U. Hager et al. Precision mass measurements of neutron-rich yttrium and niobium isotopes. *Nuclear Physics A*, 793(1-4), 2007.

[H+09] J.C. Hardy et al. Superallowed $0^+ \rightarrow 0^+$ nuclear β decays: A new survey with precision tests of the conserved vector current hypothesis and the standard model. *Physical Review C*, 79(055502), 2009.

[H+11] F. Herfurth et al. New mass data for the rp-process above Z = 32. *European Physical Journal A*, 47(6), 2011.

[H+12] S. Hofmann et al. The reaction ^{48}Ca + ^{248}Cm $\rightarrow$ $^{296}116^*$ studied at the GSI-SHIP. *The European Physical Journal A*, 46, 2012.

[H+15] J.C. Hardy et al. Superallowed $0^+ \rightarrow 0^+$ nuclear β decays: 2014 critical survey, with precise results for V_{ud} and CKM unitarity. *Physical Review C*, 91(025501), 2015.

[H+17] W.J. Huang et al. The AME2016 atomic mass evaluation (i). evaluation of input data and adjustment procedures. *Chinese Physics C*, 41(3), 2017.

[Hig64] P. W. Higgs. Broken symmetries and the masses of gauge bosons. *Physical Review Letters*, 13(508), 1964.

[HKE98] H. Horiuchia and Y. Kanada-En'yob. Structure of light exotic nuclei studied with AMD model. *Nuclear Physics A*, 616, 1998.

[Joh65] S.A.E. Johansson. Gamma de-excitation of fission fragments. *Nuclear Physics*, 64, 1965.

[Jon17] Karthein Jonas. Precision mass measurements using the phase-imaging ion-cyclotron-resonance detection technique, 2017.

[K+80] K.S. Kozier et al. Precise atomic masses and mass differences for mercury. *Canadian Journal of Physics*, 58, 1980.

[K+88] T. Kobayashi et al. Projectile Fragmentation of the Extremely Neutron-Rich Nucleus ^{11}Li at 0.79 GeV/nucleon. *Physical Review Letters*, 60(2599), 1988.

[K+95a] M. Keim et al. Laser-spectroscopy measurements of $^{72-96}$Kr spins, moments and charge radii. *Nuclear Physics A*, 586:219–239, 1995.

[K+95b] M. König et al. Quadrupole excitation of stored ion motion at the true cyclotron frequency. *International Journal of Mass Spectrometry and Ion Processes*, 142, 1995.

[K+00] E. Kugler et al. The ISOLDE facility. *Hyperfine Interactions*, 129, 2000.

[K+03] A. Kellerbauer et al. From direct to absolute mass measurements: A study of the accuracy of ISOLTRAP. *The European Physical Journal D*, 22, 2003.

[K+10] M. Kortelainen et al. Nuclear energy density optimization. *Physical Review C*, 82(024313), 2010.

[K+13] S. Kreim et al. Recent exploits of the ISOLTRAP mass spectrometer. *Nuclear Instruments and Methods in Physics Research Section B*, 317:492–500, 2013.

[K+16] R. Klawitter et al. Mass measurements of neutron-rich Rb and Sr isotopes. *Physical Review C*, 93(4), 2016.

[K+19] J. Karthein et al. QEC-value determination for 21Na → 21Ne and 23Mg → 23Na mirror-nuclei decays using high-precision mass spectrometry with ISOLTRAP at the CERN ISOLDE facility. *Physical Review C*, 100(015502), 2019.

[K+20] I. Kulikov et al. Masses of short-lived ^{49}Sc, ^{50}Sc, ^{70}As, ^{73}Br and stable ^{196}Hg nuclides. *Nuclear Physics A*, 1002, 2020.

[Kas13] A. Kasimir. Radioactive transformations and the periodic system of the elements. *Berichte der Deutschen Chemischen Gesellschaft*, 46:153, 1913.

[KE+95] Y. Kanada-En'yo et al. Structure of Li and Be isotopes studied with antisymmetrized molecular dynamics. *Physical Review C*, 52(628), 1995.

[Kow10] M. Kowalska. ISOLTRAP results 2006-2009. *Hyperfine Intecact*, 196, 2010.

[L+75] J.J. LaBrecque et al. The decay and isomerism of ^{70}Se. *Journal of inorganic and nuclear chemistry*, 37(623), 1975.

[L+91] P. Lievens et al. Nuclear ground state properties of ^{99}Sr by collinear laser spectroscopy with non-optical detection. *Physical Letters B*, 256(2), 1991.

[L+98] L.-X. Li et al. Transient events from neutron star mergers. *The Astrophysical Journal Letters*, 507, 1998.

[L+20a] R-D. Lasseri et al. Taming Nuclear Complexity with a Committee of Multilayer Neural Networks. *Physical Review Letters*, 124(0162502), 2020.

[L+20b] Y. Litvinov et al. Nuclear physics research at heavy ion accelerators: Precision studies with stored and cooled exotic nuclei. *Journal of Physics: Conference Series*, 1401(012001), 2020.

[Lab] Brookhaven National Laboratory. NNDC. https://www.nndc.bnl.gov/nudat2/.

[Lan99] K.R. Lang. *Nuclide Abundance Equations*. Springer-Verlag, 1999.

[LJ01] K. Lan and J. W. Jorgenson. A hybrid of exponential and gaussian functions as a simple model of asymmetric chromatographic peaks. *Journal of Chromatography A*, 915(1), 2001.

[Lon16] M. Longair. *Maxwell's Enduring Legacy: A Scientific History of the Cavendish Laboratory*. Cambridge University Press, 2016.

[M+56] D.W. Martin et al. Decay of ^{49}Ca and ^{49}Sc. *Physical Review*, 102(2), 1956.

[M+70] G. Murray et al. The decay of ^{73}Br. *Nuclear Physics A*, 142, 1970.

[M+95] P. Moller et al. Nuclear ground-state masses and deformations. *Atomic Data and Nuclear Data Tables*, 59:185–381, 1995.

[M+02] G. Marshall et al. Fourier transform ion cyclotron resonance detection: principles and experimental configurations. *International Journal of Mass Spectrometry*, 215, 2002.

[M+06] C. A. Meakin et al. Active carbon and oxygen shell burning hydrodynamics. *The Astrophysics Journal Letter*, 637.1, 2006.

[M+08] M. Mukherjee et al. Isoltrap: An on-line penning trap for mass spectrometry on short-lived nuclides. *The European Physical Journal A*, 35(1), 2008.

[M+09] N. Marginean et al. Evolution of deformation in the neutron-rich krypton isotopes: The ^{96}Kr. *Physical Review C*, 80(021301), 2009.

[M+10] G. Munzenberg et al. From j. j. thomson to fair, what do we learn from large-scale mass and half-life measurements of bare and few-electron ions? *AIP Conference Proceedings*, 1224(28), 2010.

[M+13a] V. Manea et al. Collective degrees of freedom of neutron-rich A=100 nuclei and the first mass measurement of the short-lived nuclide ^{100}Rb. *Physical Review C*, 88(054322), 2013.

[M+13b] B.A. Marsh et al. New developments of the in-source spectroscopy method at RILIS/ISOLDE. *Nuclear Instruments and Methods in Physics Research Section B*, 317, 2013.

[M+16a] V. Manea et al. IS490: Seeking the onset of collectivity in neutron-rich krypton isotopes with the mass spectrometer ISOLTRAP. Technical Report CERN-INTC-2016-033. INTC-P-263-ADD-1, CERN, Geneva, Jun 2016.

[M+16b] P. Moller et al. Table of experimental nuclear ground state charge radii: An update. *Nuclear ground-state masses and deformations: FRDM(2012)*, 109-110, 2016.

[M+18] M. Mougeot et al. Precision Mass Measurements of $^{58-63}$Cr: Nuclear Collectivity Towards the N=40 Island of Inversion. *Physical Review Letters*, 120(232501), 2018.

[M+20] B. Smith Matthew et al. High-precision mass measurement of neutron-rich 96kr. *Hyperfine Interactions*, 241:59, 2020.

[M+21] W. Meng et al. The ame2020 atomic mass evaluation (ii). tables, graphs and references. *Chinese Physics C*, 45(030003), 2021.

[May48] M.G. Mayer. On closed shells in nuclei. *Physical Review*, 74, 1948.

[MJ55] M. G. Mayer and J. H. D. Jensen. *Elementary Theory of Nuclear Shell Structure*. Wiley, 1955.

[MP+18] Y. Martinez Palenzuela et al. Enhancing the extraction of laser-ionized beams from an arc discharge ion source volume. *Nuclear Instruments and Methods in Physics Research B*, 431, 2018.

[Myu03] I.J. Myung. Tutorial on maximum likelihood estimation. *Journal of Mathematical Psychology*, 47, 2003.

[N+10] S Naimi et al. Critical-Point Boundary for the Nuclear Quantum Phase Transition Near A=100 from Mass Measurements of ^{96,97} Kr. *Physical Review Letters*, 105(032502), 2010.

[N+20] L Nies et al. Mass measurement of the proton-rich ^{99}In and self-conjugate ^{98}In nuclides for nuclear and astrophysical studies. Technical Report CERN-INTC-2020-025. INTC-P-553, CERN, Geneva, May 2020.

[O+56] G.D. O'Kelley et al. Decay Chain ^{49}Ca-^{49}Sc-^{49}Ti. *Physical Review*, 101(3), 1956.

[O+69] H. Ohnuma et al. Study of the ^{48}Ca(He^3,p)^{50}Sc. *Physical Review*, 177(4), 1969.

[O+92] N.A. Orr et al. Momentum distributions of ^{9}Li fragments following the breakup of ^{11}Li. *Physical Review Letters*, 69(2050), 1992.

[Oga10] Yu. Ts. Oganessian. Synthesis of a New Element with Atomic Number Z=117. *Physical Review Letters*, 104(142502), 2010.

[OK15] Yu. Ts. Oganessian and P. R. Krzysztof. A beachhead on the island of stability. *Physics Today*, 68, 2015.

[P+01] L. Pieper et al. Quantum monte carlo calculations of light nuclei. *Annual Review of Nuclear and Particle Science*, 51:53–90, 2001.

[P+10] L. Penescu et al. Development of high efficiency Versatile Arc Discharge Ion Source at CERN ISOLDE. *Review of Scientific Instruments*, 81, 2010.

[P+13] A. Parikh et al. Nucleosynthesis in type I X-ray bursts. *Progress in Particle and Nuclear Physics*, 69, 2013.

[Pen36] F.M. Penning. Die Glimmentladung bei niedrigem Druck zwischen koaxialen Zylindern in einem axialen Magnetfeld. *Physica*, 3, 1936.

[PS53] W. Paul and H. Steinwedel. Ein neues Massenspektrometer ohne Magnetfeld. *Verlag der Zeitschrift fur Naturforschung 8A*, 448, 1953.

[R+61] I. Rezanka et al. Radioactive decay of ^{49}Sc. *Journal of inorganic and nuclear chemistry*, 18(13), 1961.

[R+74] E. Roeckl et al. Decay properties of neutron deficient Kr isotopes. *Zeitschrift für Physik*, 266(1), 1974.

[R+07] S. Rahaman et al. Precise atomic masses of neutron-rich Br and Rb nuclei close to the r-process path. *European Physics Journal A*, 32(1), 2007.

[R+18] M.P. Reiter et al. Quenching of the N=32 neutron shell closure studied via precision mass measurements of neutron-rich vanadium isotopes. *Physical Review C*, 98:024310, 2018.

[Ram90] N.F. Ramsey. Experiments with separated oscillatory fields and hydrogen masers. *Review of Modern Physics*, 62, 1990.

[RG14] R. Rodríguez-Guzmán. Structure of krypton isotopes calculated with symmetry-conserving configuration-mixing methods. *Physical Review C*, 90(034306), 2014.

[RH+97] H. Raimbault-Hartmann et al. A cylindrical Penning trap for capture, mass selective cooling, and bunching of radioactive ion beams. *Nuclear Instruments and Methods in Physics Research B*, 126(1), 1997.

[Rin00] P. Ring. *The Nuclear Many-body Problem*. Springer, 2000.

[Rut11] E. Rutherford. The scattering of α and β particles by matter and the structure of the atom. *Philosophical Magazine*, 21, 1911.

[Rut20] E. Rutherford. *Nature*, 106, 1920.

[S+89] K.S. Sharma et al. The direct determination of the masses of unstable atoms with the Chalk river on-line isotope separator. *Nuclear instruments and methods in physics research A*, 275(123), 1989.

[S+91a] G. Savard et al. A new cooling technique for heavy ions in a Penning trap. *Physics Letters A*, 158(5), 1991.

[S+91b] K.S. Sharma et al. Masses of $^{103-105}$In and ^{72,73}Br. *Physical Review C*, 44(6), 1991.

[S+01] S. Schwarz et al. Accurate masses of neutron-deficient nuclides close to Z = 82. *Nuclear Physics A*, 693, 2001.

[S+03] M. Stoitsov et al. Systematic study of deformed nuclei at the drip lines and beyond. *Physical Review C*, 68(054312), 2003.

[S+08] M. Smith et al. First penning-trap mass measurement of the exotic halo nucleus ^{11}Li. *Physical Review Letters*, 101(202501), 2008.

[S+09a] J. Savory et al. rp Process and Masses of N=Z=34 Nuclides. *Physical Review Letters*, 102(132501), 2009.

[S+09b] C. Schuler et al. Stelar Nucleosynthesis in the hyades open clusters. *The Astrophysical Journal*, 701, 2009.

[S+09c] L. Stavsetra et al. Independent Verification of Element 114 Production in the ^{48}Ca+^{242}Pu Reaction. *Physical Review Letters*, 103(132502), 2009.

[S+12] V. V. Simon et al. Penning-trap mass spectrometry of highly charged, neutron-rich Rb and Sr isotopes in the vicinity of A≈100. *Physical Review C*, 85(6), 2012.

[S+17] S. Shen et al. The decay and isomerism of ^{70}Se Low-spin States of ^{70}Ge Excited in the ^{70}As(β^++EC) ^{70}Ge Decay. *Nuclear Physics Review*, 34(3), 2017.

[Sal52] E. E. Salpeter. Nuclear reactions in stars without hydrogen. *The Astrophysical Journal*, 115, 1952.

[SC05] Maurizio Salaris and Santi Cassisi. *Evolution of Stars and Stellar Populations*. Wiley, 2005.

[SG89] I. Shim and K.A. Gingerich. The nickel-group molecules NiC, NiSi and NiGe. *Zeitschrift für Physik D*, 12, 1989.

[Sie06] L. Siess. Evolution of massive AGB stars. *Astronomy and Astrophysics*, 448, 2006.

[SR06] H. Schatz and K.E. Rehm. X-ray binaries. *Nuclear Physics A*, 777, 2006.

[T+81] C. Thibault et al. Hyperfine structure and isotope shift of the D_2 line of $^{76-98}$Rb and some of their isomers. *Physical Review C*, 23(6), 1981.

[T+01] B. E. Tomlin et al. Mass measurements of ^{70}Se, ^{71}Se, ^{72}Br, and ^{73}Br. *Physical Review C - Nuclear Physics*, 63(3), 2001.

[T+16] T. Togashi et al. Quantum Phase Transition in the Shape of Zr isotopes. *Physical Review Letters*, 117(172502), 2016.

[Tho97] J.J. Thomson. XXIV. On the structure of the atom: an investigation of the stability and periods of oscillation of a number of corpuscles arranged at equal intervals around the circumference of a circle; with application of the results to the theory of atomic structure. *Philosophical Magazine*, 44(293), 1897.

[Tho04] J.J. Thomson. XXIV. On the structure of the atom: an investigation of the stability and periods of oscillation of a number of corpuscles arranged at equal intervals around the circumference of a circle; with application of the results to the theory of atomic structure. *The London, Edinburgh, and Dublin Philosophical Magazine and Journal of Science*, 7(39), 1904.

[V+68] G.B. Vingiani et al. The ^{49}Ca ground-state analogue. *Physics Letters B*, 26, 1968.

[V+08] S. Verma et al. Projected shell model study of neutron-rich deformed isotopes of Sr and Zr. *Physical Review C*, 77(024308), 2008.

[W+62] A.H. Waptsra et al. The decay of ^{196}Au. *Nuclear Physics*, 31, 1962.

[W+66] D.C. Williams et al. The (t, p) and (t, α) reactions on ^{48}Ca and ^{50}Ti. *Physics Letters*, 22(2), 1966.

[W+69] T.E. Ward et al. Note on the Beta Decay of ^{50g}Sc. *Radiochimica Acta*, 12(4), 1969.

[W+05] C. Weber et al. Weighing excited nuclear states with a Penning trap mass spectrometer. *Physical Letters A*, 347, 2005.

[W+11a] S. Wanajo et al. Electron-Capture Supernovae as the origin of Elements Beyond Iron. *The Astrophysical Journal Letters*, 726, 2011.

[W+11b] R. Wolf et al. A multi-reflection time-of-flight mass separator for isobaric purification of radioactive ion beams. *Hyperfine Interactions*, 199(1-3), 2011.

[W+12] R.N. Wolf et al. On-line separation of short-lived nuclei by a mirror-reflection time-of-flight device. *Nuclear Instruments and Methods A*, 686, 2012.

[W+13a] F. Wienholtz et al. Masses of exotic calcium isotopes pin down nuclear forces. *Nature*, 498, 2013.

[W+13b] R.N. Wolf et al. ISOLTRAP's multi-reflection time-of-flight mass separator/spectrometer. *International Journal of Mass Spectrometry*, 349-350, 2013.

[W+17] F. Wienholtz et al. Mass-selective ion ejection from multi-reflection time-of-flight devices via a pulsed in-trap lift. *International Journal of Mass Spectrometry*, 421, 2017.

[W+20] F. Wienholtz et al. Improved stability of multi-reflection time-of-flight mass spectrometers through passive and active voltage stabilization. *Nuclear Instruments and Methods in Physics Research Section B*, 463, 2020.

[WA+17] M. Wang, G. Audi, et al. The NUBASE2016 evaluation of nuclear properties. *Chinese Physics C*, 41(3), 2017.

[Wei35] C.F.v. Weizsacker. Zur Theorie der Kernmassen. *Zeitschrift fur Physik*, 96, 1935.

[WLM05] D. Walter, David J. Loveland, and Glenn T. Seaborg Morrissey. *Modern Nuclear Chemistry*. Wiley, 2005.

[Wol90] P. Wolfgang. Electromagnetic traps for charged and neutral particles. *Reviews of Modern Physics*, 62, 1990.

[WP90] H. Wollnik and M. Przewloka. Time-of-flight mass spectrometers with multiply reflected ion trajectories. *International Journal of Mass Spectrometry and Ion Processes*, 96, 1990.

[X+19] X. Xu et al. Masses of neutron-rich $^{52-54}$Sc and ^{54,56}Ti nuclides: The N=32 subshell closure in scandium. *Physical Review C*, 99(064303), 2019.

[Z+16] Y.H. Zhang et al. Storage ring mass spectrometry for nuclear structure and astrophysics research. *Physica Scripta*, 91, 2016.